Quantitative Sub Cellular Characterization of Hantavirus Structural Proteins

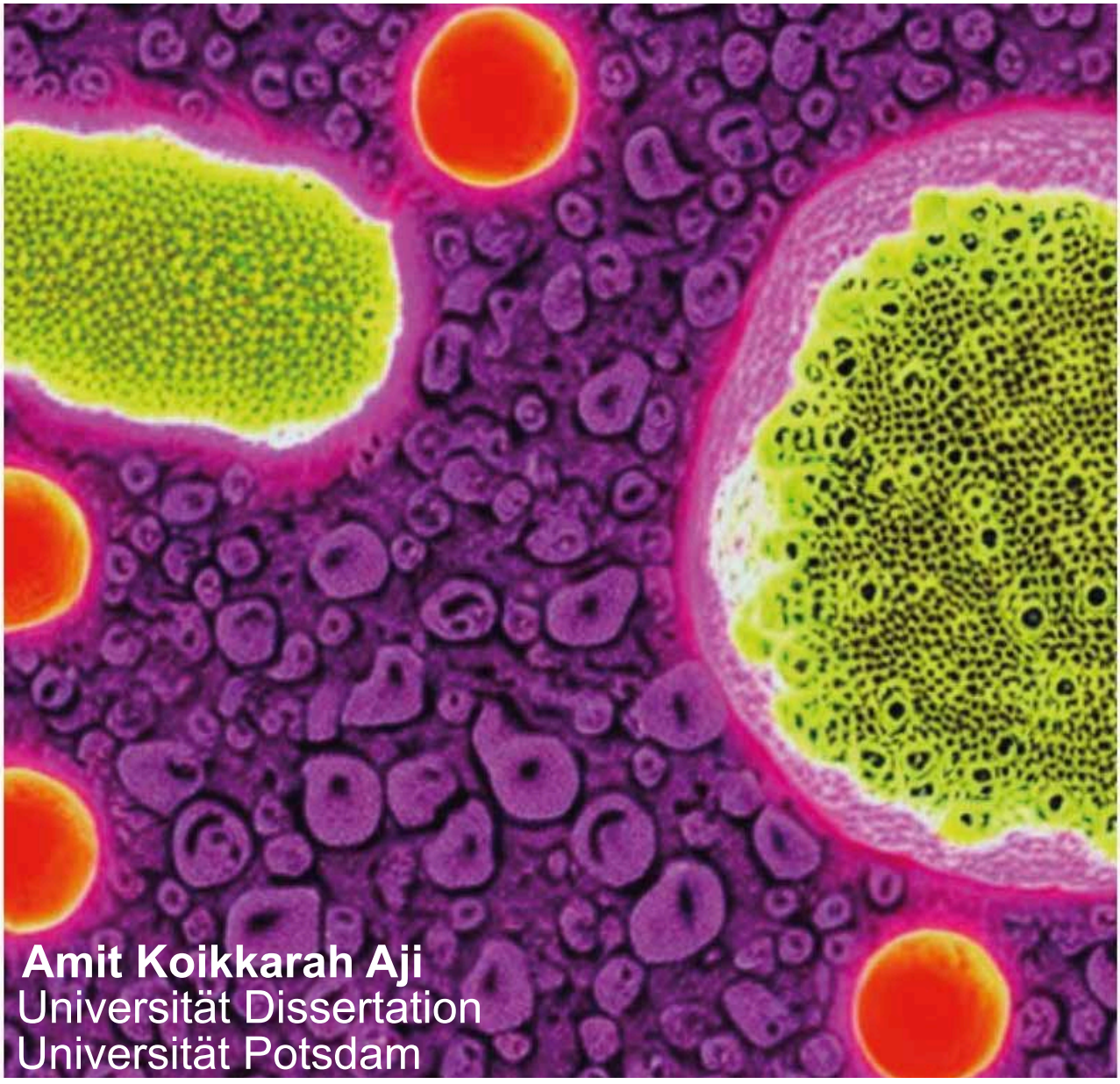

Amit Koikkarah Aji

Universität Dissertation

Universität Potsdam

QUANTITATIVE SUB CELLULAR CHARACTERIZATION OF HANTAVIRUS STRUCTURAL PROTEINS

Universität Dissertation

zur Erlangung des akademischen Grades
"Doctor rerum Naturalium"
(Dr. rer. nat.)
in der Wissenschaftsdisziplin " Zellbiologie "

Eingereicht an der
Mathematisch-Naturwissenschaftlichen Fakultät
Institut für Biochemie und Biologie
der Universität Potsdam

Vorgelegt von

Amit KOIKKARAH AJI

Potsdam, November 2022

Gutachter:

1. Prof.Dr.Salvatore Chiantia, Universität Potsdam
2. Dr.Nicole Tischler, Principial Investigator, Fundación Ciencia & Vida
3. Prof.Dr.Ralph Gräf, Universität Potsdam

Published online on the
Publication Server of the University of Potsdam:
https://doi.org/10.25932/publishup-58661
https://nbn-resolving.org/urn:nbn:de:kobv:517-opus4-586612

Science is a way of life. Science is a perspective. Science is the process that takes us from confusion to understanding in a manner that's precise, predictive and reliable - a transformation, for those lucky enough to experience it, is empowering and emotional.

Brian Greene

CONTENTS

SUMMARY

Hantaviruses (HVs) are a group of zoonotic viruses that infect human beings primarily through aerosol transmission of rodent excreta and urine samplings. HVs are classified geographically into: Old World HVs (OWHVs) that are found in Europe and Asia, and New World HVs (NWHVs) that are observed in the Americas. These different strains can cause severe hantavirus diseases with pronounced renal syndrome or severe cardiopulmonary system distress. HVs can be extremely lethal, with NWHV infections reaching up to 40 % mortality rate. HVs are known to generate epidemic outbreaks in many parts of the world including Germany, which has seen periodic HV infections over the past decade. HV has a trisegmented genome. The small segment (S) encodes the nucleocapsid protein (NP), the middle segment (M) encodes the glycoproteins (GPs) Gn and Gc which forms up to tetramers and primarily monomers & dimers upon independent expression respectively and large segment (L) encodes RNA dependent RNA polymerase (RdRp). Interactions between these viral proteins are crucial in providing mechanistic insights into HV virion development. Despite best efforts, there continues to be lack of quantification of these associations in living cells. This is required in developing the mechanistic models for HV viral assembly. This dissertation focuses on three key questions pertaining to the initial steps of virion formation that primarily involves the GPs and NP.

The research investigations in this work were completed using Fluorescence Correlation Spectroscopy (FCS) approaches. FCS is frequently used in assessing the biophysical features of bio-molecules including protein concentration and diffusion dynamics and circumvents the requirement of protein overexpression. FCS was primarily applied in this thesis to evaluate protein multimerization, at single cell resolution.

The first question addressed which GP spike formation model proposed by Hepojoki et al.(2010) appropriately describes the evidence in living cells. A novel *in cellulo* assay was developed to evaluate the amount of fluorescently labelled and unlabeled GPs upon co-expression. The results clearly showed that Gn and Gc initially formed a heterodimeric Gn:Gc subunit. This subunit then multimerizes with congruent Gn:Gc subunits to generate the final GP spike. Based on these interactions, models describing the formation of GP complex (with multiple GP spike subunits) were additionally developed.

HV GP assembly primarily takes place in the Golgi apparatus (GA) of infected cells. Interestingly, NWHV GPs are hypothesized to assemble at the plasma membrane (PM). This led to the second research question in this thesis, in which a systematic comparison between OWHV and NWHV GPs was conducted to validate this hypothesis. Surprisingly, GP localization at the PM was congruently observed with OWHV and NWHV GPs. Similar results were also discerned with OWHV and NWHV GP localization in the absence of cytoskeletal factors that regulate HV trafficking in cells.

The final question focused on quantifying the NP-GP interactions and understanding their influence of NP and GP multimerization. Gc mutlimers were detected in the presence of NP and complimented by the presence of localized regions of high NP-Gc interactions in the perinuclear region of living cells. Gc-CT domain was shown to influence NP-Gc associations. Gn, on the other hand, formed up to tetrameric complexes, independent from the presence of NP.

The results in this dissertation sheds light on the initial steps of HV virion formation by quantifying homo and heterotypic interactions involving NP and GPs, which otherwise are very difficult to perform. Finally, the *in cellulo* methodologies implemented in this work can be potentially extended to understand other key interactions involved in HV virus assembly.

ZUSAMMENFASSUNG

Hantaviren (HVs) gehören zu einer Gruppe von Zoonosenviren, die den Menschen hauptsächlich über Aerosolübertragung von Nagetierausscheidungen und Urinproben infizieren. HVs werden geografisch unterteilt in: Alte Welt-HVs (OWHVs), die in Europa und Asien vorkommen, und Neue Welt-HVs (NWHVs), die auf dem amerikanischen Kontinent beobachtet werden. Diese verschiedenen Stämme können schwere Krankheiten verursachen, wie hämorrhagisches Fieber mit Nierensyndrom oder schwere Herz-Lungen-Störungen. HVs haben eine hohe Sterblichkeitsrate, wobei NWHV-Infektionen eine Sterblichkeitsrate von bis zu 40 % erreichen. Es ist bekannt, dass HVs in vielen Teilen der Welt epidemische Ausbrüche verursachen können, so auch in Deutschland, wo in den letzten zehn Jahren regelmäßig HV-Infektionen vorkamen. HV besitzt ein trisegmentiertes Genom. Das kleine Segment (S) kodiert das Nukleokapsidprotein (NP), das mittlere Segment (M) kodiert die Glykoproteine (GPs) Gn und Gc, die bei unabhängiger Expression Tetramere und Dimere bilden, und das große Segment (L) kodiert die RNA-abhängige RNA-Polymerase (RdRp).

Die Wechselwirkungen zwischen diesen viralen Proteinen sind von entscheidender Bedeutung für die Aufklärung der Mechanismen der HV-entwicklung. Trotz aller Bemühungen fehlt es nach wie vor an der Quantifizierung dieser Verbindungen in lebenden Zellen. Dies ist für die Entwicklung komplexer Modelle für den Aufbau von HV erforderlich. Diese Arbeit konzentriert sich auf drei Schlüsselfragen im Zusammenhang mit den ersten Phasen der Virionenbildung, an denen hauptsächlich die GPs und NP beteiligt sind. Die Forschungsaufgaben in dieser Arbeit wurden mit Hilfe der Fluoreszenzkorrelationspektroskopie (FCS) untersucht. Die FCS wird häufig zur Bewertung der biophysikalischen Eigenschaften von Biomolekülen, einschließlich der Proteinkonzentration und Diffusionsdynamik, eingesetzt und macht eine Überexpression von Proteinen überflüssig. In dieser Arbeit wurde FFS in erster Linie eingesetzt, um die Multimerisierung von Proteinen bei Einzelzellauflösung zu untersuchen.

Die erste Frage lautete, welches das von Hepojoki et al. (2010) vorgeschlagene Modell der GP-Spike-Bildung den Vorgang in lebenden Zellen adäquat beschreibt. Es wurde ein neuartiger in cellulo-Assay entwickelt, um die Konzentration von fluoreszenzmarkierten und unmarkierten GPs bei der Ko-expression zu bestimmen. Die Ergebnisse zeigten deutlich, dass Gn und Gc zunächst eine heterodimere Gn:Gc-Untereinheit bilden. Diese Untereinheit multimerisiert dann mit kongruenten Gn:Gc-Untereinheiten, um den finalen GP-Spike zu erzeugen. Auf der Grundlage dieser Interaktionen wurden zusätzlich Modelle entwickelt, die die Bildung des GP-Komplexes (mit mehreren GP-Spike-Untereinheiten) beschreiben.

Die HV-GP-Assemblierung findet hauptsächlich im Golgi-Apparat (GA) von infizierten Zellen statt. Interessanterweise wird angenommen, dass NWHV GPs an der Plasmamembran (PM) assembliert werden. Dies führte zur zweiten Frage dieser Arbeit, bei der ein systematischer Vergleich zwischen OWHV- und NWHV-GP durchgeführt wurde, um diese Hypothese zu bestä-

tigen. Überraschenderweise wurde die GP-Lokalisierung an der PM bei OWHV- und NWHV-GPs gleichermaßen beobachtet. Ähnliche Ergebnisse wurden auch bei der Lokalisierung von OWHV- und NWHV-GP in Abwesenheit von zytoskelettalen Faktoren festgestellt, die die HV-Infektion regulieren.

Die letzte Frage dieser Arbeit konzentrierte sich auf die Quantifizierung der NP-GP-Wechselwirkungen und das Verständnis ihres Einflusses auf die Multimerisierung von NP und GPs. Gc-Multimere, die in Gegenwart von NP nachgewiesen wurden, wurden durch das Vorhandensein von perinukleär lokalisierten Regionen mit starken NP-Gc-Wechselwirkungen in lebenden Zellen komplettiert. Es wurde gezeigt, dass die Gc-CT-Domäne die NP-Gc-Assoziationen beeinflusst. Gn hingegen bildete unabhängig von der Anwesenheit von NP tetramerische Komplexe.

Die Ergebnisse dieser Arbeit geben Aufschluss über die ersten Phasen der HV-Assemblierung, indem sie die Homo- und Hetero-Interaktionen zwischen NP und GPs quantifizieren, was sonst nur sehr schwer möglich ist. Schließlich können die in dieser Arbeit implementierten in cellulo-Methoden potenziell erweitert werden, um andere Schlüsselinteraktionen zu verstehen, die an der HV-Assemblierung beteiligt sind.

GLOSSARY

NOMENCLATURE

Ab	Antibody
ANDV	Andes Orthohantavirus
BCCV	Black Creek Canal Orthohantaviruses
BD	Bidirectional
CT	cytoplasmic tail
dpi	Days post infection (dpi)
ER	Endoplasmic Reticulum
ERGIC	ER–Golgi intermediate compartment
GA	Golgi Apparatus
GP	Glycoprotein
GPC	Glycoprotein Precursor
GPMV	Giant Plasma Membrane Vesicle
HCPS	Hantavirus cardiopulmonary syndrome
HFRS	Hemorrhagic Fever with Renal Syndrome
HPS	Hantavirus Pulmonary Syndrome
hpt	Hours post transfection
HTNV	Hantaan Orthohantavirus
HV	Orthohantaviruses
MBS	Mean Beam Spiltter
NP	Nucleocapsid Protein
NSs	Non Structural S segment
NWHV	New World Orthohantaviruses
OWHV	Old World Orthohantaviruses

PM Plasma Membrane

PML Plasma Membrane Localization

PUUV Puumala Orthohantavirus

RdRP RNA-dependent RNA polymerase

RNP Ribonucleoprotein

ROI Region of Interest

RVFV Rift Valley Fever Virus

SNV Sin Nombre Orthohantavirus

SP Signal Peptide

TGN Trans Golgi Network

TM Transmembrane

TSWV Tomato spotted wilt virus

VSV Vesicular Stomatitis Virus

Construct Terminology

AF Alexa Fluor

GP BD mCh2 Same as SP-GP BD mCh2

mEGFP-GP Same as SP-mEGFP-GP

mEGFP-GP* No SP of respective Gn at N terminus

Chemicals

NEM N-ethylmaleimide

PBS Phosphate buffered saline

Physical Parameters

ϵ Molecular Brightness

σ Variance

σ^2_{cc} Cross Variance

σ^2_d Detector Noise

σ^2_n Occupation number

τ_{Diff} Diffusion time

B_{cc} Cross Brightness

N_{cc} Cross Number

ζ Number of GPs localized in Golgi Apparatus

n Average number of molecules encountered in the illumination volume (for N&B)

B Apparent Brightness

N Apparent Number

N_{eff} Average particle number in the detection volume

Relative CC Relative Cross Correlation

Techniques

ccN&B Cross Correlation Number and Brightness

cryo-EM Cryo-electron microscopy

FCCS Fluorescence Cross-Correlation Spectroscopy

FCS Fluorescence Correlation Spectroscopy

FRET-FLIM Förster resonance energy transfer by Fluorescence lifetime Imaging

N&B Number and Brightness

sFCS Line scan FCS

1

INTRODUCTION

1.1. HANTAVIRUSES

1.1.1. HISTORICAL TIMELINE OF HANTAVIRUS OUTBREAKS

Orthohantaviruses (HVs) were first described in Chinese medical accounts around AD 960 where a similar pathogen was reported [1]. The English sweating sickness that resulted in five epidemics between 1485 and 1551 is proposed to be a medieval HV strain. Further, occurrences of nephritis epidemic during the American Civil War and World War I have been ascribed to HVs [2]. HV infections came to the limelight during the Korean conflict (1950-1953) where over 3000 United Nations troops fell casualty to the Korean hemorrhagic fever, commonly called as hemorrhagic fever with renal syndrome (HFRS). The etymology of HV is credited to this event since the conflict took place primarily around the shores of the Hantaan river.

In Finland, Puumala HV (PUUV) was isolared initially in the 1980s in bank voles (*Myodes glareolus*) [3]. In 1993, the HV outbreak at the Four Corners Region of Southwestern USA resulted in the identification of the Hantavirus Pulmonary Syndrome (HPS) [4]. This outbreak killed 13 people and had a mortality rate close to 50 % [5]. Andes HV (ANDV) outbreak in southern Argentina in 1995 presented the first epidemiological evidence of person to person transmission for HPS infections [6]. Similar conclusions were obtained for the outbreak that occurred in the Chubut province, Argentina between November 2018 and February 2019 [7].

1.1.2. CLASSIFICATION OF HANTAVIRUSES

HVs are classified geographically into Old World Hantaviruses (OWHVs), that are detected primarily in Asia and Europe, and New World Hantaviruses (NWHVs), that are observed in North and South America [8]. At present, over 28 HV strains cause pathogenic infections in humans, ranging from acute renal failure to pulmonary oedema and severe hemorrhagic illness, around the world (Figure 1.1) [9]. While around 1000 HPS cases have been reported, more than 100,000 HFRS cases are known to occur worldwide each year. In several countries, HV infections remain undetected leading to under-reporting [3]. HV infections have been steadily reported in Germany since early 2000s, with significantly increased numbers in the "outbreak"

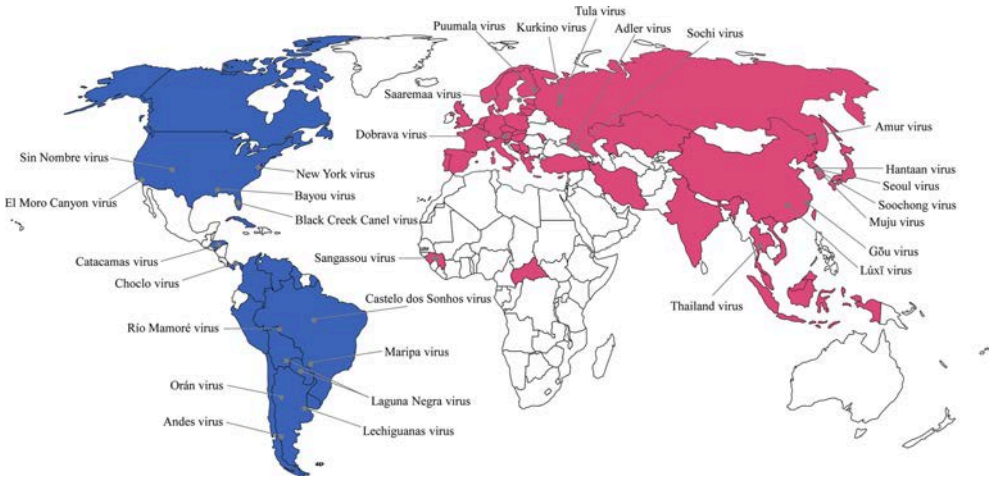

Figure 1.1: **Geographical Distribution of Hantavirus Strains**: HV strains and the geographical locations of their prevalence is shown here. HV strains causing HFRS infection (red) and HV strains causing Hantavirus Cardiopulmonary Syndrome (HCPS) (blue). Image adapted with permission from Kim et al. [9]

years of 2007, 2010, 2012 and 2017. PUUV is the prevalent strain detected in Germany, particularly in the western and southern parts of the country [10] [11].

1.1.3. OVERVIEW OF HANTAVIRUS PATHOGENESIS

HV replication begins in the vascular endothelium [12]. Viraemia (entry of viruses in the bloodstream) is detected five to ten days post infection indicating stronger viral persistence compared to acute lytic progression seen with other hemorrhagic fevers (viral genome introduced into the host cell during lytic cycle) [13]. A probable explanation for this viral persistence includes lack of a competent T cell response [12]. Several host cell surface proteins have been credited to mediate HV entry into cells. Protocadherin-1 is an important host receptor that regulates the entry of NWHV infections in endothelial cells while appropriate host factors that are necessary for entry and infection by OWHV strains in endothelial cells remain undiscovered [14].

HVs utilize multiple entry pathways including clathrin dependent endocyotsis, macropinocytosis [15] [16], clathrin independent receptor-mediated endocytosis and so on. Post internalization, the virions are transported to the endosomes. Here, they detach from the cellular receptors due to low pH. Finally, the viral genetic material is released into the cytoplasm and then trafficked to the site of viral replication. Depending on the HV strain, the viral replication is executed at the Golgi apparatus (GA) or at the plasma membrane (PM) (Figure 1.2) [12].

OWHV strains cause HFRS, while NWHV strains results in HPS and Hantavirus Cardiopulmonary Syndrome (HCPS). Disease severity depends on the HV genotype since HFRS caused by Hantaan HV (HTNV) is more lethal than the mild clinical discourse with the PUUV infection. HFRS occurs in five distinct phases: febrile, hypotensive, oliguric, polyuric and convalescent. HCPS is often associated with a rapid onset of respiratory failure owing to pulmonary oedema

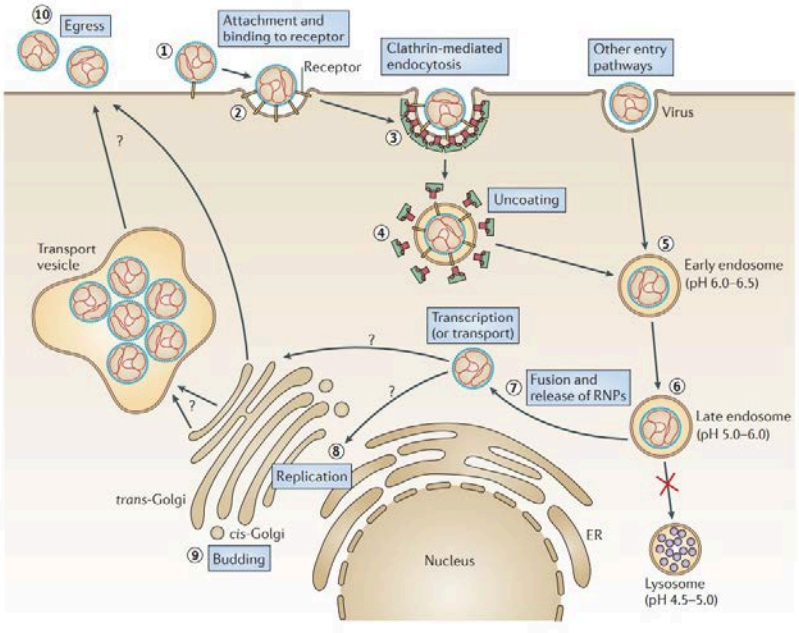

Figure 1.2: **Hantavirus viral replication cycle**: HV virion initially attaches to the cell surface receptor (Step 1). Following endocytosis (Step 2), the virion enters the cell (Step 3). Multiple entry pathways have been attributed to HVs. In this figure, clathrin-mediated endocytosis is shown. The clathrin coat of the vesicle is disassembled (Step 4), and the virion-harbouring vesicle enters the early endosome (Step 5). The virion then matures into a late endosome (Step 7). Fusion between the viral and endosomal membranes is modulated by acid-induced conformation changes in the viral fusion protein in the late endosome. This results in release of the ribonucleoproteins (RNPs) (Step 7). Initial transcription occurs and followed by the transport of RNPs to the ER–Golgi intermediate compartment (ERGIC) for transcription. Viral replication occurs in viral factories that are located at the ERGIC or the cis-Golgi (step 8). The nascent viruses are proposed to bud into the cis-Golgi (step 9), from where they are trafficked to the plasma membrane for release. Progeny virions egresses out of the PM (step 10). Image reprinted from Vaheri et al.[12] with re-print permission (License Number:5419390409918)

.

and cardiogenic shock. Increased capillary permeability is considered as a characteristic of HV infection and could explain multiple HV infection symptoms like hypotension and abdominal pain, extravasation of fluid to alveolar spaces and pulmonary oedema that takes place in HFRS and HCPS [12]. Thrombocytopenia, leucocyte activation and release of proinflammatory cytokines and chemokines are other infection observations [17].

The case fatality rate between HV strains ranges from 0.08–0.4% for HFRS disease caused by PUUV and ≈5%, for HTNV infections. On the other hand, for the NWHVs causing HCPS infections, up to 40% fatality rate has been reported [12]. Broader understanding on HV infection pathogenesis is addressed in excellent reviews by Vaheri et al. [12], Vapalahti et al. [18], Bi et al. [19], Krueger et al. [20] and Muranyi et al. [21].

1

1.1.4. GENERAL STRUCTURAL FEATURES OF THE HANTAVIRUS GLYCOPROTEIN AND NUCLEOCAPSID PROTEIN

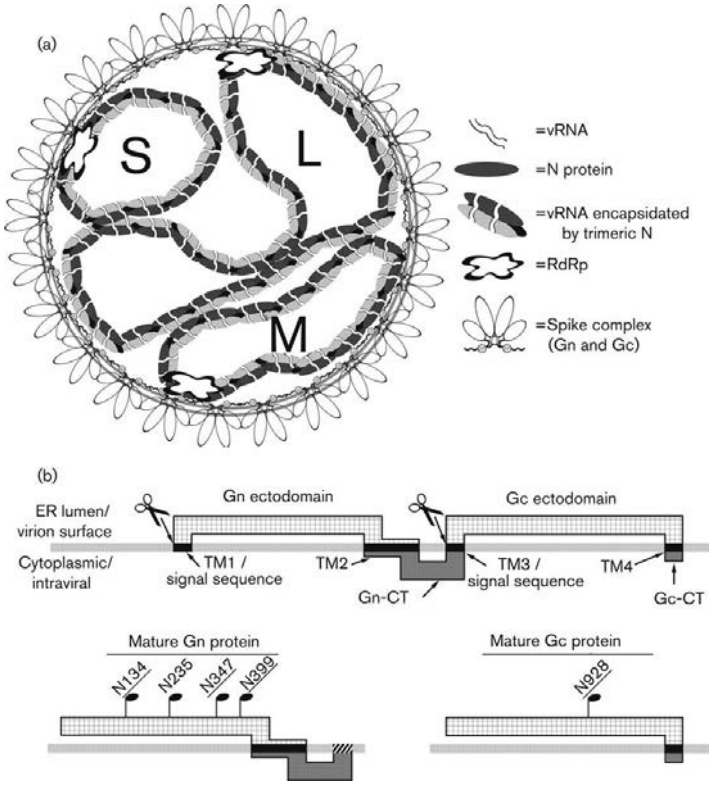

Figure 1.3: **Structure of Hantavirus Particle**: (a) Schematic picture of the trisegmented HV virion is shown. The S segment constitutes of Nucleocapsid Protein (NP), M Segment constitutes of the Glycoproteins Gn and Gc and L segment constitutes of RNA dependent RNA Polymerase (RdRP). (b) Representation of the major domains of the GP including transmembrane (TM), ectodomain and cytoplasmic tail (CT) regions. The peptide sequence marked by the scissors symbol (close to TM3 domain) cleaves the M segment into the Gn and Gc. At the bottom major the conserved glycosylation sites on Gn and Gc are shown. The glycans are N-glycosylated with high mannose content and have important functions in proper protein folding and golgi transport. Image reprinted from Hepojoki et al.[23] with re-print permission (Permission License ID: 1285152-1).

HVs (family:*Hantaviridae*) belong to the order of *Bunyavirales*, a family of negative sense RNA viruses with a trisegmented genome [22]. HV virions are either round, pleiomorphic or tubular with a broad diameter variation between 70 to 350 nm [23]. HVs are composed of three negative sense polarity single stranded RNA segments: small (S), medium (M) and large (L) (Figure 1.3). The 3.7 kb M segment encodes a glycoprotein precursor (GPC) that initially matures in ER and subsequently cleaves into two envelope glycoproteins (GPs) Gn and Gc [24]. The 2.1 kb S segment encodes the nucleocapsid protein (NP) and the 6.6 kb L segment encodes the RNA-dependent RNA polymerase (RdRP) [23]. This dissertation focuses on the characterization of the GPs and NP and their interactions responsible for the virion development in living cells.

The GPs constitutes of transmembrane (TM) and cytoplasmic tail (CT) regions (Figure 1.3). Four glycosylation sites on Gn and one glycosylation site on Gc are conserved across all HV strains. The conserved glycans are N-linked oligosaccharide with high mannose content [25]. There is an additional O-linked glycosylation site on PUUV Gc [26]. The glycans on Gn play an important role in protein folding and intracellular trafficking [27], while the N-glycan on Gc influences cell-cell fusion [28]. Signal peptide (SP) at the N-terminus of GPC directs it to the endoplasmic reticulum (ER). GPC is co-translationally cleaved by the peptidase sequence WAASA to yield the GPs, Gn and Gc [29]. Gn further interacts with Gc to form the tetrameric spikes $(Gn/Gc)_4$. These spikes are then transported to the site of the assembly, GA or PM, depending on the HV strain [30].

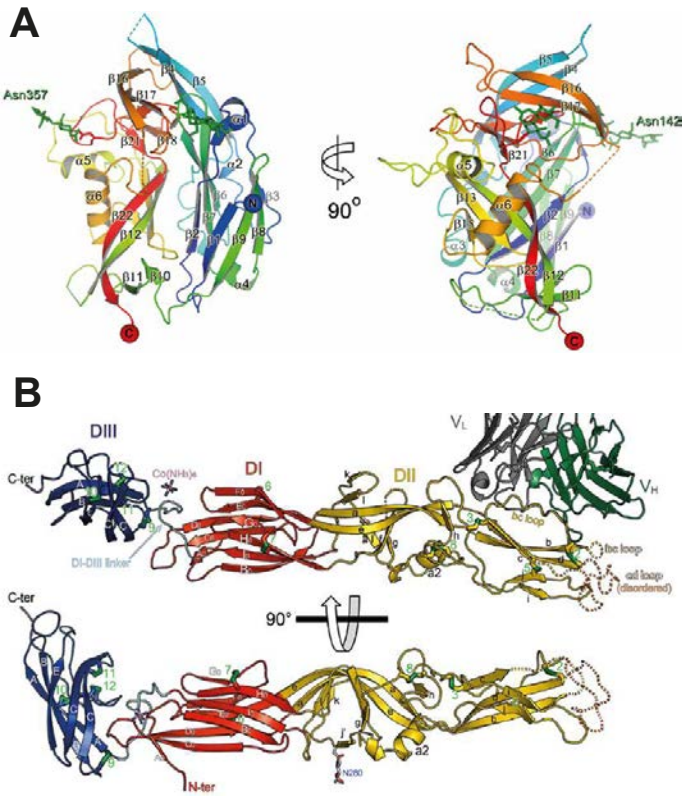

Figure 1.4: **Crystal Structures of Gn and Gc Ectodomain**: (A) Schematic picture of the crystal structure of PUUV Gn ectodomain. Ribbon representation of Gn with N-terminus (in blue) and C-terminus (in red). Glycans are shown as green sticks. Image adapted with permission from Li et al. [31] (B) Schematic picture of the representative structures of HV Gc ectodomain. Domain I, II and III are shown in red, blue and yellow respectively. The linker between domains I and III is denoted in cyan and the C-terminal end is in magenta. The disulfide bonds are displayed as sticks with sulfur atoms in green. The lower panel shows an orthogonal view of Gc. Dotted lines describe the disordered region, corresponding to the cd loop (orange) and the distant end of the bc loop (yellow). Image adapted with permission from Guardado-Calvo et al. [32].

Gn has an α/β fold consisting of five α-helices, a 3_{10}-helix and twenty-two β-strands. The β strands assemble to form five β sheets. The Gn fold is stabilized by seven intra-domain disulfide bonds (Figure 1.4 A) [31]. Fitting of HTNV Gn ectodomain using high resolution cryo-electron microscopy (cryo-EM) reconstruction revealed that HTNV Gn localizes to membrane-distal tetrameric spikes of the mature envelope surface and shields the Gc fusion protein on the mature virion. The mixed α/β fold of Gn ectodomain resembles the alphavirus GP E2 [33].

Gc has a class II membrane fusion protein fold, that primarily consists of β domains [34]. Gc ectodomain consists of three domains. Domain I, an eight stranded β sandwich arranges domain II and III around it. Two insertions in domain I between the strands D_o-E_o and strands H_o-I_o forms the elongated β stranded domain II. Domain III has six β strands and is followed by the stem region (Figure 1.4 B) [35] [36]. Gc:Gc contacts dictate the lateral interactions between GP spikes. Gc is primarily monomeric when solubilized from viral particles [37].

The NP is the most abundant viral protein in HV infected cells [38]. Stable NP trimers serve as intermediates for NP multimerization and in the formation of RNP complexes [39]. NP trimers binds specifically to a panhandle structure of the RNPs formed by the base-paired 3 $'$- and 5 $'$ end of the genome [40]. During viral encapsidation, NP interacts with itself and other viral and host cellular proteins. Regions on both the N and C termini are involved in NP multimerization. Recently, Arragain et al. [41], using high resolution cryo-EM, showed that NP residues 1 to 79 do not follow helical symmetry and corresponds to flexibly linked coiled-coil structure. These residues influences the interaction of NP with RdRP. NP-RdRP association is essential for cap snatching, the first step of transcription, that allows the RdRp to replicate the viral genome [42]. The subsequent RNP complex which consists of NP, viral RNA and RdRP, then interacts with the first GP spike complex, initiating the formation of virions [43]. For further reading on NP multimerization, the reader is directed to the review by Reuter & Krueger [39].

1.2. FLUORESCENCE CORRELATION SPECTROSCOPY (FCS)

FCS is an experimental technique that evaluates kinetic processes through statistical analysis of equilibrium fluctuations [44]. It was invented in 1972 to initially monitor the fluctuations in the chemical equilibrium of the binding reactions [45]. Technical innovations with confocal laser microscopy and high quantum-efficiency solid-state light detectors, have permitted in carrying out FCS experiments with single molecule resolution [43]. Theoretical and experimental advances also allowed FCS implementation to determine important physical parameters as diffusion coefficient, chemical rate constant, concentration and so on [46].

FCS is frequently used for the detection and temporal evaluation of bio-molecules at extremely low concentrations ($\approx \mu$M range) [47]. Improvements during the past decades have expanded its capabilities using new modalities. This includes dual color Fluorescence Cross-Correlation Spectroscopy that can measure interaction between molecules, pair correlation function that provides information about directionality of molecules and line scanning FCS which overcomes the resultant photobleaching due to slow diffusion of molecules on the membranes. FCS can be combined with super-resolution STED (Stimulated Emission Depletion) microscopy to detect diffusion in nanoscale region. Innovations with data analysis such as photon counting histogram and fluorescence intensity distribution analysis further allowed the determination of the molecu-

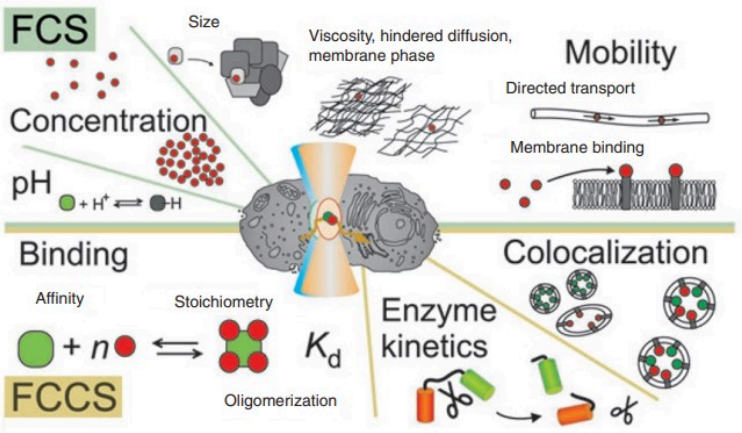

Figure 1.5: **Applications of fluorescence correlation spectroscopy based techniques**: Overview of the biophysical features that can be derived using FCS and Fluorescence Cross-Correlation Spectroscopy (FCCS). Details, regarding the implementation of FCS and FCCS in deriving the physical parameters presented in this figure is elaborated in Bacia, Kim & Schwille [49]. Image reproduced from Bacia, Kim & Schwille [49] with re-print permission (License Number:5419400012952).

lar brightness of fluorophore molecules [48].

1.2.1. THEORETICAL FOUNDATIONS OF FCS

This section provides a brief overview on the implementation of FCS theory for the analysis of different molecular processes. FCS experiments are performed by placing fluorescently-labeled molecules in the focal plane of an illumination volume [48]. Fluorescence fluctuations are generated while the system under observation is in thermal equilibrium. These fluctuations provide an insight into the macroscopic and microscopic characteristics of the the system [51]. Constitutive equations for FCS presented in this section are referenced from Muetze, Ohrt & Schwille [51] and the main aspects are described briefly here.

Fluorescence fluctuations are defined as the deviation of δF(t) from the temporal average of the signal, $\langle F(t)\rangle$

$$\delta F(t) = F(t) - \langle F(t)\rangle \tag{1.1}$$

Temporal average of the fluorescence signal $\langle F(t)\rangle$ over the acquisition time period T is calculated as follows:

$$\langle F(t)\rangle = \frac{1}{\mathrm{T}}\int_0^T F(t)\,dt \tag{1.2}$$

These fluctuations around an equilibrium state are mathematically analyzed using an auto correlation function (ACF). It compares the fluctuating signal at time t with itself at a time point t $+\tau$, where τ is the lag time. The ACF is defined by the following equation:

$$G(\tau) = \frac{\langle \delta\mathrm{F(t)}\ \delta\mathrm{F(t)(t}+\tau)\rangle}{\langle \mathrm{F(t)}\rangle^2} \tag{1.3}$$

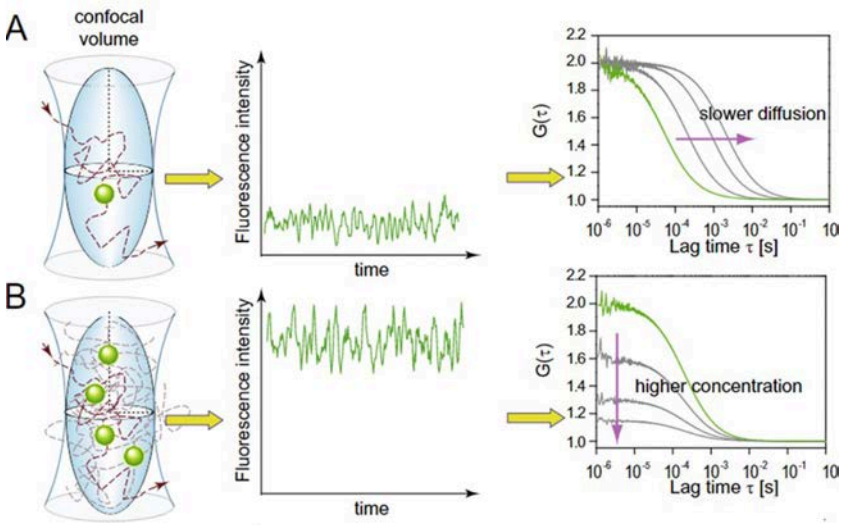

Figure 1.6: **Demonstration of FCS principle**: This image shows in brief the implementation of FCS. Fluorescent molecules diffusing in and out of the confocal volume, results in temporal intensities, which are later transformed into autocorrelation function (ACF) for further analysis. Two key features of the ACF curves are highlighted in this figure. The ACF trend (denoted by the arrow) in [A] highlights that diffusion coefficient is inversely proportional to the width of the ACF curve. The ACF trend (denoted by the arrow) in [B] shows concentration in the confocal volume is inversely proportional to the amplitude of the ACF curve (y-intercept magnitude). Image adapted from Macháň & Wohland (2014) with permission (License ID :5424300507048)

Equation 1.3 can be fitted to an appropriate model function to obtain the characteristic time scales and concentration of the system. On approximating the confocal volume to a 3D ellipsoidal Gaussian detection volume, the 3D ACF can be converted into the following analytical expression for freely diffusing species:

$$G(\tau) = \frac{1}{N_{eff}}\left(\frac{1}{1+(\tau/\tau_{Diff})}\right)\left(\frac{1}{1+(\omega_o/z_o)^2\ (\tau/\tau_{Diff})}\right)^{1/2} \tag{1.4}$$

Equation 1.4 is used in obtaining physical parameters of the 3D volume. $G(0) \approx \frac{1}{N_{eff}}$, where N_{eff} is the average particle number in the detection volume (V_{eff}) (see Figure 1.6), where $V_{eff} = \pi^{3/2}\omega_o^2 z_o$ (z_o: axial beam waist of the ellipsoidal and ω_o: radial beam waist of the ellipsoidal). Thus, magnitude of the y-intercept of the ACF function is inversely proportional to the number of particles (N) encountered in V_{eff}. The characteristic diffusion time $\tau_{Diff} = \omega_o^2/4D$, where D is the diffusion co-efficient. τ_{Diff} for a single component system. τ_{Diff} is defined as the time the ACF amplitude has decayed to half its value ($G(\tau_{Diff}) \approx \frac{1}{2}\ G(0)$).

The parameters N_{eff} and τ_{Diff} are used to calculate relevant biophysical parameters such as protein concentration, dissociation constant and so on. In this work, protein multimerization is evaluated using FCS based techniques.

Exhaustive mathematical analysis on FCS is further presented in Krichevsky & Bonnet [44],

Ries & Schwille [52], Elson [53] and the textbook by Wohland, Maiti & Macháň [54].

1.2.2. NUMBER AND BRIGHTNESS (N&B)

N&B, initially described by Digman et al. [55], derives its implementation from FCS principles. Data set required for N&B is a stack of images of the same illumination view acquired over a defined acquisition time. Moment analysis developed by Qian and Elson [56] is then applied on every pixel of the image stack to determine the multimerization state of the proteins and protein concentration. Unlike other FCS techniques, N&B cannot calculate the diffusion properties of the system.

N&B theory presented in this work is adapted from Digman et al. [55] and from Dunsing [57]. In brief, the average ($\langle \mathrm{k} \rangle$) and variance (σ^2) of the intensity values obtained over a prescribed acquisition time over several frames K is initially calculated:

$$\langle \mathrm{k} \rangle = \frac{\sum_i \mathrm{k}_i}{\mathrm{K}} \tag{1.5}$$

$$\sigma^2 = \frac{\sum_i (\mathrm{k}_i - \langle \mathrm{k} \rangle)^2}{\mathrm{K}} \tag{1.6}$$

While acquiring fluorescence intensities during N&B ,it is crucial to set an optimal pixel dwell time. This is to ensure that temporally averaged intensity fluctuations are not cancelled out, yet they persist long enough for efficient sampling. In N&B, the variance σ^2 of the intensity is contributed by the occupation number (σ_n^2) and the noise of the detector (σ_d^2). ϵ, the molecular brightness is the number of photons emitted per second per molecule. In biological applications, ϵ is associated with clustering or aggregation of the fluorophore. n denotes the average number of molecules encountered in the illumination volume. In this work, the detector noise is approximated to follow Poisson statistics, which implies that the mean and the variance of the values pertaining to the distribution of the detector noise are equal. This background information helps us in the development of the constitutive equations:

$$\sigma_n^2 = \epsilon^2 n \tag{1.7}$$

$$\sigma_d^2 = \epsilon n \tag{1.8}$$

$$\langle \mathrm{k} \rangle = \epsilon n \tag{1.9}$$

Equation 1.7 is based on the concept in FCS where each species contributes to the fluctuations according to the square of the particle brightness. Equation 1.9 highlights that the average intensity is the conserved product of molecular brightness multiplied by the average number of particles.

Since constitutive equations for variance also involves noise, additional terms apparent brightness B and apparent number N are defined as follows:

$$\mathrm{B} = \frac{\sigma^2}{\langle \mathrm{k} \rangle} = \frac{\sigma_n^2}{\langle \mathrm{k} \rangle} + \frac{\sigma_d^2}{\langle \mathrm{k} \rangle} = \frac{\epsilon^2 n}{\epsilon n} + \frac{\epsilon n}{\epsilon n} = \epsilon + 1 \tag{1.10}$$

$$N = \frac{\langle k \rangle^2}{\sigma^2} = \frac{\epsilon n}{\epsilon + 1} \tag{1.11}$$

Inputting B=1 in Equation 1.10 we get ϵ=0, which indicates an immobile fraction. When B is greater than 1, it indicates the presence of mobile particles in pixels that can be used for analyzing protein clustering or aggregation. The final molecular brightness ϵ does not depend on the number of particles, allowing us to report precise multimerization values of protein clusters (since the parameter reported is invariant). Thus, using simple statistical measures on intensity, ϵ and n can be derived for calculating protein multimerization and concentration respectively.

1.2.3. CROSS CORRELATION NUMBER AND BRIGHTNESS (ccN&B)

The concept of correlation stems from the discipline of digital signal processing. Correlation evaluates the coherence between two different signals or waveforms. The coherence is denoted as the similarity between a signal and the time delayed version of another signal. Cross correlation was extended to N&B applications by Digman et al. [58]. This was achieved by correlating the fluorescence amplitude fluctuations for two colors to detect the presence of molecular complexes and their stoichiometry. ccN&B additionally generates pixel resolution maps of protein complexes. Equations for ccN&B in this work have been inferred from the work of Digman et al. [58] and Petrich et al. [59]. and the general overview for a two channel system is presented:

For a two channel system, the cross variance parameter is initially defined in terms of the intensity in channel 1 (G) and intensity in channel 2 (R) over K frames as:

$$\sigma^2_{cc} = \frac{\sum(G_i - \langle G \rangle)(R_i - \langle R \rangle)}{K} \tag{1.12}$$

Using σ^2_{cc}, the cross brightness value and the cross number values can be defined as follows:

$$B_{cc} = \frac{\sigma^2_{cc}}{\sqrt{\langle k_G \rangle \langle k_R \rangle}} \tag{1.13}$$

$$N_{cc} = \frac{\langle G \rangle \langle R \rangle}{\sigma^2_{cc}} \tag{1.14}$$

Cross variance value of zero implies the fluctuations in the two channels are independent of each other. A positive value implies that signals are correlated and a negative value indicates that they are anti-correlated. And finally, relative cross correlation value (Relative CC) in the following manner:

$$\text{Relative CC} = \text{maximum}\left(\frac{N_{cc}}{N_G}, \frac{N_{cc}}{N_R}\right) \tag{1.15}$$

where N_G and N_R is obtained from the amplitudes of the ACF from channel 1 and channel 2 respectively.

1.2.4. LINE SCAN FCS (SFCS)

sFCS was utilized for the analysis of GP oligomerization in Giant Plasma Membrane Vesicles (GPMVs) (otherwise known as cellular blebs) in chapter 4. In sFCS, the detection volume is primarily scanned along the major axis of the membrane. This results in a detection time in the membrane region, which is lower than the τ_{Diff} of the fluorophore. During data analysis, the emission from the membrane bound flurophores is integrated for every scan. These intensity values form the discrete time trace which can then be used to calculating the correlation curve. [52]. Constitutive equations of FCS are then applied (refer Equations 1.1 to 1.4). The key advantages of sFCS in studying membrane dynamics includes robustness to instabilities, excellent signal to noise ratio and minimal photobleaching for longer acquisition times [60] [61].

sFCS is utilized in multiple biological applications. It is particularly useful for determining the diffusion co-efficient in living cells. sFCS allows the complete representation of diffusion dynamics including total number of diffusion processes, fraction of molecules contributing to each diffusion mode and the respective diffusion time scales [62]. The practical implementation of sFCS is discussed in detail by Hermann, Ries & García-Sáez [63] and in chapter 2. For more detailed review on the different modalities of sFCS, which is beyond the scope of this work, the reader is directed to the excellent review by Ries & Schwille [64].

1.3. OBJECTIVES OF THE THESIS

This dissertation focuses on the quantitative characterization of GP and NP dynamics that regulate the formation of the HV virion at single cell resolution. Three key questions on the consequences of NP and GP interactions as a function of protein multimerization were formulated to understand the steps of mechanistic development of HV particle. They are as follows:

1. **Which model proposed by Hepojoki et al. [43] describes the formation of the GP spike in cells ? (Presented in chapter 3)**
2. **Is GP localization and its possible assembly at the PM, an exclusive feature for NWHV strains ? If yes, what are the characteristics of the GPs partitioned at the PM ? (Presented in chapter 4)**
3. **What is the magnitude of interaction between NP and GPs ? How does NP-GP interactions influence GP multimerization during the virion development ? (Presented in chapter 5)**

These questions were assessed by primarily performing FCS based methods (described in the previous sections) in living cells expressing fluorescently labelled HV GP constructs. Relevant biophysical parameters were then derived to investigate these crucial steps of HV virion assembly in a quantitative manner. The implementation of these FCS techniques have been detailed in chapter 2.

The details regarding these investigations are handled as a separate chapter. Each chapter commences with the motivation for addressing the research question. This will be followed by presenting the results, discussing the key implications of the findings and the overall conclusions pertaining to the particular question.

The quantitative outcomes of these research questions would provide the precise understanding of the HV GP spike formation, the dynamics of cellular localization of GPs and the implications on GP multimerization in the presence of NP. These findings will permit the exploration of other key HV interactions in the future, utilizing the methodologies outlined in this dissertation.

2

Materials and Methods

2.1. Materials

2.1.1. Cloning and Generation of Chimeric Proteins

The PUUV GP sequence is from the PUUV Sotkamo/V-2969/81 strain, the HTNV GP sequence is from the HTNV (76-118) strain and the ANDV GP gene sequence used in this work is from the ANDV isolate CHI-7913. Plasmids encoding PUUV Gn and Gc were a gift from A.Herrmann (Humboldt Universität, Berlin), HTNV GPC was a gift from S.Weiss (Charité, Berlin) and ANDV GPC was a gift from Dr.Nicole Tischler (Fundación Ciencia & Vida, Chile). Plasmids encoding PUUV SP-mEGFP-Gn and PUUV SP-mEGFP-Gc used the pEGFP-C1 vector. Plasmids encoding HTNV SP-mEGFP-Gn and HTNV SP-mEGFP-Gc used the pcDNA vector. N-terminus of HV mEGFP-GP and the N terminus of untagged HV GP, was fused with the GnSP (signal peptide sequence present at the N terminus of Gn) of the respective HV strain. This was introduced to ensure a physiological membrane incorporation and localization of the fusion protein constructs [65]. Commercial vector produced by Twist Bioscience (San Francisco, CA, USA) was used to encode ANDV SP-mEGFP-Gc and ANDV SP-mEGFP-GPC. ANDV SP-mEGFP-Gn and ANDV StrepII-Gn was encoded in the pcDNA vector system. ANDV Strep-II GPC and ANDV GPC-mEGFP was a kind gift of Dr. Nicole Tischler (Fundación Ciencia & Vida, Chile). Plasmid encoding a fluorescent trans-Golgi resident protein (Golgi-mTurquoise) was a gift from Dorus Gadella (Addgene plasmid number # 36205). The constructs mp-YFP, mp-EGFP and mp-Ch2, which has a myristoylation and palmitoylation (mp) motif at the N terminus, were a kind gift of Dr.Roland Schwarzer (University Hospital Essen). Their design has been described earlier in [59] and [65].

The bidirectional (BD) expression vector was a kind gift from Dr.Katja Arndt (Universität Potsdam). One promoter of the BD expression system expresses the cytosolic mCherry2 and the other promoter expresses the unlabelled HV GP (containing the GnSP at the N terminus, as stated in the previous paragraph). The unlabeled GP sequence was PCR-amplified and separately inserted into the BamHI/EcoRI cassette to produce GP BD mCh2 plasmid. PUUV YFP-NP and PUUV GnSP-YFP-Gn were a kind gift of Dr.Roland Schwarzer (University Hospital, Essen).

Name	Backbone	Insert	Resistance
PUUV SP-mEGFP-Gn	pEGFP-C1 (Clonetech)	PUUV SP,PUUV Gn	Kanamycin
PUUV SP-mEGFP-Gc	pEGFP-C1 (Clonetech)	PUUV SP,PUUV Gc	Kanamycin
PUUV SP-mEYFP-Gn	mEYFP-C1	PUUV SP,PUUV Gn	Kanamycin
PUUV SP-mCh2-Gn	mCh2-C1	PUUV SP,PUUV Gn	Kanamycin
PUUV SP-mCh2-Gc	mCh2-C1	PUUV SP,PUUV Gc	Kanamycin
PUUV Gn BD mCh2	p210 2D vector	PUUV SP-Gn, mCherry2*	Ampicillin
PUUV Gc BD mCh2	p210 2D vector	PUUV SP-Gc, mCherry2*	Ampicillin
PUUV YFP-NP	pmYFP-C1	PUUV NP	Kanamycin
PUUV NP-YFP	pmYFP-N1	PUUV NP	Kanamycin
PUUV mEGFP-NP	pEGFP-C1 (Clonetech)	PUUV NP	Kanamycin
PUUV mTurq2-NP	PUUV mEYFP-NP	mTurq2	Kanamycin
ANDV Strep-II GPC	pI.18	ANDV Strep-II GPC	Ampicillin
ANDV SP-mEGFP-Gn	pCDNA3.1+	ANDV SP, ANDV Gn	Ampicillin
ANDV SP-mEGFP-Gc	Commerical Vector (Twist)	ANDV SP-mEGFP-Gc	Ampicillin
ANDV Gn BD mCh2	p210 2D vector	ANDV SP-Gn, mCherry2*	Ampicillin
ANDV Gc BD mCh2	p210 2D vector	ANDV SP-Gc, mCherry2*	Ampicillin
ANDV SP-mEGFP-GPC	Commerical Vector (Twist)	ANDV SP-mEGFP-GPC	Ampicillin
ANDV GPC-mEGFP	pI.18	ANDV GPC-mEGFP	Ampicillin
HTNV SP-mEGFP-Gn	pCDNA3.1+	HTNV SP,HTNV Gn	Ampicillin
HTNV SP-mEGFP-Gc	pCDNA3.1+	HTNV SP,HTNV Gc	Kanamycin
HTNV Gn BD mCh2	p210 2D vector	HTNV SP-Gn, mCherry2*	Ampicillin
HTNV Gc BD mCh2	p210 2D vector	HTNV SP-Gc, mCherry2*	Ampicillin
mp-mEGFP	pEGFP-C1 (Clonetech)	mp-mEGFP	Kanamycin
mp-YFP	pmYFP-C1	mp-YFP	Kanamycin
mp-mCh2	pmCherry-C1	mp-Ch2	Kanamycin
Golgi-Turq	pmTurquoise-C1	Golgi Retention Signal	Kanamycin
ER-EGFP	pEGFP-C1 (Clonetech)	ER-EGFP	Kanamycin
ER-mCh2	pmCherry-C1	ER-mCh2	Kanamycin

Table 2.1: **Overview of all plasmids described in this work**. mCherry2* is the cytosolic variant and in the p210 2D vector, its expression is regulated by the higher expressing promotor (since in the p210 2D vector the two promoters do not have a 1:1 ratio for cytoplasmic expression). SP refers to the signal peptide present at the N-terminus of the respective HV GPC.

PUUV YFP-NP construct design is elaborated in [66]. Briefly, Vero E6 cells infected with the PUUV Sotkamo/V-2969/81 strain were subjected to mRNA extraction and subsequently by reverse transcription and PCR amplification to obtain the PCR product with NP. This was later subcloned into pmYFP-C1 using the NotI and BsrgI restriction sites. mTurq2-NP was generated by excising YFP using AgeI and NotI restriction sites and substituting it with the mTurq2 PCR product. PUUV NP-YFP and PUUV mEGFP-NP used the pmYFP-N1 (multiple restriction site region at the N terminus of YFP) and pEGFP vectors respectively. All cloning plasmids were verified via Sanger sequencing (performed externally by LGC sequencing).

In this dissertation, the GP constructs have the respective SP (from the N-terminus of Gn) fused to the N terminus of the non-fluorescent GP and mEGFP-GP constructs. The fluorescent constructs will be referred in this work as mEGFP-GP and the non-fluorescent constructs as GP. If SP is not present in the mEGFP-GP construct, then it will be explicitly mentioned as mEGFP-GP* and stated that it is devoid of the SP domain. Similarly, the bidirectional plasmid will be referred to as GP BD mCh2 in this work (implying one promoter expresses SP-GP and the other promoter expresses cystolic mCherry2 in a defined ratio; here the mCherry2 is regulated by the higher expressing promotor, since the two inserts are not produced in a 1:1 ratio (details see [90])).

2.1.2. CELL LINES

Cell Line	Origin	Morphology	Order no.
A549	Human alveolar lung cells	epithelial	CCL™ - 185
HEK 293T	Human embryonic kidney cells	epithelial	CCL™ - 11268
CHO	Chinese hamster ovary cells	epithelial	CCL™ - 61
Vero E6	African green monkey kidney cells	epithelial	CRL™ - 1586
BHK-21	Baby syrian golden hamster kidney fibroblast cells	epithelial	CCL™ - 10

Table 2.2: **Overview of cell lines used in this study**: All cell lines were purchased from ATCC, Manassas, Virginia, USA.

The experiments in this work were completed in multiple cell lines including Chinese Hamster Ovary Cells (CHO), Baby Hamster Kidney cells (BHK)-21, Human Embryonic Kidney (HEK)293T, adenocarcinomic human alveolar basal epithelial (A549)) and African green monkey kidney epithelial cells (VeroE6) cells. HV infections are known to have variations in its pathogenesis according to the strain and cell model used [67]. Thus, most of the experiments presented in this work were conducted in multiple cell models.

CHO cell models were chosen since they were previously utilized for HTNV VLP formation [68] and for studying the influence of receptors on HV infection [69]. BHK-21 cells were selected since they were previously used for identifying the role of integrins in ANDV infection [70], assessing NP oligomerization [71], understanding the influence of host cytosketelal factors on HV

infections [72] and for generating pseudotyped VSV systems to elucidate the role of neutralizing antibodies against NWHV infection [73]. HEK 293T cell models were chosen due to its utilization in understanding the impact of cellular host regulation factors on NP expression in infected cells [74-77], the interactions between NP and RdRP [78] and the impact of Gn autophagy in the presence of NP in transfected cells [79]. A549 cell models have been previously used to study the consequences of NP on the cellular immunity in infected cells [80-82], lentiviral-based expression of NP [84] and to evaluate microRNA expression in HV infected cells [85]. Vero E6 cells have been extensively used for propagating HV infection in cells [86-89].

2.1.3. ANTIBODIES

Antigen	Species	App.	Dilution	Obtained from
PUUV Gc	mouse	IF	1:1000	Gift from Dr. Nicole Tischler (4G7/E10)
PUUV Gn	rabbit	IF	1:500	Abcam (ab181006)
Strep-tag II	mouse	IF	1:1000	Thermo Fisher (# MA5-17283)
ANDV Gc	mouse	IF	1:1000	Gift from Dr. Nicole Tischler (4G7/E10)

Table 2.3: **Overview of the primary antibodies used**: App.(Application) IF(Immunofluorescence)

Antigen	Conjugate	Species	App.	Dilution
mouse IgG (H+L)	AlexaFluor^{TM} 488	Goat	IF	1:1000
rabbit IgG (H+L)	AlexaFluor^{TM} 488	Goat	IF	1:1000

Table 2.4: **Overview of the secondary antibodies used**: App.(Application) IF(Immunofluorescence)

2.2. METHODS

2.2.1. CELL CULTURE AND TRANSFECTION

CHO-K1, A549, HEK 293T, BHK-21 and VeroE6 cells were maintained in Dulbecco's modified Eagle's medium containing 10% fetal bovine serum, 100 U/ml penicillin, 0.1 mg/ml streptomycin, and 4 mM L-glutamine at 37℃ and 5% CO2. Cells are passaged every 3 to 5 days, for a maximum of 13 times. All solutions, buffers, and media used for cell culture were purchased from PAN-Biotech (Aidenbach, Germany). Cells (3 to 6 x 10^5) were plated on glass-bottom 35-mm-diameter plates (CellVis, Mountain View, CA or MatTek Corp., Ashland, MA) 48 h before experiments. Fusion protein expression plasmids were transfected into (70 to 90% confluent) CHO and HEK cells using Turbofect (Thermo Fisher Scientific) and in A549, BHK-21 & VeroE6 cells using Lipofectamine 3000 (Thermo Fisher Scientific) according to the manufacturer's protocol, 20 to 24 h prior to experiments.

2.2.2. CONFOCAL FLUORESCENCE MICROSCOPY

Confocal fluorescence images were recorded with a 40x UPLS Apochromat water immersion objective (NA 1.2) at 21^{o}C on a Zeiss LSM 780 (Carl Zeiss, Oberkochen, Germany) confocal microscope with a frame size of either 512*512 pixels or 1024*1024 pixels. In this dissertation, one color & two color temporal measurements and immunofluorescence (IF) images were recorded using the confocal microscope.

For one color measurements, samples excited at 488 nm (Alexa Fluor (AF) 488 , HV constructs with mEGFP) using a CW Argon laser (Lasos, Jena, Germany) were detected in the range of 507 to 606 nm. Samples with HV constructs tagged with mCherry2 was excited at 561 nm using a laser diode and observed in the 597 to 695 nm detection range. Out-of-focus light was attenuated by using a pinhole size corresponding to one airy unit (≈39 µm). Fluorescence emission for samples excited at 488 nm was separated using a 488 nm dichroic mirror and for samples excited at 561 nm was separated using a 488/561 nm dichroic mirror.

Two color measurements in this work primarily involved HV constructs tagged with YFP and mCh2, co-expressed in cells. Measurements with 488 nm (YFP) excitation, fluorescence was detected between 499 and 562 nm and for 561 nm (mCh2) excitation, fluorescence detected between 606 and 695 nm. These ranges were chosen to avoid unspecific spectral cross-talk of the fluorescence signals. Fluorescence emission was separated using 488/561 nm dichroic mirror.

For IF imaging, samples generally contained either Hoescht staining and AF488 conjugated 2nd Ab (to detect the appropriate HV GP) or Hoescht staining, AF488 conjugated 2nd Ab and GP BD mCh2 constructs. Hoescht staining was visualized by exciting the sample at 405 nm and detected in the range of 419-508 nm. AF488 was observed by exciting the sample with 488 nm and detecting in the range of 508-561 nm and mCherry2 was visualized by exciting the sample at 561 nm and detecting in the range of 588-695 nm. Images in each fluorescence channel was sequentially taken (one at a time) to avoid signal cross-talk in the decreasing order of wavelength (excitation of 561 nm first and 405 nm excited last). Fluorescence emission for samples excited at 488 nm and 561 nm was separated using a 488/561 nm dichroic mirror and for samples excited at 405 nm was seperated using a 405/505 dichroic mirror.

2.2.3. IMMUNOFLUORESCENCE MICROSCOPY (IF)

Intracellular and cell surface staining of non-fluorescent HV GPs was visualized using IF. The protocol for incubating the antibodies (Abs) and subsequent nucleus staining is similar for the intracellular and cell surface staining. The major differences between the two staining approaches is whether the cells are (fixed/living) and (permeabilized/non-permeabilized), which is suitably highlighted as well.

While performing **intracellular IF** staining, cells were washed three times with phosphate-buffered saline (PBS) with calcium and magnesium (PAN-Biotech) and fixed with 4% paraformaldehyde (Sigma-Aldrich, Munich, Germany) for 5 to 10 min at room temperature. Cells were then washed three times with PBS before permeabilization with 0.2% Triton X-100 (Sigma-Aldrich) for 10 minutes and incubation with 2% bovine serum albumin (PAN-Biotech) for 45 to 60 min.

After three more washing steps with PBS, cells were incubated with the 1:1000 diluted primary Ab for 1 hour at 37^{o}C. Cells were subsequently washed with PBS for three times and incubated with the 1:1000 diluted secondary Ab for 45 minutes to 1 hour at room temperature. This was followed by 2x washing with PBS and staining the cells with the Hoescht dye (15 minutes incubation at room temperature (RT)) to observe the cell nucleus. The cells are then washed twice with PBS and stored in PBS for future imaging.

Cell surface immunofluorescence (**cell surface IF**) was performed in living and non-permeabilized cells. The incubation period with the primary Ab was 2 to 4 hours at 37^{o}C The rest of the procedures pertaining to incubating with 2% bovine serum albumin, the 2nd Abs and staining the nucleus with the Hoescht dye are similar to the intracellular IF staining protocol. Cells in this case, were stored in cell culture medium, prior to imaging.

GP detected	Construct	1^o Ab	2nd Ab
ANDV Gn	ANDV Strep-II GPC	anti-strep (Thermo)	Goat-anti mouse
ANDV Gc	ANDV Strep-II GPC	anti-Gc(4G7/E10)	Goat-anti mouse
ANDV Gn	ANDV Strep-II Gn + ANDV Gc BD mCh2	anti-strep (Thermo)	Goat-anti mouse
ANDV Gc	ANDV Gc + ANDV Gn BD mCh2	anti-Gc(4G7/E10)	Goat-anti mouse
PUUV Gc	PUUV Gc + PUUV Gn BD mCh2	anti-Gc(4G7/E10)	Goat-anti mouse
PUUV Gn	PUUV Gn + PUUV Gc BD mCh2	anti-Gn(Abcam)	Goat-anti rabbit
ANDV Gn	ANDV Strep-II Gn	anti-strep	Goat-anti mouse
ANDV Gc	ANDV Gc BD mCh2	anti-Gc(4G7/E10)	Goat-anti mouse
PUUV Gc	PUUV Gc BD mCh2	anti-Gc(4G7/E10)	Goat-anti mouse
PUUV Gn	PUUV Gn BD mCh2	anti-Gn(Abcam)	Goat-anti rabbit

Table 2.5: **GP Constructs and antibodies used for PM localization studies in transfected cells**: Overview of the GP constructs, antibodies and controls used for assessing PM localization in transfected cells. The negative control in each case is the cells expressing the respective GP construct and treated with the 2nd Ab alone. Goat-anti rabbit stands for Goat anti-Rabbit IgG Alexa Fluor (AF) 488 conjugated secondary antibody (Thermo Fischer) and Goat-anti mouse stands for Goat anti-mouse IgG Alexa Fluor (AF) 488 conjugated secondary antibody (Thermo Fischer). For details on primary Abs see Table 2.3. and secondary Abs see Table 2.4.

2.2.4. CONTROL EXPERIMENTS FOR CELL SURFACE IF

Specificity of HV GP expression at the cell surface using the cell surface IF protocol was validated with a set of control experiments. First, localization of α-Tubulin, an intracellular protein, was analysed using the cell surface IF protocol. Transfected (cells expressing ANDV Strep-II GPC) and non transfected CHO cells were used. Cells were treated with anti-tubulin mAb and Goat anti-mouse IgG Alexa Fluor (AF) 488 conjugated secondary antibody (Goat anti-mouse 2nd Ab). No detectable fluorescence signal was observed at the cell surface of non-transfected and transfected cells (Figure B.3 A and B).

Further, the antibodies used to detect HV GPs were analyzed for any potential artifacts (particularly non-specific binding) during cell surface IF. Non-transfected cells were treated with the respective combination of primary and secondary Abs and transfected cells (with the specific HV construct) were treated with the corresponding secondary Ab alone. No detectable fluorescence signal was observed in every such control experiment, for all combinations of HV constructs and Abs. In Figure B.3 C & D, the results of non-transfected CHO cells treated with the primary antibody (anti-Strep mAb) and secondary antibody (Goat anti-mouse 2^{nd} Ab) and ANDV Strep-II GPC transfected CHO cells treated with secondary antibody (Goat anti-mouse 2^{nd} Ab) are respectively shown. Congruent results were obtained for all control experiments conducted with other combinations of HV constructs and Abs (data not shown).

2.2.5. QUALITATIVE BOXPLOTS FOR HV GP LOCALIZATION AT PM

Images showing the HV GP localization at PM using non-fluorescent HV GP constructs in chapter 4 were magnified images with one/two cells. To substantiate that similar GP localization can be observed with multiple cells in the given sample, qualitative boxplots evaluating GP fraction were generated. For this purpose, the fluorescence signal of the cell surface expression of HV GPs was compared to their respective negative control (details regarding the negative control, see Table 2.5) in the following manner:

1. Transmission (PMT mode) and the green fluorescence channel images of each cell were collected during the confocal imaging acquisition using Zeiss software. Transmission image identifies the outer membrane region of the cell.

2. The green fluorescence channel image and the transmission channel image were exported to ImageJ as .TIFF images.

3. The polygon selection tool in ImageJ is used on the transmission image to select the Region of Interest (ROI) at the PM. Once the selection is made, "Restore Selection" option was used to make the same selection on the green channel.

4. Average fluorescence intensity in the selected region in the green channel was analysed using the Measure option

5. Mean fluorescence intensity at the selected ROI within the sample cell expressing the non-fluorescent HV construct is compared to the mean fluorescence intensity at the PM in the respective negative control (HV construct + 2^{nd} Ab, see Table 2.5 for details). The mean fluorescence intensity in the respective negative control is calculated by averaging the intensity observed at the PM of the multiple negative control cells.

6. The proportion of fluorescence intensity in the sample cell is compared to its respective negative control in the following manner:

$$\text{GP Fraction} = \frac{\text{(Mean intensity of the Sample cell ROI)- (Mean intensity of the negative control*)}}{\text{(Mean intensity of the negative control*)}} \tag{2.1}$$

The intensity in Equation 2.1 refers to the fluorescence signal intensity in the selected ROI (which is the PM region). If two cells are present in the vicinity of each other in an image, then the common region between the cells is excluded from the intensity calculations. The mean intensity from negative control is the mean of the intensities from multiple cells expressing the respective negative control (not from a single cell expressing the negative control).

The GP fraction boxplots were generated to denote that GP staining at the cell surface is not influenced by any artifacts in multiple cells. It should not be used for any quantitative comparison of the expression levels between different HV constructs accounting for the variability involved in the negative controls & Abs used (seen in Table 2.5) and the dissimilar distribution of GP expression at the PM between HV constructs. Nevertheless, these plots are a convenient qualitative indicator to show the specificity of the HV GP partition at the PM in multiple cells within a sample.

2.2.6. GIANT PLASMA MEMBRANE VESICLE PREPARATION (GPMV)

GPMVs were produced in living cells by implementing the N-ethylmaleimide (NEM) protocol for GPMV generation by Sezgin et al. (2012). Briefly, cells are washed twice and incubated for 60 to 75 mins in NEM buffer (2 to 4 mM NEM, 10 mM HEPES, 150 mM NaCl, 2 mM CaCl2, pH 7.4) at 37 °C. Afterward, the NEM buffer was replaced by the HEPES buffer (10 mM HEPES, 150 mM NaCl, 2 mM CaCl2, pH 7.4) used for all imaging experiments. For sFCS measurements, blebs that were still attached to cells were selected to avoid out-of-focus movement or drift during image acquisition.

2.2.7. PLASMA MEMBRANE LOCALIZATION (PML) CALCULATION IN GPMVS

Plasma Membrane Localization (PML) denotes the fraction of fluorescently labelled GP localized in the outer membrane of the GPMV, in comparison to the rest of the cellular volume. The value provides an quantitative estimation of the protein expression at the PM. PML analysis was completed on the GPMVs generated on cells (images of GPMVs, see Figure 4.4 B & D, chapter 4). Confocal fluorescence images of GPMVs were captured with a 40 × UPLS Apochromat water immersion objective (NA 1.2) at 21 °C on a Zeiss LSM780 (Carl Zeiss, Oberkochen, Germany) confocal microscope with a frame size of 512 × 512 pixels (further details on acquisition, refer to *Confocal fluorescence microscopy* in this chapter)

CZI images were converted into TIFF format and then exported into ImageJ. Using the polygon tool selection, the outer membrane of the GPMV (ROI-1) and the rest of the cellular volume (ROI-2) are independently selected. The threshold for the measurements are set by selecting the Threshold option in ImageJ. Once the threshold was determined, the measure option was used to calculate the mean fluorescence intensity in the respective selection.

$$\text{PML} = \frac{\text{Mean Intensity Value at ROI-1}}{\text{Mean Intensity Value at ROI-2}} \tag{2.2}$$

Thus, PML describes the ratio of average fluorescence intensity at the outer membrane of the GPMV (portion that forms the GPMV; not the cytosolic part) to the average fluorescence intensity observed in the rest of cellular volume and is normalized to each particular cell. Thus, PML

indicates the relative proportion of fluorescently labelled HV GPs partitioning at the PM compared to the rest of the cellular volume.

Positive control for the PML calculations was the myristoylated-palmitoylated (mp)-EGFP that specifically localizes at the PM, while the negative control is an ER-resident EGFP (ER-EGFP). mp-EGFP has an average PML value of 2.5 in the CHO cells. This signifies that the average intensity at the outer contour of the GPMV is 2.5 times higher compared to the average intensity obtained in the rest of the cellular volume. ER-EGFP, on the other hand, does not have any detectable intensity at the GPMV. This guarantees that the fluorescence signal observed at the GPMVs is specific to the proteins that localize at the outer membrane of the GPMVs (further details see chapter 4, Figure 4.4 E).

2.2.8. NUMBER AND BRIGHTNESS (N&B)

N&B analysis in this dissertation has been adapted from the protocol established by Dunsing [57]. 3 to 6 x 10^5 cells are plated onto 35-mm glass-bottom dishes (CellVis, Mountain View, CA or MatTek Corp., Ashland, MA) 48 h prior to the experiment and transfected as described above. Confocal images are acquired using a Zeiss LSM780 microscope. The emission and detection of different laser used for N&B has been described above in the section *Confocal Fluorescence Imaging*. The laser power was restricted to maintain the photon count rate and bleaching remained below 1 MHz and ca. 20%, respectively. Measurements that exhibited strong bleaching were discarded. Images of 128*128 pixels were acquired with pixel dimensions of 400 nm and a pixel dwell time of 50 μs. Image time-stacks of 105 scans were collected using the Zeiss cyan ZEN software. The intensity time-stacks data are analyzed using a custom-written Matlab code (The MathWorks, Natick, MA, USA), developed primarily by Dunsing [57]. The algorithm implements the theoretical framework from Digman et al. [55] for the specific case of photon-counting detectors, thus obtaining the molecular brightness and number as a function of pixel position.

Additionally, the corrections pertaining to partial bleaching, minor cell movements, calculation of final brightness values and selection of ROI, image masking for two-color measurements (where organelle staining is also recorded) are detailed extensively in the protocol by Dunsing [57] and have been adapted suitably in this dissertation.

2.2.9. CALCULATING PROTEIN MULTIMERIZATION USING N&B

N&B provides the average brightness value and the average number of molecules from the Region of Interest (ROI)/cell considered (acquistion of ROI explained in chapter 2). Absolute brightness values are then normalized against the reference monomer brightness (ϵ_m) and the fluorescence probability (ρ_m) to obtain the multimer value of the protein under consideration. Fluorescence probability (ρ_m) is additionally applied to denote the probability of the fluorescence protein to emit a fluorescence signal. ρ_m, hence imbibes the dark and bright states of the fluorophores. ρ_m is calculated by obtaining the relative ratio of absolute brightness values of the monomeric and dimeric variants of the fluorophore in the following manner:

$$\rho_m = \frac{\langle \epsilon_{dimer} \rangle}{\langle \epsilon_m \rangle} - 1 \tag{2.3}$$

Here ϵ_m is the reference monomer brightness and ϵ_{dimer} is the reference dimer brightness. ρ_m value of 1 implies that the dimer variant of the fluorophore has twice the brightness of the monomeric variant. ϵ_m and the fluorescence probability (ρ_m) is then used to calculate the multimerization value (otherwise referred to as normalized brightness). The detailed derivation to obtain ϵ_n, the average protein multimerization value, is described in detail by Dunsing et al.[57] and incorporated suitably in this work. Thus, the final formula for ϵ_n is:

$$\epsilon_n = \frac{1}{\rho_m}\left(\frac{\epsilon_i}{\epsilon_m} - 1\right) + 1 \tag{2.4}$$

where ϵ_i is the absolute brightness of the protein

Since the multimerization value is reported in terms of monomer units, it is important to ensure that concentration value is also reported in similar units. The latter is achieved by dividing the average intensity of the fluorescently labelled protein to the average brightness of the reference monomer as follows:

$$N_{conc} = \frac{\langle k \rangle}{\epsilon_m} \tag{2.5}$$

where N_{conc} is the number of molecules (in monomer units) and k is the average intensity of the fluorescently labelled protein under consideration.

2.2.10. CROSS CORRELATION NUMBER AND BRIGHTNESS (CCN&B)

The ccN&B implementation has been adapted from the protocol established by Petrich et al.[59] and modified suitably for the evaluation within the cytosolic region of the cell. Briefly, an image stack is acquired over time at a fixed position in the sample typically consisting of 100 frames. Frame size of 256 x y (where y<=256) are utilized for obtaining the images using a pixel size of 0.208 μm and a pixel dwell time of 12.6 μs and alternating two different excitation wavelengths. Laser powers are kept low enough to restrict bleaching below 20 % of the initial fluorescence signal (typically ≈3 μW for 488 nm, and ≈5 μW for 561 nm). CZI image output and TIFF files of the CZI images were imported into MATLAB using the Bioformats package and analyzed using a custom-written MATLAB script implementing the equations from Digman et al. [58] for the specific case of photon-counting detectors, thus obtaining the molecular brightness and number as a function of pixel position. Pixels corresponding to the ROI are manually selected in an image map. To distinguish the fluorescence signals independently, fluorescence intensities above 1MHz were discarded. To correct for lateral drift during the acquisition, frames are aligned to the first frame by maximizing the spatial correlation between sub-selections in consecutive frames, averaged over both channels, as a function of arbitrary translations [33]. The brightness-intensity maps show the pixel brightness with a color code in units of counts/dwell time/molecule. The average fluorescence count rate (counts/dwell time) was represented as pixel intensity. The details regarding corrections for bleaching, minor cell movements & specific detector response and relative cross correlation calculations are expounded further in Petrich et al. [59] and adapted in this work suitably.

2.2.11. POINT FLUORESCENCE CORRELATION SPECTROSCOPY (PFCS)

pFCS performed in this work has been adapted from the protocol established by Petrich et al. [59] and the workflow is briefly discussed here. pFCS measurments are taken for 120 s on a

Zeiss LSM780 microscope and recorded using the Zen Black software module. mCherry2 was excited at 561 nm using a laser diode and observed in the 578 to 695 nm detection range. Laser powers were optimized to limit photobleaching below 20%. Confocal pinhole size was set to 1 airy unit (A.U). To calibrate the confocal volume, pFCS measurements with AF 488 in water at 50 nM were performed at the same laser power. Each measurement with 12 repetitions of 10 s was performed. The resultant ACF function was fitted as described by Dunsing [57] to obtain the structural parameter S and τ_{Diff}. Details on the data analysis of pFCS measurements have been described in the supplementary information section of Petrich et al. [59].

pFCS measurements were performed on cells expressing PUUV GP mCh2 to calculate the concentration of GP using the concentration of mCherry2 in chapter 3. mCherry2 concentration was calculated by assuming homogeneous distribution of the fluorophore in the cellular volume under consideration. The calculation of the mCherry2 concentration obtained from pFCS measurements in the GA, is described in the next section.

2.2.12. CALCULATION OF GP CONCENTRATION IN GA USING PFCS

Evaluation of GP concentration in GA using pFCS is elaborated in my publication "*Detection of Envelope Glycoprotein Assembly from Old World Hantaviruses in the Golgi Apparatus of Living Cells*" [90]. Here, a brief outlook is provided.

GP (encoded in the BD mCh2 construct) concentration in the GA is calculated by initially measuring the number of soluble mCherry2 discerned in the considered confocal volume (N_{mCh2}) using pFCS. Next, the complimentary number of GPs in the same confocal volume (N_{GP}) is calculated as follows:

$$N_{\text{GP}} = \frac{N_{\text{mCh2}}}{\text{BD expression ratio of GP:mCherry2}} \tag{2.6}$$

Next, the GP is assumed to reside either in the ER or the GA. This permits the description of a partition co-efficient ζ which is defined as:

$$\zeta = \frac{N_{\text{GA}} * A_{\text{GA}}}{(N_{\text{GA}} * A_{\text{GA}}) + (N_{\text{ER}} * A_{\text{ER}})} \tag{2.7}$$

where N is the average number of GPs in the defined illumination volume and A is the apparent area occupied by the ER/GA. This partition ζ is calculated from single color N&B measurements and the details of the procedure are described in .

Thus, on obtaining this ζ, the estimated number of GPs in the confocal volume encompassing only the GA is given by:

$$N_{\text{GP-pFCS}} = \frac{N_{\text{GP}} * \zeta * V_{\text{cell}}}{V_{\text{GA}}} \tag{2.8}$$

Here, $V_{\text{GA}}/V_{\text{cell}}$ was approximated to 0.04.

This formulation was used in chapter 3 to calculate the Gn (or Gc) concentration at the GA, when it was encoded in the BD mCh2 construct.

2.2.13. SCANNING FLUORESCENCE CORRELATION SPECTROSCOPY (sFCS)

The one color sFCS protocol applied in this thesis has been adapted from the protocol established by Dunsing [57]. In brief, line scan of 256 × 1 pixels (pixel size 80 nm) was performed perpendicular to the GPMV membrane with a 403.20 µs scan time. Typically, 250,000–400,000 lines were acquired (total scan time ≈ 2–4 min) in photon counting mode. Laser powers were adjusted to keep depletion due to photobleaching below 20%. Typical laser power values were ≈ 1.8 µW for GPMV measurements. The fluorescence fluctuation signal was maximized by selecting cells with the lowest detectable protein expression. Scanning data is exported as TIFF files and analyzed in MATLAB (MathWorks, Natick, MA) using custom-written code, developed primarily by Dunsing [57]. sFCS analysis follows the procedure described in Ries and Schwille [60]. Further details on the averaging of the line scans, selection of ROIs, corrections on photobleaching, calibrating the focal volume and brightness calibration is explained in detail by Dunsing [57] and in Ries and Schwille [60].

GP multimerization in the GPMVs can be calculated using Equation 2.4. Surface concentration of the GP residing in GPMVs is calculated as follows:

$$\text{Surface Concentration}_{\text{protein}} = \frac{N_{\text{conc}}}{\rho_m \pi \omega_0^2 S} \tag{2.9}$$

where ω_0 represents the waist diameter of the confocal volume and S is the shape parameter, which is the ratio of the vertical and lateral dimension of the confocal ellipsoid. S is usually around 5 to 9.

3

Hetero-Interactions of Hantavirus Glycoproteins essential for Spike Formation

3.1. Motivation

Hetero-interactions between HV GPs drives the formation of the GP spike assembly. Huiskonen et al. [91], on performing electron cryotomography (CT), observed the association of Gn as homotetramers and that of Gc as homodimers. This led to a 4-fold symmetry prediction of the spike complex, with each spike containing four copies of both GPs. The organization of the spike and molecular interactions between Gn and Gc were further elaborated by Serris et al. [24]. They fitted the X-ray structures of the soluble ectodomains of the ANDV and Maporal virus (MAPV) Gn^H/Gc and observed that the tetrameric spikes of HV GPs are initially formed in the ER before getting transported to GA. Bignon et al. [37] showed that HV spikes exhibit a dynamic equilibrium between closed and open forms and that the spike must remain preferentially in the closed form to generate Gc homotrimers and for membrane fusion to occur.

Hepojoki et al. [43] proposed two possible models for the hetero-oligomeric formation of the GP spikes. Model 1 suggests that Gn proteins form the tetrameric Gn complex initially. This acts as a precursor for Gc to come into contact with the Gn complex and form the overall $(Gn\text{-}Gc)_4$ spike complex. Model 2 proposes that heterodimeric Gn-Gc subunit is initially generated. This sub-unit oligomerizes with congruent Gn-Gc units to create the final $(Gn\text{-}Gc)_4$ spike complex. Despite best efforts, there is a lack of quantitative analysis to prove which assembly model accurately describes the spike formation in cells. In this chapter, experimental approaches were performed to systematically assess the Gn-Gc interactions that direct the formation of spike complexes within a living cell. This was achieved by expressing PUUV GPs constructs in CHO cells. Suitability of CHO cells have been discussed in chapter 2. The results from this analysis would enable us to state conclusively which Hepojoki models [43] appropriately describes the generation of the GP spike.

Findings from this chapter have been published in the Journal of Virology under the title "*Detection of Envelope Glycoprotein Assembly from Old-World Hantaviruses in the Golgi Apparatus of Living Cells*" [90]. Certain results obtained by my colleague Roberto for this article were used for designing new experiments performed in this chapter. Those results will be referenced as "*Previous work by Roberto*".

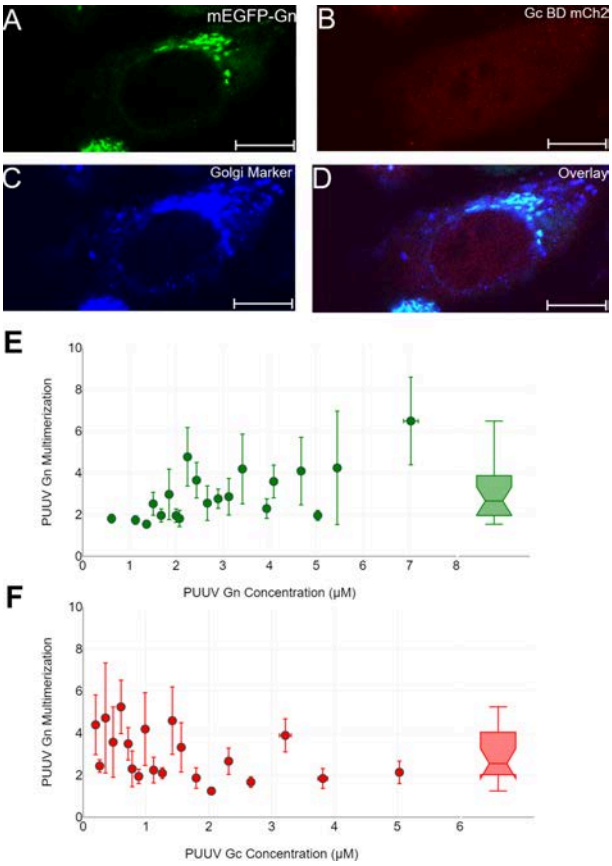

Figure 3.1: **Concentration-dependent multimerization of PUUV Gn in the presence of PUUV Gc in CHO cells**: Representative images of CHO cells co-expressing PUUV mEGFP-Gn, Golgi-Turq and PUUV Gc BD mCh2 24 hpt. Expression of [A] PUUV mEGFP-Gn, [B] of PUUV Gc BD mCh2 and [C] of Golgi-Turq (Golgi Marker) and [D] the overlay of all the fluorescence signals [A] to [C] in the same CHO cell. PUUV mEGFP-Gn multimerization as a function of [E] PUUV mEGFP-Gn or [F] unlabelled PUUV Gc concentration was obtained by performing N&B analysis. Gc concentration in the GA was calculated using pFCS measurements (details see, chapter 2). Analysis was restricted to cells showing significant expression of mCherry2. Each scatter point represents multimerization/concentration value, that is calculated by averaging five cells with similar protein concentrations by applying equal frequency binning. Error bars denote = standard error of mean (SEM). For raw data of the plots in [E] and [F] see Figure A.1. Each data set was obtained from at least 4 separate experiments. The right panel insert shows the multimerization data points grouped per category, in the form of notched box plots. Scale bars are 10 µm.

3.2. RESULTS

3.2.1. PUUV GN FORMS LARGER MULTIMERS IN THE GOLGI APPARATUS IN THE PRESENCE OF PUUV GC

Gn:Gc interaction upon co-expression of GPs in CHO-K1 cells was analysed by measuring the GP multimerization state via N&B analysis. Gn and Gc were encoded in separate cDNAs due to the cloning difficulties in generating fluorescently labelled PUUV GPC. Expression of fluorescently tagged Gn and Gc resulted in the enrichment of GPs in the GA. Surprisingly, no Gn multimers larger than tetramers were detected even at high Gn concentration (*Previous work by Roberto*). The restricted Gn multimerization was credited to the steric hindrance of the FPs fused to the GPs. To circumvent this limitation, an alternative strategy was adopted. An *in cellulo* assay was developed to estimate the amount of fluorescently labelled and unlabeled GPs upon co-expression. The unlabelled GP was encoded in the BD vector and the mCherry2 concentration was used to calculate the GP concentration.(details on the BD vector, see chapter 2) .

CHO cells were transfected with PUUV mEGFP-Gn and PUUV Gc BD mCh2 (Figure 3.1 A to 3.1 D). Gn was significantly enriched in the GA. PUUV mEGFP-Gn multimer state as a function of its concentration showed upto octamers, (Figure 3.1 E) on average, (the average after data binning) in the GA. Interestingly, the multimerization values of PUUV mEGFP-Gn in the presence of PUUV Gc BD mCh2 did not plateau at large Gn concentrations. Finally, no correlation was obtained between PUUV mEGFP-Gn multimerization and the concentration of unlabeled PUUV Gc (Figure 3.1 F).

3.2.2. PUUV GC MULTIMERIZATION INCREASES IN THE PRESENCE OF PUUV GN

Furthermore, the PUUV mEGFP-Gc multimerization in the presence of PUUV Gn BD mCh2 was investigated. The molecular brightness of PUUV mEGFP-Gc in the GA (Figure 3.2 A to 3.2 D), was significantly enhanced and Gc multimerization values ranged, between two and four (Figure 3.2 E) on average (the average is after data binning). No correlation was obtained between the multimerization behavior of PUUV mEGFP-Gc with its concentration (Figure 3.2 E) and with the concentration of unlabelled PUUV Gn (Figure 3.2 F).

3.3. DISCUSSION

Formation of Gn:Gc hetero-complexes is an vital step in the assembly of new HV virions in infected cells. Despite their relevance, constrained information exists regarding the hetero GP interactions that directs the formation of GP spike. This chapter presents a quantitative assessment of the Gn:Gc interactions that conduct the multimeric spike complex formation in living cells.

HV assembly in physiological conditions requires co-expression of Gn and Gc. Gn and Gc expressed together (from a single GPC, separate cDNAs, or in the infection context) for the HTNV [92][93], PUUV [66], ANDV and SNV [94][95] strains co-localized in the GA. In this study, the GP multimerization state was quantified with respect to its subcellular partition, its concentration, and the concentration of its interacting GP partner.

PUUV GPs fused with fluorescent proteins at the N-terminus were enriched in the GA. Gn did

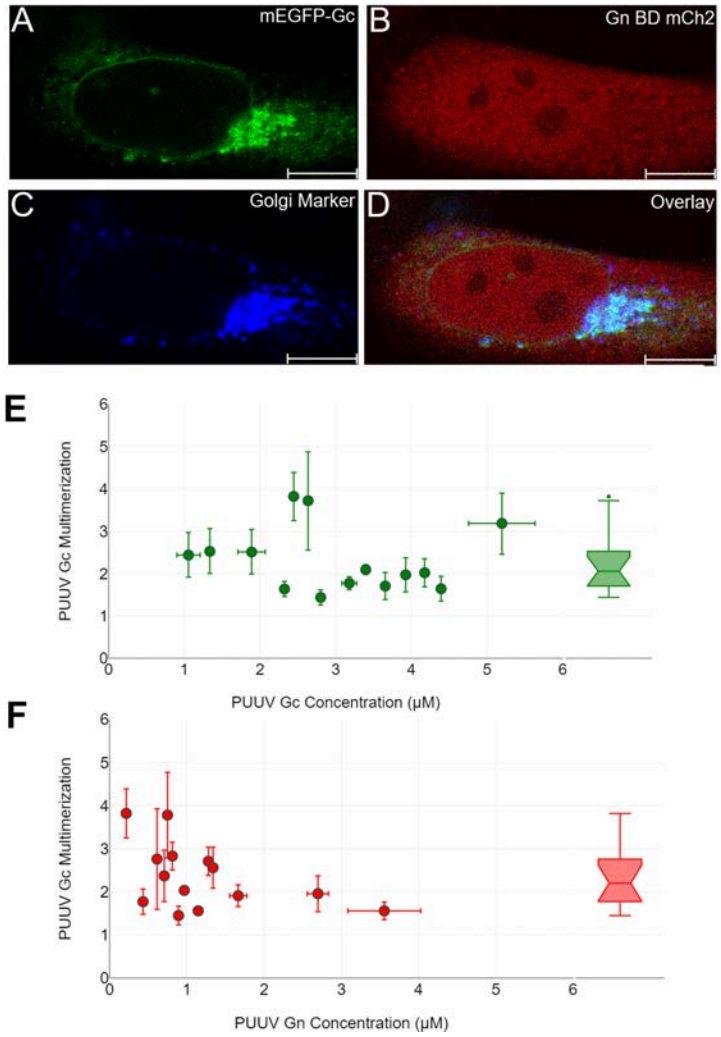

Figure 3.2: **Concentration-dependent multimerization of PUUV Gc in the presence of PUUV Gn in CHO cells**: Representative images of CHO cell co-expressing PUUV mEGFP-Gc, Golgi-Turq (Golgi Marker) and PUUV Gn mCh2 BD 24 hpt. Expression of [A] PUUV mEGFP-Gc, [B] of PUUV Gn BD mCh2 and [C] of Golgi-Turq (Golgi Marker) and [D] the overlay of all the fluorescence signals [A] to [C] in the same CHO cell. PUUV mEGFP-Gc multimerization as a function of [E] mEGFP-Gc or [F] unlabelled PUUV Gn concentration was obtained by performing N&B analysis. PUUV Gn concentration in the GA was calculated from pFCS measurements (details see, chapter 2). Analysis was restricted to cells that showed significant expression of mCherry2. Each point represents the average of multimerization/concentration values calculated by averaging three to four cells with similar protein concentrations using equal frequency binning. Error bars = standard error of mean (SEM). For raw data of the plots in [E] and [F] see Figure A.2. Each data set was obtained from at least 4 separate experiments. The right panel insert shows the multimerization data points grouped per category, in the form of notched box plots. Scale bars are 10 μm.

not form oligomers greater than tetramers even at high Gn concentrations with this assay. This was credited to the steric hindrance generated by the fluorescent tag present on the N terminus

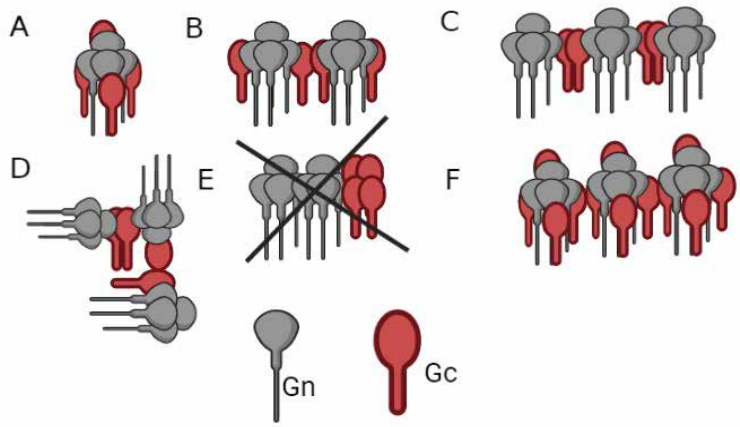

Figure 3.3: **Schematic examples of Gn-Gc hetero-multimers compatible and incompatible with the highest observed multimerization states in cells expressing both Gn and Gc**: [A] to [D] Hetero-multimers containing 4 Gc units and up to 12 Gn units. [E] Gn-Gc arrangement containing a Gn homo-octamer linked to a Gc tetramer. [F] Gn-Gc hetero-octamers connected via Gc:Gc contacts. Further details refer text and [90].

of Gc (*Previous work by Roberto*) [90]. Nevertheless, this experimental outcome demonstrated that relatively small Gn-Gc hetero-oligomers (Gn being monomeric or dimeric on average) was sufficient for Gn transport to the GA and that Gn-Gc interactions did not mandate the prior formation of Gn homo-tetramers. This was in direct disagreement with assembly model 1 proposed by Hepojoki et al. [43] where, the formation of Gn tetramers, is the precursor for Gc to interact with Gn to generate the GP spike assembly.

Limitations arising from steric hindrance of fluorophore tags were overcome by a novel approach to monitor the interactions between the fluorescent labelled GP and unlabeled GP. Using this strategy, Gn formed large multimers containing up to octamers (after data binning; Figure 3.1 E), in the presence of (non-fluorescent) Gc (Gn on singular expression forms up to tetramers [90]). Gn multimerization did not plateau for the highest concentrations observed. This suggests that even larger Gn multimers are present in the samples and the observed multimerization is an average estimate. Furthermore, the weak correlation between Gn multimerization and Gc concentration indicated that the formation of Gn complexes (complexes refer to large Gn subunits) did not require preformed Gc:Gc dimeric association. Instead, the findings support the notion that Gn and Gc associates at low concentration, subsequently allowing the formation of higher-order Gn-Gc units.

Gc, in the presence of (non-fluorescent) Gn, formed ca. up to tetramers (after data binning; Figure 3.2 E). This indicated that Gc multimers greater than dimers (Gc on singular expression forms up to dimers [90]) would require the mediation by Gn oligomers. This additionally suggests that associations between Gn tetramer units must be mediated by Gc. Gc complexes with approximately four units diffusing together can be explained using several Gn-Gc configurations (Figure 3.3 A to D). They are in consonance with the high multimeric states for Gn. Alternative

spatial combinations of Gn-Gc hetero-multimers (e.g., the large Gn homo-multimer linked to a Gc homo-tetramers in Figure 3.3 E) would not be compatible because the largest Gn (or Gc) homo-oligomers observed in the absence of the other GP, was tetramers (or dimers).

Limited Gc multimerization in the presence of Gn could be attributed to the presence of the N-terminal fluorescent tags. This implies that in the absence of FPs, more Gc monomers would be present in Gn-Gc hetero-multimers. Nevertheless, these findings complement the proposed GP organization on the viral surface, where Gn tetramers are connected via Gc:Gc contacts [24] [31] [33] [43]. Finally, the lack of correlation between Gc multimerization and Gn concentration highlights that the assembly model 1 [43] cannot be entirely accurate, since that would require the formation of Gn multimers (at higher Gn concentrations) for Gc multimerization to occur.

3.4. CONCLUSION

The experimental findings in this chapter proves the assembly model 2 by Hepojoki et al. [43], which involves the formation of Gn-Gc heterodimeric subunit, appropriately describes the GP spike formation observed in living cells. Gn-Gc hetero-dimers were formed initially in the ER. These heterodimers then interact to form the final GP spike and later are translocated to the GA. Gn-Gc interactions drive the formation of the hetero-octameric complex and Gc stabilizes contacts between neighboring GP spikes. The GP assembly into continued larger complexes was reasonably constrained by the presence of FPs in the experiments performed in this work. Despite this shortcoming, these results finally provide a direct evidence for the first steps of OWHV assembly in the GA of living cells.

4

Plasma Membrane Localization of Hantavirus Glycoproteins

4.1. Motivation

Most bunyaviruses (including HVs) assemble at the GA [96]. In contrast, assembly of GPs at the PM is hypothesized as an unique feature of the NWHV strains [83]. Goldsmith et al. [97] showed that the virus budding of Sin Nombre Virus (SNV) entirely took place at the PM of infected Vero E6 cells using thin section EM and immuno-EM. Rakov et al. [98] observed that Black Creek Canal Virus (BCCV) GPs were expressed at the PM at the apical surface of polarized Vero C1008 infected cells using EM and concluded that the American HVs associated with HPS mature at the PM. Spiropoulou et al. [94] detected SNV GPs at the cell surface at later time points post transfection (24 to 36 hours) and post infection (5 days). Cifuentes-Muñoz et al. [99] observed upon expressing ANDV GPC, encoded in a lentiviral expression system, in HEK 293T cells that Gn multimers up to tetramers and Gc monomers partitioned at the PM. The same group further discovered the peptide segment in Gc that is responsible for cell-cell fusion [100] and showed that the post fusion Gc homotrimer occurs at low pH [101].

Interestingly, anecdotal observations of GP localization at cell surface were also obtained with OWHV strains. Ogino et al. [102] demonstrated that the HTNV GP localization at the PM is dictated by low pH and by the cell line used. Disruption of the Gc glycosylation site was also shown to inhibit the cell-cell fusion of HTNV GPs [103]. Sperber et al. [66] showed that fluorescently labelled PUUV GPs on individual expression were detected at the cell membrane and examined how truncated Gc-CT domain influences the PM expression of PUUV Gc. Slough et al. [104] showed that HTNV GPs (encoded in a Vesicular Stomatitis Virus (VSV) based expression system) has significant PM localization after introducing single point mutations in Gn-CT and Gc. Parvate et al. [105] noted tubular projections and budding at the PM for HTNV and ANDV infected Vero E6 cells, six to nine days post infection (dpi). Gallo et al. [106] observed localization of TULV Gn at the PM of infected Vero E6 cells.

These findings indicate that assembly of GPs at the PM could be similarly observed across all HV strains. Gallo et al. [106] attempted a systematic comparison between OWHV (PUUV, Tula HV (TULV) and NWHV (Prospect Hill HV (PHV)) infected cells to understand the cell surface expression of HV GPs. Significant expression of TULV Gn was detected at the PM, similar to the findings of Spiropoulou et al. [94]. Limited viral production with PUUV and PHV infected cells resulted in non appreciable GP expression at PM.

In this chapter, cells expressing GPs of OWHV and NWHV were systematically compared, since cell surface localization was previously obtained with HV GPC transfected cells [94] [102]. This alternative strategy does not suffer the limitations of restricted viral production (due to slow HV replication cycle, as seen in Gallo et al.(2022)). It additionally elucidates the intrinsic behavior of GPs at the PM and distinguishes the role of other HV proteins in the potential viral assembly at the cell surface.

The following aspects of the HV GP localization at the PM were addressed in this chapter using ANDV and PUUV strains primarily:

1. Does non-fluorescent OWHV and NWHV GPs localize at the PM upon co-expression ?

2. Are non-fluorescent HV GPs transported to the PM upon singular expression ?

3. Do GPs form large spike assemblies at the PM ? If yes, what mechanistic model describes this assembly appropriately ?

4. Is GP localization at the PM influenced by disruption of cytoskeletal factors ?
   Here the HTNV strain was additionally assessed, since PM localization of HTNV GPs has been previously reported (Ogino et al. [102]).

These investigations would expand the knowledge on the mechanisms that govern the assembly of HV GPs at the PM and highlight possible differences, if any, between OWHV and NWHV GP partition at the PM.

To answer the above questions, the cell surface expression of non-fluorescent ANDV and PUUV GPs was initially analysed using IF analysis. Further, it was evaluated if non-fluorescent Gn and Gc partition at the PM upon independent expression. Next, the dynamics of the GP assembly at the PM was analysed by expressing fluorescently labelled constructs. Protein multimerization of ANDV Gn and Gc at the PM was evaluated upon co-expression using N&B analysis. Finally, GPMV, an approximate model membrane system, was generated to analyse the GP dynamics at the PM, particularly in the absence of cytoskeletal factors. All observations in this chapter were recorded 24 hours post transfection (hpt) of the respective HV construct. A different time point will be suitably mentioned. The appropriateness of the cell models (CHO, Vero and A549) used in this chapter have been discussed earlier in chapter 2. Additional results pertaining to this chapter are shown in Appendix B.

4.2. RESULTS

4.2.1. NON-FLUORESCENT ANDV AND PUUV GPS PARTITION INTO THE PM UPON CO-EXPRESSION

Cell surface localization of non-fluorescent ANDV GPs in CHO cells was analyzed by expressing ANDV Strep-II GPC. ANDV Gn localization was observed using anti-strep mAb (since the Strep-II tag is attached to Gn domain, referred to as Gn* mAb) and Goat anti-mouse 2nd Ab, while that of ANDV Gc was detected using an anti-Gc mAb (4G7/E10) and a Goat anti-mouse 2nd Ab. Discrete punctuate staining of ANDV Gc (Figure 4.1 A & Figure B.4 A) and ANDV Gn (Figure 4.1 C & Figure B.4 B) was detected at the cell surface. Similar observations were obtained upon expressing ANDV Strep-II GPC in A549 cells (Figure A.5 A & C).

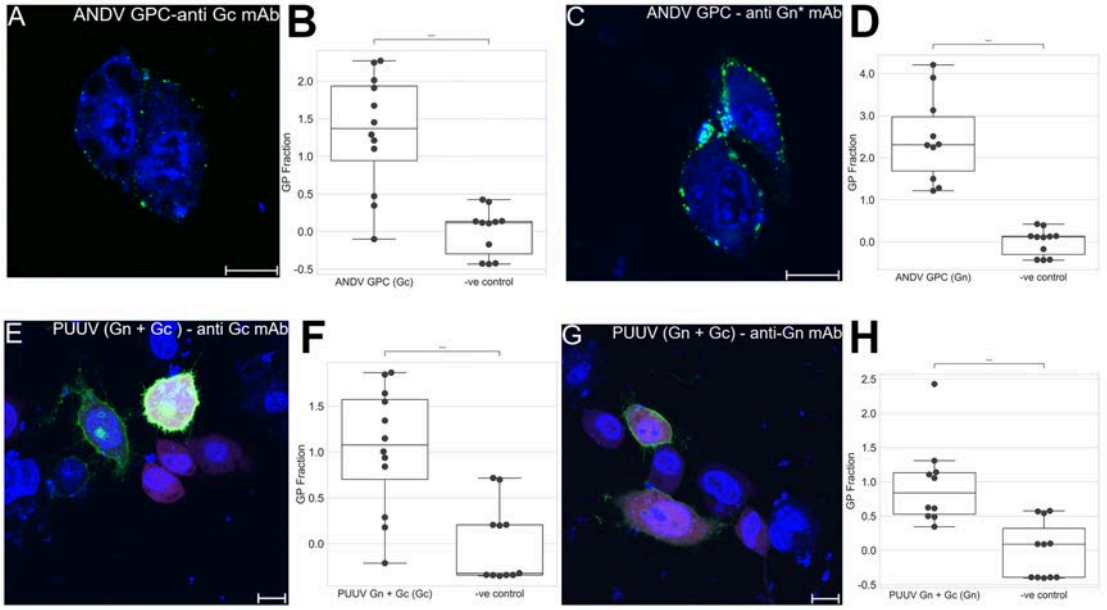

Figure 4.1: **Cell surface expression of non-fluorescent ANDV and PUUV GPs in CHO cells**: ANDV and PUUV Gn & Gc localization at the PM upon co-expression of GPs in CHO cells was evaluated using cell surface IF. The nucleus was visualized using Hoechst staining (purple). Red channel in [E] and [G] denotes the respective GP BD mCh2 construct. ANDV GP localization was assessed by expressing ANDV Strep-II GPC. Representative image of the cell surface localization of [A] ANDV Gc and [B] ANDV Gn. [E] Representative image of the cell surface localization of PUUV Gc upon co-expressing PUUV Gc and PUUV Gn BD mCh2 [G] Representative image of the cell surface localization of PUUV Gn respectively after co-expressing PUUV Gn and PUUV Gc BD mCh2. PM localization of [B] ANDV Gc [D] ANDV Gn [F] PUUV Gc and [H] PUUV Gn was compared against their respective negative control using GP Fraction parameter and presented as box plots (details and significance of the box plot, see chapter 2). Each point in the scatter plot represents one cell. Minimum of 10 individual cells were considered for each boxplot. Scale bars are 10 µm. Significance was determined by t-test, P**** ≤ 0.001

Next, ANDV GP partition at the PM was assessed upon co-expression of GPs from separate cDNAs in CHO cells. GP co-expression from separate cDNAs helps to avoid practical cloning

and transfection difficulties with full-length GPC. Localization of ANDV Gc was assessed by co-expressing ANDV Gc and ANDV Gn BD mCh2 and that of ANDV Gn was assessed using ANDV Strep-II Gn and ANDV Gc BD mCh2. This approach permits the acquisition of cells where both the GPs are localized. ANDV GPs were detected at the PM using this strategy (Figure B.2). Thus, ANDV GPs localized at the PM upon expression from a single GPC and co-expression of GPs from separate cDNAs.

Further, the PM localization of PUUV GPs was evaluated in CHO cells. Cell surface localization of PUUV Gc was analysed by expressing PUUV Gc and PUUV Gn BD mCh2 and treating the cells with anti-Gc mAb (4G7/E10) and a Goat anti-mouse 2^{nd} Ab. Cell surface expression of PUUV Gn by co-expressing PUUV Gn and PUUV Gc BD mCh2 and treating the cells using anti-PUUV Gn MAb (Abcam) and a Goat anti-rabbit IgG AF488 conjugated secondary antibody (Goat anti-Rabbit 2^{nd} Ab). PUUV Gc (Figure 4.1 E & Figure B.4 C) and PUUV Gn (Figure 4.1 G & B.4 D) also showed discernible partition at the PM. Congruent results were also obtained with A549 cells (Figure B.5 E & G).

Altogether from these findings, ANDV and PUUV GPs have discernable localization at the PM, independent of the cell model used. ANDV GPs were detected upon expression from a single GPC and from seperate cDNAs.

4.2.2. NON-FLUORESCENT ANDV GPS AND PUUV GC PARTITION INTO THE PM WHEN EXPRESSED SINGULARLY

Furthermore, non-fluorescent ANDV and PUUV GPs localization at PM, upon individual expression, was assessed. Previous studies with SNV [94] and HTNV GPs [102] concluded that GP co-expression was essential to transport the GPs to the PM. However, Sperber et al. [65] detected weak localization of fluorescent labelled PUUV Gn and PUUV Gc at the PM upon individual expression in CHO cells. These contradictory results prompted the evaluation of GP partition at the PM upon independent expression. ANDV Strep-II Gn, ANDV Gc BD mCh2, PUUV Gn BD mCh2 and PUUV Gc BD mCh2 were independently expressed to visualize the localization of ANDV Gn, ANDV Gc, PUUV Gn and PUUV Gc respectively. The 1^{o} and 2^{nd} Abs used for the visualization of ANDV and PUUV GPs at the PM have been described in the previous section. ANDV Gc (Figure 4.2 A), ANDV Gn (Figure 4.2 C) and PUUV Gc (Figure 4.2 E) were significantly detected at the PM of CHO cells. Interestingly, PUUV Gn did not show any detectable cell surface localization (Figure 4.2 G). Complimentary results were also obtained upon individual expression of ANDV and PUUV GPs in A549 cells (Figure B.6).

Based on these findings, ANDV Gc and ANDV Gn have detectable PM localization upon independent expression, for all cell models tested. Interestingly for PUUV, only Gc was visualized at the PM upon singular expression.

4.2.3. FLUORESCENT ANDV GPS PARTITION MOSTLY IN INTRA-CELLULAR COMPARTMENTS TO FORM LARGE MULTIMERS

Fluorescently labelled ANDV GPs were expressed in CHO cells to assess whether large GP assemblies are formed at the PM. Previous studies have shown that the fluorescence tagging does not generate artifacts with respect to HV GP localization [107]. Upon independent expres-

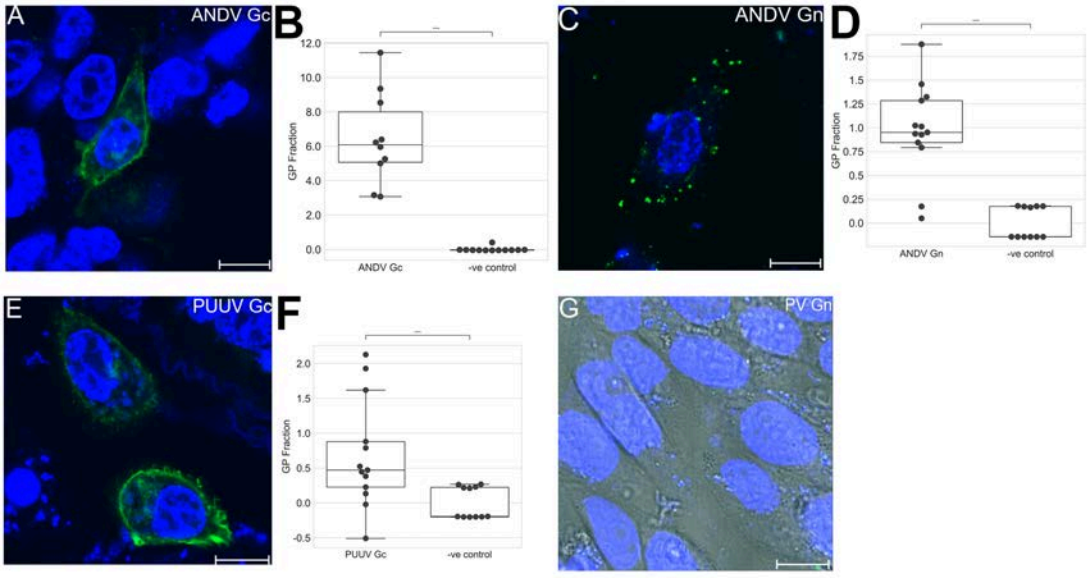

Figure 4.2: **Cell surface localization of untagged ANDV and PUUV GPs upon individual expression in CHO cells**: ANDV and PUUV Gn & Gc localization at the PM upon individual expression of GPs in CHO cells was evaluated 24 hpt using cell surface IF staining. The nucleus was visualized using Hoechst staining (purple). Representative image of the cell surface localization of [A] ANDV Gc, [B] ANDV Gn, [E] PUUV Gc and [G] PUUV Gn. PM localization of [B] ANDV Gc [D] ANDV Gn [F] PUUV Gc and [H] PUUV Gn was compared against their respective negative control using GP fraction parameter and presented as box plots (details on the box plot, see chapter 2). Scale bars are 10 µm. Each point in the scatter plot represents one cell. Minimum of 10 individual cells were considered for each boxplot. Significance was determined by t test, P**** ≤ 0.001

sion, ANDV mEGFP-Gn and ANDV mEGFP-Gc were enriched primarily at the ER (Figure B.7).

Upon expression of fluorescently labelled ANDV GPC constructs in CHO cells, ANDV Gn and ANDV Gc primarily localized around the perinuclear region (Figure 4.3 A & 4.3 C), even for extended transfection times (120hpt) (Figure 4.3 B & 4.3 D). No detectable PM localization was observed. ANDV GP assemblies at the perinuclear region was assessed quantitatively using N&B. ANDV mEGFP-GPC and ANDV GPC-mEGFP were used to calculate the ANDV Gn and ANDV Gc multimerization, respectively. The data showed, within the explored ANDV GPC concentration range, that Gn forms large multimers (up to ca. 12 subunits on average). Gc, on the other hand, formed smaller complexes containing on average up to four subunits (Figure 4.3 E). This indicated large ANDV GP spike assemblies are formed at the perinuclear region when ANDV Gn and Gc are co-expressed.

Thus, ANDV GPs formed large spike assemblies at the perinuclear region, similar to their OWHV counterparts. Interestingly, fluorescently labelled ANDV GP constructs did not yield any distinct PM localization, even after longer time periods post transfection.

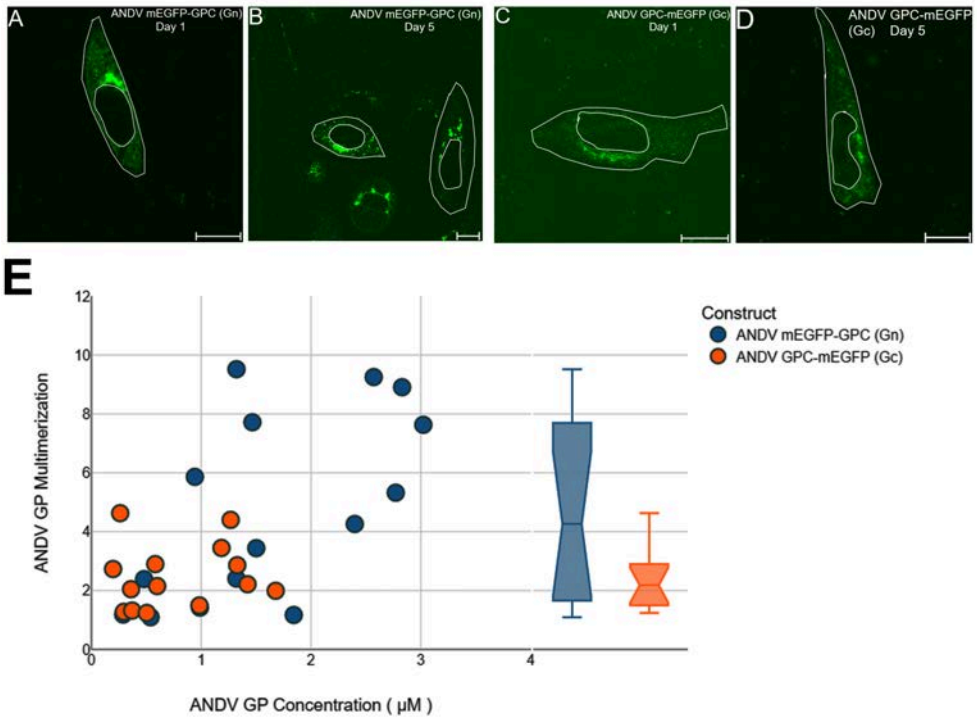

Figure 4.3: **Intra-cellular localization and multimerization state of fluorescent ANDV GPC in CHO cells**: Representative image of ANDV mEGFP-GPC expression observed after [A] 24 hpt (Day 1) and [B] 120 hpt (Day 5). Representative image of ANDV GPC-mEGFP expression observed after [C] 24 hpt (Day 1) and [D] 120 hpt (Day 5). Images are contrast enhanced for clear visualization. [E] Concentration dependent multimerization analysis of ANDV Gn (blue) and Gc (orange) upon expression of ANDV mEGFP-GPC and ANDV GPC-mEGFP respectively. This was evaluated using N&B. Each point in the graph represents the average multimerization in one cell. 14 cells considered for ANDV GPC-mEGFP and 15 cells for ANDV mEGFP-GPC. The right panel shows the multimerization data points grouped per category in the form of notched box plots. Scale bars are 10 µm.

4.2.4. FLUORESCENTLY LABELLED HV GC WEAKLY PARTITIONS INTO GIANT PLASMA MEMBRANE VESICLES

PM localization of fluorescently labelled HV GPs was observed with improved sensitivity, by generating GPMVs in cells. GPMVs are vesicular protrusions in which the PM is momentarily detached from the actin cortex. This permits the investigation of protein dynamics at the PM within its conserved lipidome and proteome [108]. GPMVs are commonly featured during cellular apoptosis, cell migration and even used by viruses for cellular entry [109] [110]. They are devoid of cytoskeletal factors particularly intermediate filaments and F-actin [111] [112]. Regime of GPMVs utilized in this work is when its growth phase recedes and the outer cortex starts to reform. Fluorescent labels like GFP have been used to study the GPMV dynamics and are known to cause no artifacts on protein localization [112-116]. Blebbed CHO cells as demonstrated in Figure 4.4 B and 4.4 D were chosen for analyzing the GP dynamics in GPMVs.

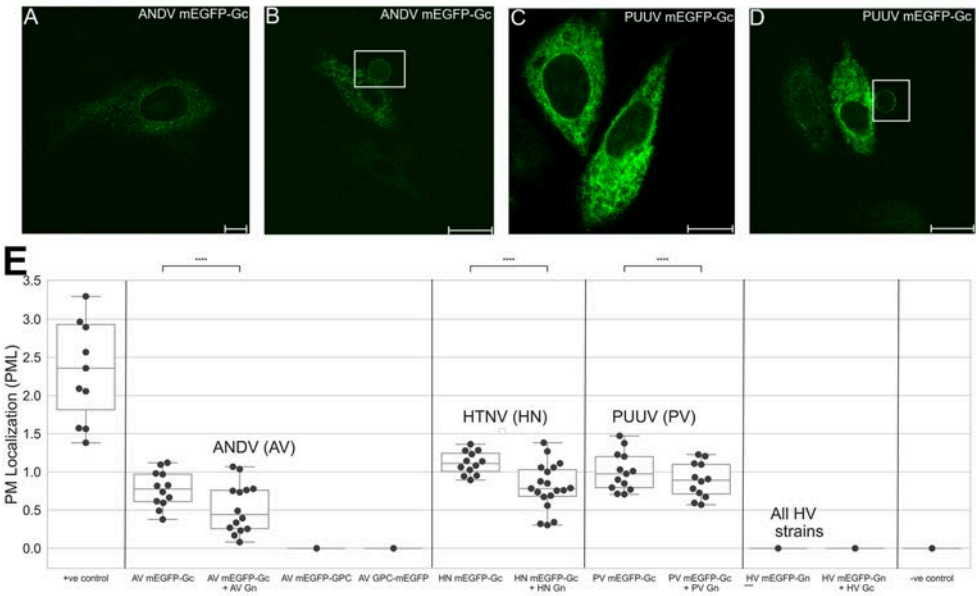

Figure 4.4: **ANDV, HTNV and PUUV Gc partitions weakly into GPMVs after expression in CHO cells**: Representative image of cell expressing ANDV mEGFP-Gc [A] before and [B] after the formation of GPMVs. Cells expressing PUUV mEGFP-Gc 24 hpt [C] before and [D] after the formation of GPMVs. White boxes in panels [B] and [D] highlight the GPMVs considered for PML analysis. [E] PML analysis for different HV construct combinations expressed in CHO cells 24 hpt. The untagged HV construct is encoded in the BD mCh2 plasmid. The single cell points for the CHO cells expressing ANDV mEGFP-GPC, ANDV GPC-mEGFP, HV mEGFP-Gn, HV mEGFP-Gn + HV Gc and –ve control (ER-EGFP) are representative of their PML value. The single points shown for the other constructs in this figure represent one cell. Minimum of 10 individual cells were considered for the boxplots with multiple scatter points. Scale bars are 10 µm. Significance was determined by t-test, P**** ≤ 0.001.

Average expression of fluorescently labelled HV constructs at the GPMVs was examined using the parameter PML. It indicates the relative proportion of fluorescently labelled HV GPs partitioning at the GPMV compared to the rest of the cellular volume (details see chapter 2). In CHO cells, ANDV mEGFP-Gc showed an average PML value of 0.77 upon singular expression and had a marked reduction of ≈30 % upon co-expression with unlabeled ANDV Gn in CHO cells. HTNV mEGFP-Gc showed an average PML value of 1.1 on singular expression and had a similar reduction of ≈30 % upon co-expression with unlabeled HTNV Gn. PUUV mEGFP-Gc, on the other hand, showed an average PML value of 1 upon singular expression and did not depreciate significantly upon co-expression with unlabeled PUUV Gn (Figure 4.4 E). mEGFP-Gn, on the other hand showed no detectable fluorescence intensity at the GPMV in the presence or absence of unlabeled Gc for all the HV strains tested (for GPMVs on cells expressing ANDV mEGFP-Gn, see Figure B.8). Similar results were observed with cells expressing ANDV mEGFP-GPC. Congruent results were obtained with all HV construct combinations tested in Vero E6 and A549 cells (Figure B.9)

Altogether, mEGFP-Gc localized weakly in GPMVs on independent expression and upon co-expression with Gn, for all the HV strains and cell models tested.

4.2.5. FLUORESCENTLY LABELLED HV GPS DO NOT FORM LARGE SPIKE ASSEMBLIES IN GIANT PLASMA MEMBRANE VESICLES

Finally, the possibility of large spike GP assemblies in the GPMVs was assessed. The mutlimerization of HV Gc partitioned at GPMVs was analysed using sFCS. In chapter 3 it was shown that Gc multimers greater than dimers were detected only in the presence of Gn. This informs the presence of large GP assemblies and was used to examine large GP complexes in GPMVs. mEGFP-Gc multimerization in GPMVs in the presence and absence of unlabeled Gn (encoded in the BD expression system) for the ANDV, HTNV and PUUV strains was respectively analyzed in CHO cells using sFCS (details, seechapter 1 for theory and chapter 2 for the implementation). mEGFP-Gc formed monomers and dimers in GPMVs on singular expression. Interestingly, in the presence of Gn, Gc multimerization in GPMVs continued to remain as monomers and dimers (Figure 4.5), indicating the lack of large GP assemblies.

Overall, across all the HV strains tested, fluorescently labelled Gc formed monomers and dimers upon singular expression and in the presence of unlabelled Gn in GPMVs. The latter finding suggests the absence of large GP spike assemblies in GPMVs.

4.3. DISCUSSION

Initial observations of virus budding at the PM of North American HV strains resulted in the hypothesis that virus assembly at the PM is a distinguishing feature between OWHVs and NWHVs [97] [98]. In subsequent years, similar results were noted with OWHV strains such as HTNV [102] and PUUV [65] [117]. In this chapter, PM localization of GPs was evaluated by a systematic comparison between OWHV and NWHV strains using multiple *in vitro* assays.

Non-fluorescent ANDV and PUUV GPs were substantially detected at the PM upon co-expression, for all the cell models tested. Punctuate ANDV GPs structures were observed at the cell surface. This is congruent to the results previously obtained with SNV [94] and HTNV [102] GPs in Vero E6 cells. ANDV GPs upon expression, from either from a single GPC or from separate cDNAs, were also detected at the PM. Interestingly, non-punctuate continuous localization was observed at the PM for PUUV GPs, upon expression from seperate cDNAs.

Non-fluorescent ANDV GPs were also discerned at the PM on singular expression, for all cell models tested. While PUUV Gc upon individual expression showed partition at the PM, singular expression of PUUV Gn did not yield any detectable localization at the cell surface. The latter observation could be due to the limited PUUV Gn expression (below the detection limit of the IF assay) at the cell surface. Based on these inferences, HV GPs partition at the PM without the requirement of GP co-expression. This is contrary to the previous observations with SNV [94] and HTNV GPs [102].

Singular expression of GPs of other Bunyavirus strains such as Punta Toro phlebovirus (Gc) [118] and Rift Valley Fever Virus (RVFV) (Gn) [119], have also showed distinct partition at the PM. In phleboviruses, the short length of Gc-CT, akin to HV Gc-CT, was proposed to modulate PM expression [120]. While Gc peptide domains [100] and N-glycosylation site [103] have been attributed for cell-cell fusion in the presence of HV Gn, specific GP motifs that regulate cell sur-

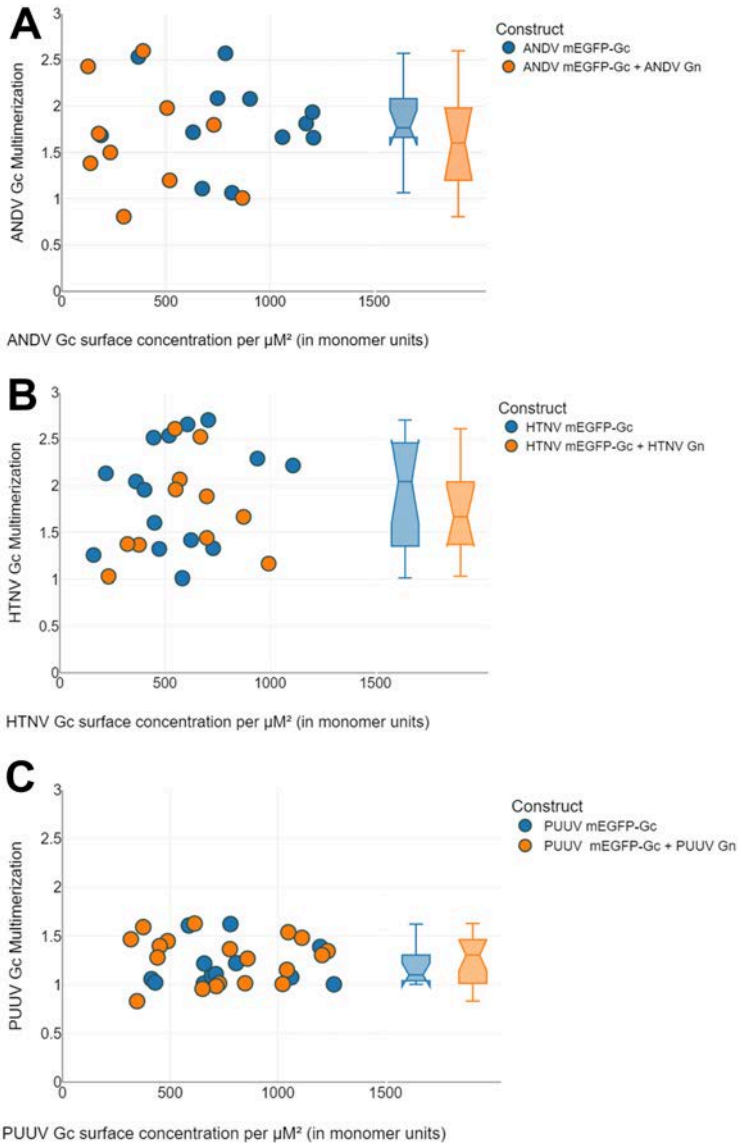

Figure 4.5: **ANDV, HTNV and PUUV Gc do not form large spike assemblies in GPMVs:** Gc multimerization within GPMVs was quantified using sFCS. Protein multimerization plotted as a function of local surface concentration (in monomer units) and each point represents one cell. Minimum of 10 individual cells were considered for each construct combination. The right insert shows the multimerization data points grouped per category in the form of notched box plots. [A] Multimerization of ANDV mEGFP-Gc when expressed alone or concurrently with ANDV Gn BD mCh2. [B] Multimerization of HTNV mEGFP-Gc when expressed alone or concurrently with HTNV Gn BD mCh2. [C] Multimerization of PUUV mEGFP-Gc when expressed alone or concurrently with PUUV Gn BD mCh2. Calculation of surface concentration (in monomer units), refer to Equation 2.9.

face localization upon individual expression have not been identified yet. Future assessments are required for identifying such peptide domains on HV GPs.

Unfortunately, the nature of structures (punctuate/filamentous/another formation) HV GPs form at the PM cannot be concluded from experiments performed in this chapter. SNV GPs [94] and HTNV GPs [102] were shown to form punctuate aggregates in Vero E6 cells. On the contrary, in the VSV expression system, HTNV GPs formed dendriform or branch-like projections at the cell surface [104]. Similar results were seen with orthobunyavirus GPs in a non VSV system [121]. In SNV [94] and BCCV [98] infected Vero E6 cells, GPs were detected as continuous granular punctuates at the cell surface. Experiments in this chapter with ANDV GPs and PUUV GPs showed different GP localization structures. Thus, further investigation is required to assess what HV GPs structures are formed at the PM and the factors that regulate them. This is relevant in elucidating the GP assembly at the PM.

Expression of fluorescently labelled ANDV GPs did not result in distinct partition at the PM, even at later time points of transfection. Within the observed concentration range, ANDV mEGFP-GPC and ANDV GPC-mEGFP resulted in large GP assemblies (Gn ca. upto decamers and Gc ca. upto tetramers) at the perinuclear region (mainly at the GA) 24 hpt. Distinct PM localization of Gn and Gc was not observed for ANDV mEGFP-GPC and ANDV GPC-mEGFP, even 120 hpt (day 5). This was contrary to the observation with SNV infected cells (on day 5 distinct localization of GPs at the PM was observed in infected cells) [94]. Based on these findings and the results from chapter 3 with PUUV GPs, HV GPs form large GP assemblies at the GA.

Fluorescently labelled HV Gc localized weakly (even in the presence of HV Gn) in GPMVs, a model membrane system that is devoid of cytoskeletal factors. Weak Gc localization was confirmed by the low PML values (< 1.5), for all the HV strains and cell models evaluated. Interestingly, ANDV GPC-mEGFP did not localize in the GPMVs. This can be credited to the steric hindrance caused by the FP tagging at C-terminus of Gc because HV Gc constructs with GFP fused at the N terminus of Gc had distinct localization in the GPMVs. On the contrary, mEGFP-Gn had no detectable expression in GPMVs, in the presence and absence of Gc.

sFCS experiments further showed that large GP spike assembly did not occur in GPMVs due to the lack of Gc multimers greater than dimers in the presence of untagged Gn. This result also advocates that Gn might not reside in GPMVs (Gc forms multimers greater than dimers only in the presence of Gn, as seen in chapter 3), similar to the PML results with HV mEGFP-Gn. The limited HV Gn partition in GPMVs might be due to (a) longer Gn-CT domain that might inhibit the transport of Gn into GPMVs or (b) Gn interaction with cytoskeletal factors that are absent in GPMVs. The former is less likely since PUUV Gn truncated at its CT domain did not yield a distinct PM localization (Figure C.6 A).

While HV GPs have not been reported to associate with cytoskeletal factors, the results with other Bunyavirus strains indicate otherwise. RVFV Gn has been proposed to interact with vimentin. The di-lysine motif of Gc-CT, which is similarly conserved in all HV Gc-CTs, has been attributed for a possible role in cytoskeletal remodelling of the cell [122]. It has been known that cytoskeletal factors like actin (for NWHV) and microtubules (for OWHV) play a crucial role

in the progression of HV trafficking and replication [123]. These previous results indicate that the influence of cytoskeletal factors on HV GPs cannot be discounted. Further work is necessary to assess the influence cytoskeletal factors on HV GPs for proper trafficking, assembly and budding of particles, similar to the hypothesis presented with RVFV GPs.

4.4. CONCLUSION

The PM localization of GPs between OWHV and NWHV strains was investigated in a systematic 1:1 comparison to show that HV GPs partitioned at the PM for all the strains and cell models tested. Non-fluorescent HV GPs localized at the PM without the requirement of GP co-expression. HV GP expression at the cell surface was detected when the GPs were expressed from a single GPC or separate cDNAs. The findings further highlighted that fluorescently labelled HV Gc was trafficked to the PM in the presence and absence of HV Gn in GPMVs. Additionally, large scale GP assemblies were not detected in the GPMVs, since the multimeric state of HV Gc detected in the presence of HV Gn continued to remain monomers and dimers.

5

Quantitative Sub-Cellular Interactions between Puumala HV Nucleocapsid Protein and Glycoproteins

5.1. Motivation

Negative sense RNA enveloped viruses generally encode a matrix protein. It performs important functions ranging from membrane budding to coordinating viral components for transcription [124]. Bunyaviruses lack this matrix protein that mediates the interactions between the RNP complex and the GP spike. GP-CT domains, particularly that of Gn, is proposed to act as a surrogate matrix protein [125]. RNP-GP interactions via GP-CT domains was hypothesized to control the development of the viral assembly by bringing pre-assembled GP spikes into close proximity, eventually leading to the formation of the intact virion [39]. However, there is limited mechanistic information on how the different components of the RNP complex (NP, RdRP and viral RNA) interact with the GP spike to generate the HV virion. This chapter primarily focuses on the NP-GP interactions and its role in the viral assembly.

Multiple features of NP-GP interactions in the viral assembly have been characterized previously [138] [139]. Gn-CT and Gc-CT interacts with the NP (being part of the RNP complex) [43] and with purified recombinant NP [126]. Shimizu et al. [127] demonstrated that co-expression of HTNV GPC with HTNV NP promoted the localization of Gc at the GA. They also concluded that deletion of 6 amino acids at the carboxyl terminal of HTNV Gc-CT lowered the HTNV NP expression upon co-expression with HTNV Gc. This finding led to the proposition that NP stabilizes the GP spike heterocomplex through NP-Gc interaction via Gc-CT. Acuña et al. [128] showed with ANDV and PUUV strains, that VLPs are formed upon singular expression of GPC, similar to phleboviruses [122] and concluded that NP is not essential for VLP formation.

While previous studies have provided insights into how NP interacts with the GP spike, there has been a lack of quantitative information on the role of NP-GP interactions in the overall viral assembly. Thus, the NP-GP interactions were analysed using the PUUV strain by evaluating the following aspects:

1. What is the magnitude of interactions between NP and GP ?

2. How does NP-GP interactions increase the average multimerization of GP and NP ?

These inquiries were examined in the context of NP not being associated with the RNP complex, allowing the further realization of the relevance of the RNP complex in NP-GP interactions. These interactions are generally difficult to characterize within an infection context and the strategies presented in this chapter provide an alternative methodology to examine such interactions in detail.

In this chapter, NP-GP interactions and its role in the virion development was analysed in multiple cell models. Initially, homotypic NP-NP interactions were examined in relevant human and rodent epithelial cell models. This was followed by evaluating the possible increase of NP and GP multimerization upon co-expression. Further assessments were conducted to study the strength of NP-GP associations in living cells and to observe the distribution of interactions within single cells. The GP-CTs, the interacting domains between NP and GP, were truncated to understand their influence on NP-GP associations. And finally, the variations of GP multimerization, as a function of absolute brightness, upon co-expression of NP, Gn and Gc, was discerned.

Certain findings of this chapter have already been published under the title "*Characterization of Hantavirus N Protein Intracellular Dynamics and Localization*" in Viruses journal [66]. The co-localization experiments performed independently by my collaborators in this article was used in justifying the design of new experiments performed for this work and will referenced as *Previous work by collaborators*.

Additionally, the constructs used in this chapter are primarily fluorescently labelled and are from the PUUV strain. Any non-fluorescent labelled constructs and other HV strains will be appropriately highlighted. Appropriateness of the cell models (CHO, HEK, BHK-21 and A549) used in this chapter have been discussed earlier in chapter 2. Additional results pertaining to this chapter are shown in Appendix C.

5.2. Results

5.2.1. Homotypic NP-NP interactions are more significant in human epithelial cell models compared to rodent epithelial cells

NP multimerization analysis was performed in human epithelial cell models of HEK 293T and A549 and compared to the results obtained from rodent CHO and BHK-21 cells. The analysis was completed using N&B. Cells expressing NP primarily as granular multimers in the cytosol were chosen for the multimerization analysis. CHO (Figure 5.1 A), BHK-21 (Figure 5.1 B), A549 (Figure 5.1 C) and HEK (Fig 5.1 D) cells transfected with YFP-NP were examined 20-24 hpt. The

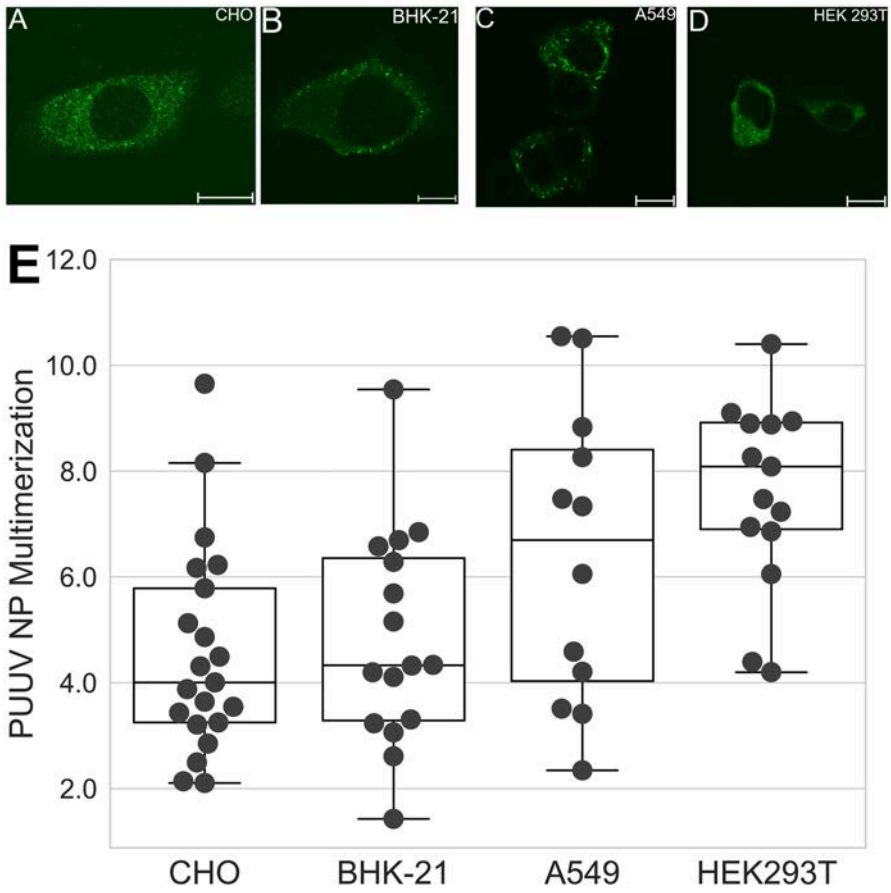

Figure 5.1: **Comparison of NP multimerization in epithelial cell models**: Representative image of [A] CHO, [B] BHK-21 [C] A549 and [D] HEK 293T cell expressing YFP-NP as granular multimers in the cytosol primarily. [E] Boxplot with multimerization values of NP between living cell models. Multimerization values were obtained within the concentration range of 0.2 to 0.7μM for the purposes of 1:1 comparison between different cell models. Each point in the graph represents the average multimerization in one cell. Minimum of 10 cells were considered for each cell model. Scale bars are 10 µm.

concentration range of 0.2 to 0.7μM was selected to afford a 1:1 comparison of NP multimerization between different cell models. Within this concentration range, NP formed an average ca. hexamers and octamers in A549 cells and HEK cells respectively compared to the average ca. NP tetramers observed with CHO and BHK-21 cells (Fig 5.1 E).

Thus, independent of the cell model, NP formed larger multimers of varying size (up to ca. decamers) before transitioning to the filamentous and cluster aggregates. Stronger NP-NP interactions were observed in HEK and A549 cells compared to rodent CHO and BHK-21 epithelial cells

5.2.2. Multimerization of PUUV Gc increases upon co-expression of PUUV NP

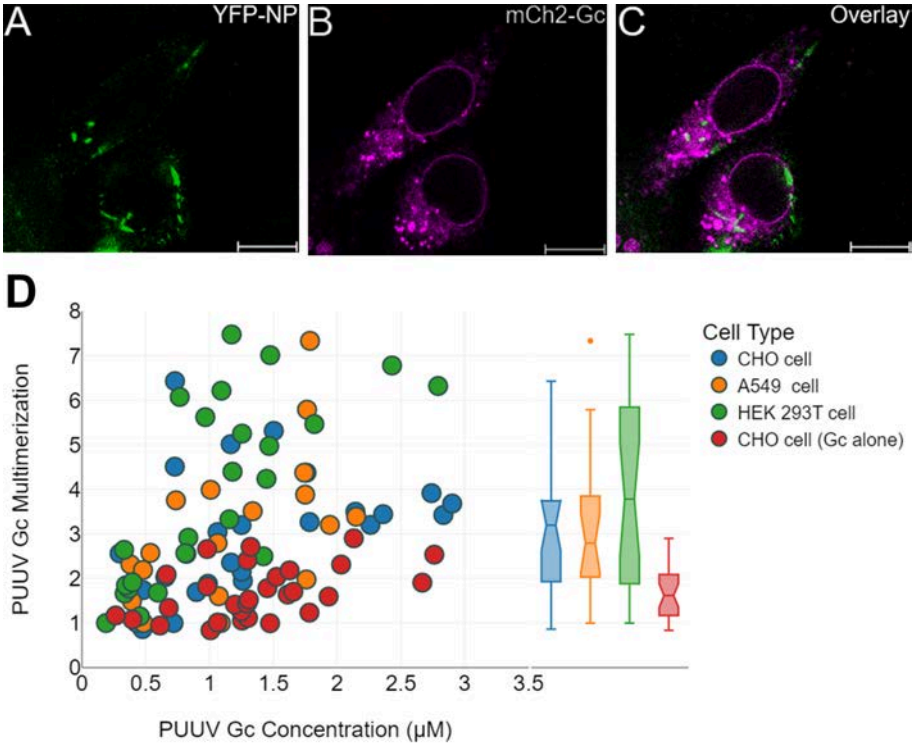

Figure 5.2: **Gc multimerization increases in the presence of NP**: [A] to [C] Representative images of CHO cells co-expressing YFP-NP and mCh2-Gc 24 hpt. [D] Concentration dependent multimerization analysis of PUUV Gc in the presence of PUUV NP in rodent and human cell lines, completed with N&B. CHO (blue), A549 (orange) and HEK cell lines (green). Each point in the graph represents the average multimerization in one cell. Gc multimerization upon co-expression with NP is further compared with Gc multimerization on individual expression in CHO cells (red). Each point in the graph represents the average multimerization in one cell. Right panel insert shows the multimerization data points grouped per category in the form of notched box plots. Minimum of 15 cells were considered for each cell model. Scale bars are 10 μm.

Multimerization of NP and GPs upon co-expression was analysed. NP formed large multimers in the presence of GPs (Gn/Gc), similar to its singular expression (Figure C.2). Next, Gc multimerization was assessed upon co-expression with NP in multiple epithelial cell models was evaluated. YFP-NP and mCh2-Gc were co-expressed in CHO (Figure 5.2 A-C), HEK (Figure C.3 A-C) and A549 cells (Figure C.3 D-F) and Gc multimerization was quantified using N&B. In the presence of NP, Gc formed multimers up to ca. octamers, for all the cell models tested.

Futhermore, Gn multimerization in the presence of NP was examined using N&B. YFP-NP and mCh2-Gn were co-expressed in CHO (Figure 5.3 A-C), HEK (Figure C.4 A-C) and A549 cells (Figure C.4 D-F). In the presence of NP, Gn continued to form up to tetramers, for all the cell

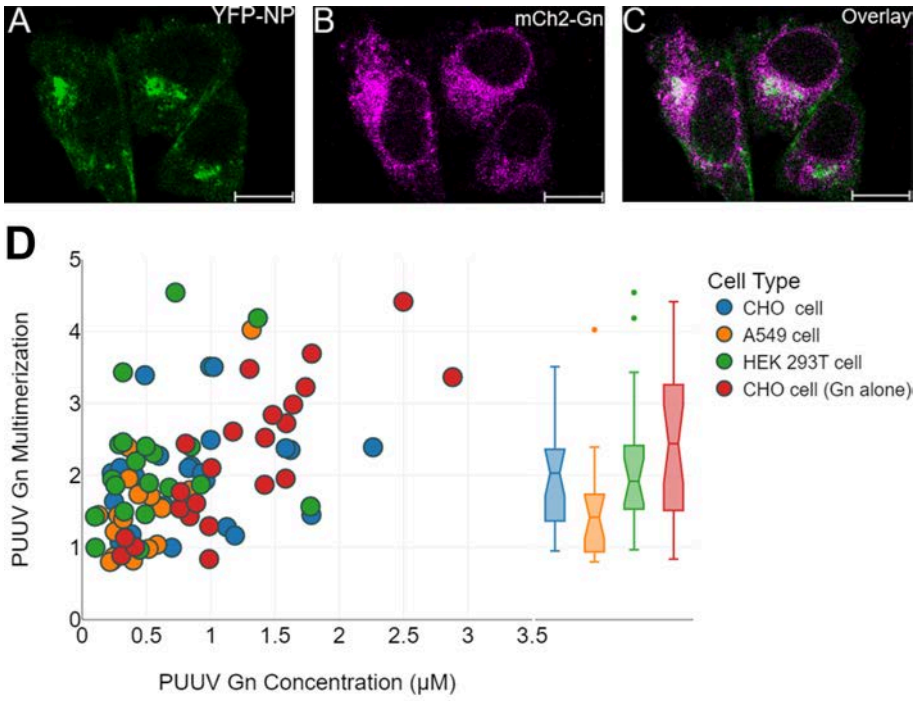

Figure 5.3: **Monomer-tetramer equilibrium of Gn is not affected by the presence of NP**: [A] to [C] Representative images of CHO cells co-expressing PUUV YFP-NP and PUUV mCh2-Gn 24 hpt. [D] Concentration dependent multimerization analysis of Gn in the presence of NP in rodent and human cell lines, completed with N&B. CHO (blue), A549 (orange) and HEK cell lines (green). Gn multimerization upon co-expression with NP is further compared with Gn multimerization on individual expression in CHO cells (red). Each point in the graph represents the average multimerization in one cell. Minimum of 15 cells were considered for each cell model. Right panel insert shows the multimerization data points grouped per category in the form of notched box plots. Scale bars are 10 μm.

models tested. Gn multimers greater than tetramers were not detected in the presence of NP within the observed concentration range. Thus, NP did not result in an increase of Gn multimerization.

Thus, independent of the cell model, Gc formed large multimers in the presence of NP, while Gn continued to exist within the monomer to tetramer equilibrium in the presence of NP.

5.2.3. PUUV GC ASSOCIATES WITH PUUV NP VIA GC-CT TO FORM LARGE MULTIMERS

The influence of Gc-CT on NP-GP interactions was further examined. Truncated Gc without the CT domain (GcΔCT) was generated. mEGFP-GcΔCT was initially expressed individually in CHO cells and formed monomers within the concentration range observed, 24 hpt (Figure 5.4 B). This result was in agreement with the size exclusion chromatography results by Willensky et al [129]. Upon co-expression with YFP-NP in CHO cells, GcΔCT continued to remain monomeric primarily (Figure 5.4 B). Similar results were obtained also in A549 cells (Figure C.7).

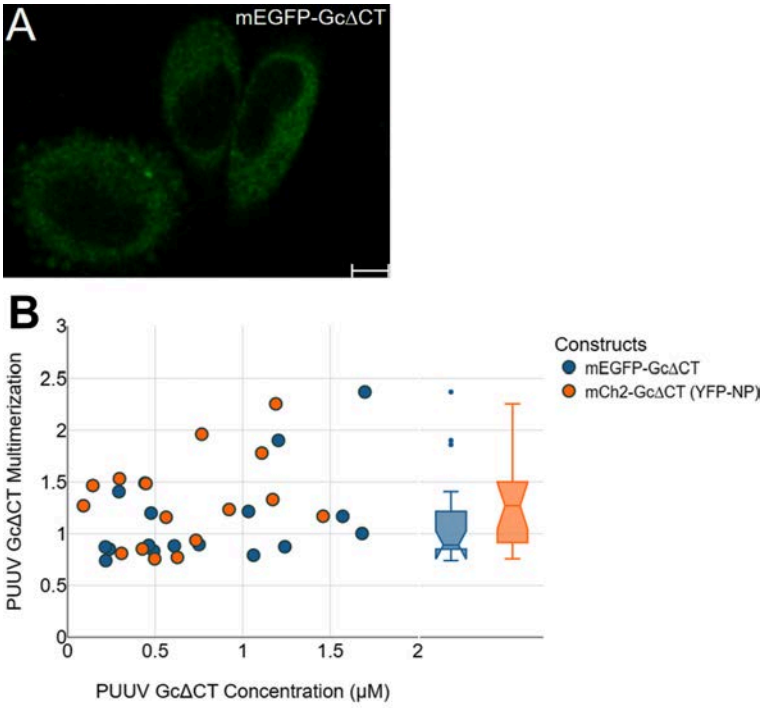

Figure 5.4: **Multimerization of GcΔCT is not influenced by the presence of NP**: mEGFP-GcΔCT was expressed in the presence and absence of YFP-NP in CHO cells 24 hpt. [A] Representative images of CHO cells expressing mEGFP-GcΔCT observed 24 hpt. [B] Concentration dependent multimerization analysis of GcΔCT in the absence (blue) and presence (orange) of NP 24 hpt, using N&B. Each point in the graph represents the average multimerization in one cell. Minimum of 10 cells were considered for each cell model. The right panel insert shows the multimerization data points grouped per category in the form of notched box plots. Scale bars are 10 μm

GnΔCT also formed monomers primarily in the presence and absence of NP (Figure C.6). The latter is similar to the results obtained by the size-exclusion chromatography experiments by Liu et al. [31] and confirms the observation that Gn-CT is crucial for Gn oligomerization [94].

Thus, increase in Gc multimerization upon co-expression of NP is facilitated by NP-Gc interaction via the Gc-CT domain.

5.2.4. PUUV NP AND PUUV GC HAVE LOCALIZED REGIONS OF HIGH INTERACTIONS IN LIVING CELLS

Finally, the NP-GP interactions were quantified upon co-expression in living cells. Significant co-localization was discerned between NP and GP(Gn/Gc) upon co-expression of fluorescently labelled NP, Gn and Gc. However, the co-localization between NP & GP (Gn/Gc) was significantly lower compared to Gn & Gc co-localization (*Previous work by Collaborators*). Co-localization of proteins only suggests the presence of protein species within the same spatial region and does

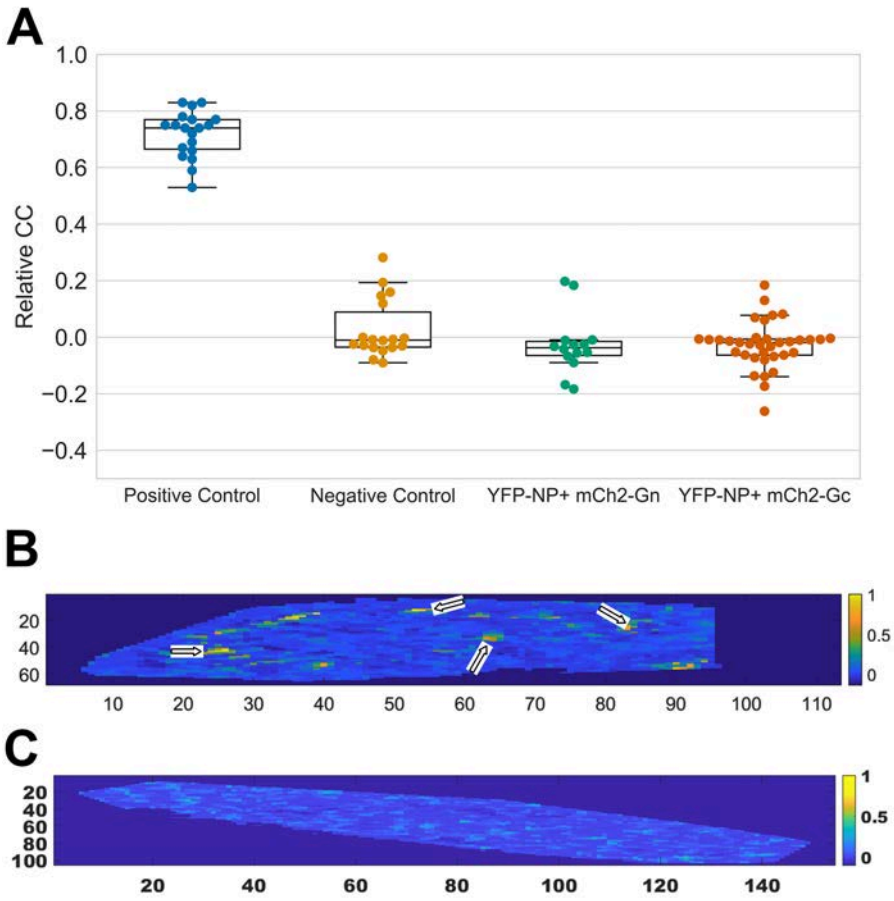

Figure 5.5: **Presence of localized regions of high NP-Gc interactions in CHO cells** [A] Relative CC values obtained from CHO cells co-expressing NP and GP(Gn/Gc) using ccN&B. Positive control is the tandem cytosolic construct (YFP-mCh2) and the negative control, is the co-expression of YFP-NP and cytosolic mCherry2. Each point on the graph represents a single cell. Minimum of 15 cells were considered for each cell model. The Relative CC values calculated here is the pixel average of the ROI selected in each cell (details of ROI selection, see Petrich et al.[59]). [B] Relative CC map for the CHO cell co-expressing YFP-NP and mCh2-Gc. The white arrows indicate the localized regions of high interaction. [C] Relative CC map for the CHO cell co-expressing YFP-NP and mCh2-Gn

not provide any information on the strength of interaction between the proteins. The covariance based ccN&B method was thus applied to evaluate NP-GP (Gn/Gc) associations (see chapter 1, for the theory and chapter 2 for the implementation protocol)

CHO cells co-expressing mCh2-GP (where GP=Gn/Gc) with granular punctuate multimers of YFP-NP were analyzed 24 hpt (Figure 5.5 A). Relative CC (parameter denoting average interaction) values for NP and GP(Gn/Gc) associations were similar to the values obtained for the

negative control. Similar results were obtained in HEK293T and A549 cells (Figure C.8).

Pixel-by-pixel maps of the Relative CC values were assessed to observed the Relative CC distribution within cells co-expressing NP and GP(Gn/Gc). Cells expressing the tandem YFP-mCh2 construct (positive control) have homogeneously distributed positive Relative CC values with high magnitude distributed throughout the cell (Figure C.9 B). In contrast, cells expressing YFP-NP and cytosolic mCherry2 (negative control) resulted in homogeneous low Relative CC values throughout the cell (Figure C.9 D). Similar to the negative control, low Relative CC values are observed for CHO cells expressing Gn and NP (Figure 5.5 C). On the other hand, localized intracellular regions characterized by high Relative CC (high abundance of Gc-NP complexes) was obtained in cells co-expressing Gc and NP (Figure 5.5 B). Such regions were primarily observed around the peri-nuclear region.

Thus, average NP-GP interactions in the cell are relatively weak. In cells co-expressing NP and Gc, spatially confined cellular regions characterized by significant NP-Gc interactions was observed.

5.3. DISCUSSION

RNP-GP interactions are crucial for driving the virion formation. The RNP comprises of NP, RdRp and viral RNA and it is essential to distinguish their individual interactions with GP and assess their respective consequences on the overall viral assembly. This chapter focused on quantifying the role of NP-GP interactions during the virion development. Despite the average NP-GP interactions in cells being relatively weak, localized regions of high interactions were detected in cells expressing NP and Gc.

NP-NP interactions were significantly higher in the human epithelial cells (HEK293T and A549) compared to their rodent cell models (CHO and BHK-21). This was substantiated by the higher average NP multimerization detected in HEK293T and A549 cells compared to CHO and BHK-21 cells at the same hpt, within the restricted concentration range of 0.2 to 0.7 μM. NP formed ca. between octamers and decamers before transitioning to filaments and aggregates. NP continued to form large aggregates in the presence of GPs, indicating that NP multimerization is not hindered by the presence of other HV proteins. Interestingly, over-expression of NP-mEYFP and mEGFP-NP resulted in artificial NP distribution in cells (Figure C.1). This suggests a probable influence of fluorescence tagging on NP localization.

NP multimerization presented in this work considered cells expressing NP primarily as granular punctuate multimers in the cytosol. However, understanding the concentration regime where NP exists as filaments and aggregates is relevant in deciphering the overall NP dynamics. Advanced microscopy techniques like Fluorescence Intensity Fluctuation (FIF) spectrometry [130] could be adapted to visualize and quantify the attributes of NP aggregates. Also, variations in the percentage of filamentous and aggregate PUUV NP structures could exist between different cell models, as proposed by Haegle et al.(2019) [131], an aspect unexplored in this work. Nevertheless, the methodologies presented in this work allowed for the assessment of NP dynamics, when it remains as granular multimers in living cells, for the very first time.

Large Gc oligomers (greater than dimers) were detected in the presence of NP. This result was complimented by the detection of localized regions of high NP-Gc interaction within cells despite the overall low average Relative CC value for the entire cell. Upon co-expression with mTurq2-NP and YFP-Gn in HEK cells, the average brightness of mCh2-Gc did not increment substantially compared to the co-expression of mEYFP-Gn and mCh2-Gc (absolute brightness $\propto$ protein multimerization, details see Equation 2.4 in chapter 2) (Figure C.5). Experiments in this work could not suggest the reason behind the similar brightness in both cases, since the Gn-Gc and Gc-NP interactions could not be decoupled appropriately.

NP-Gc interactions were limited upon truncating Gc-CT, since GcΔCT continued to exist primarily as monomers in the presence of NP. Two possible explanations can describe this finding (i) Sperber et al. [65] showed that the impaired stability of GcΔCT acerbated the likelihood of folding defects and premature degradation of Gc. This phenomenon could impact how GcΔCT interacts with NP or (ii) Hepojoki et al. [43] demonstrated that NP interacts strongly with the Gc-CT using SPOT peptide assay. Therefore, truncation of the CT segment would result in reduced association. The experiments performed in this chapter could not clarify if either mechanism is responsible for the findings with GcΔCT. Finally, the results with NP-Gc interactions is in contrast to the hypothesis of Hepojoki et al. [23] which suggested the interaction of Gn-CT with the RdRp-RNP complex being necessary for the association of Gc to the RNP-GP complex.

Gn continued to remain from monomers to tetramers in the presence of NP, for all the cell models tested. Weak NP-GP interaction was substantiated by the distribution of low Relative CC values (the factor for interactions in this study) within cells. Upon co-expression with NP and Gc, Gn showed no appreciable change in multimerization (measured as a function of absolute brightness, details see Equation 2.4 chapter 2) compared to the cells co-expressing Gn and Gc. These results support the hypothesis of Hepojoki et al. [23] which states that GP spike formation (which has Gn multimers $\geq$ tetramers) is essential for Gn-CT to interact with the RNP complex. Whether Gn interacts significantly NP upon forming larger Gn oligomers ($\geq$ tetramers) or whether NP is required to exist within the RNP complex to effectively interact with Gn-CT, is a consideration for future research.

NP-GP interactions using fluorescently labelled constructs was previously completed with Tomato spotted wilt virus (TSWV), a plant Bunyavirus using FRET-FLIM (Förster resonance energy transfer using Fluorescence-lifetime imaging microscopy) [134][135]. Expression of TSWV Gc-YFP with non-fluorescent TSWV N, resulted in Gc co-localization with N in specific clusters and increased expression level of Gc by 10 fold. The latter was attributed to the strong NP-Gc interaction, which was similarly observed by Shimizu et al. [127] on co-expressing HTNV NP and HTNV GPC. These findings are in line with the co-expression experiments presented in this work, where Gc multimerization increased in the presence of NP. Overall, based on the inferences in this chapter and the previous results with TSWV and HTNV, NP-Gc interactions could play a pivotal role in the overall virus assembly, not only for HVs, but bunyaviruses in general.

5.4. CONCLUSION

This chapter focused on the quantification of NP-GP interactions and the impact of GP oligomerization in the presence of NP in living cells. In the presence of NP, Gn continued to remain from

monomers to tetramers, while Gc formed upto ca. octamers in all the cell models tested. The latter finding was complimented by localized regions of high NP-Gc interactions. The average NP-GP interactions are weak in cells expressing NP as granular punctuate multimers. Finally, homotypic NP:NP interactions were stronger in human epithelial cells compared to rodent epithelial cells. This variation did not influence the NP-GP interactions in different cell models.

6

CONCLUDING REMARKS AND FUTURE PROSPECTS

6.1. KEY CONCLUSIONS FROM THE THESIS

Understanding the molecular mechanisms that regulate the HV pathogenesis is essential in developing appropriate antivirals and vaccines against this debilitating pathogen. In this regard, analysing the interactions of HV proteins responsible for HV virion formation is crucial. This research work focused on elucidating the initial steps of the HV virion development in living cells, primarily involving GPs and NP, and the following conclusions were obtained:

1. **Quantitative evidence for the mechanism of GP spike formation**: This work finally proves which model [43] describes the GP spike formation in cells appropriately, nearly a decade after its proposition. It was clearly demonstrated that Gn and Gc initially forms a heterodimeric Gn:Gc subunit, which further multimerizes to form the final $(Gn\text{-}Gc)_4$ spike complex (further details, see chapter 3)

2. **HV GPs partition at GA and at PM**: The results from chapter 3 and chapter 4 evidently demonstrates that HV GPs partition both at the GA and at the PM, irrespective of the strain evaluated. This is contrary to the existing proposition which states that HV GPs generally localize and assemble within the ER-GA network [134]. The work also shows that large scale GP complexes preferentially form at the GA and that GPs localizes weakly at the PM, across different strains (further details, see chapter 4).

3. **Gc multimerization increases due to NP-Gc interaction via Gc-CT**: The results from chapter 5 highlights the influence of NP on Gc multimerization (NP being present primarily as granular multimers in the cytosol). This was concurred by the presence of localized regions of high NP-Gc interactions in cells. Additionally, outside the RNP complex, average NP-GP interactions in the cell remained relatively weak.

6.2. FUTURE PROSPECTS

6.2.1. CELLULAR LOCALIZATION OF HANTAVIRUS GLYCOPROTEINS

The experiments performed in chapter 3 and chapter 4 demonstrated several key characteristics of HV GPs partitioning at the GA and at the PM in multiple HV strains and cell models. This brought forth additional open questions regarding HV GP localization in cells, which includes:

1. **What is the mechanistic model for GP intra-spike (GP interactions necessary to form the final spike) and possible GP inter-spikes (interactions between GP spikes) formation at the PM, given both GPs localize at the PM independently ?**
   The experiments in this work clearly discern the presence of HV GPs at the PM. However, due to relatively low GP concentration at the PM (in comparison to GA), the dynamics of possible spike formation could not be appropriately assessed. It would be intriguing to verify if large spike GP assemblies can be formed at the PM for OWHV and NWHV strains, despite the weak localization (highlighted from PML results, see chapter 4).

2. **What intracellular transport processes regulate the partition of GPs at the GA and at the PM ?**
   This work highlights that GP localization is not exclusive to the ER-GA network. Intracellular transport processes can regulate the partition of GP in cells, particularly between GA and PM. Rowe et al. [135] showed how Rab11, a recycling endosome that operates between Trans Golgi Network (TGN) and PM, plays an important role in ANDV infection. Thus, it would be relevant to examine which host cellular proteins modulates the GP transport between the ER-GA network and the PM.

3. **Which cytoskeletal factors affect the localization of GPs at the PM and what is the mechanism behind such interactions ?**
   HV infections are shown to be influenced by cytoskeletal factors [123]. Interestingly, in GP-MVs, devoid of several cytoskeletal factors, preferential localization of Gc was detected. Thus, understanding whether cytoskeletal proteins influence GP localization and subsequent GP assembly at the PM would develop the mechanistic model presented in question 1 of this section

4. **Which peptide regions on Gn are essential for GP partition at the PM ? What consequences occur on overall GP localization if such regions are mutated ?**
   While several regions on Gc have been attributed for cell-cell fusion , no significant sequence on HV Gn has been attributed to dictate its partition at the PM. Such regions would permit us to understand how GPs interact at the PM. This assessment can be extended to assess such peptide domains influence the GP interaction with cytoskeletal factors.

These additional inquiries will expand the understanding of how HV GPs partition at the GA and PM. The *in vitro* strategies highlighted in this doctoral work can be adapted to address these open questions. The results from these queries coupled with the current findings from this work can then be suitably extrapolated to other relevant Bunyavirales strains such as pheloboviruses, whose GPs are also proposed to partition at the PM [122].

6.2.2. NUCLEOCAPSID PROTEIN-GLYCOPROTEINS INTERACTIONS

The *in vitro* approaches in this work have established several key quantitative features on NP-GP associations. The findings from this work have established additional questions on NP-GP interactions:

1. **Does Gn and NP interact significantly when Gn forms oligomers greater than tetramers ?**
   This would indicate the validity of the proposition of Hepojoki which states that Gn-CT interacts with NP after the formation of GP spike, where large Gn oligomers ($\geq$ tetramers) exists [43].

2. **Does the NP, Gn and Gc expression levels have a correlation over time in infected cells ?**
   This experiment would verify if concentration trends of GP in the presence of NP observed in transfected cells in this work are similarly noted in infected cells. It would also verify the influence of RNP complex formation on the expression levels of NP, Gn and Gc.

3. **Does the GP spike regulate the percentage of NP granular, filamentous and aggregate multimers over time compared to the individual expression of NP? Are there differences across different human and rodent cell models ?**

These additional queries coupled with the current results from this work will comprehensively build our understanding on NP-GP interactions. This would also precisely analyze the necessity of NP to form the RNP before it associates with the GP spike and permit us to determine the role of other viral proteins like RdRP and viral RNA in the virion assembly. The *in vitro* methodologies outlined in this research work can be incorporated to screen for these associations effectively.

Appendices

A

Hetero-Interactions of Hantavirus Glycoproteins essential for Spike Formation

Extended results from chapter 3 showing the raw data for the plots appearing in Figure 3.1 and Figure 3.2. Points used for the equal frequency binning in these respective figures are plotted.

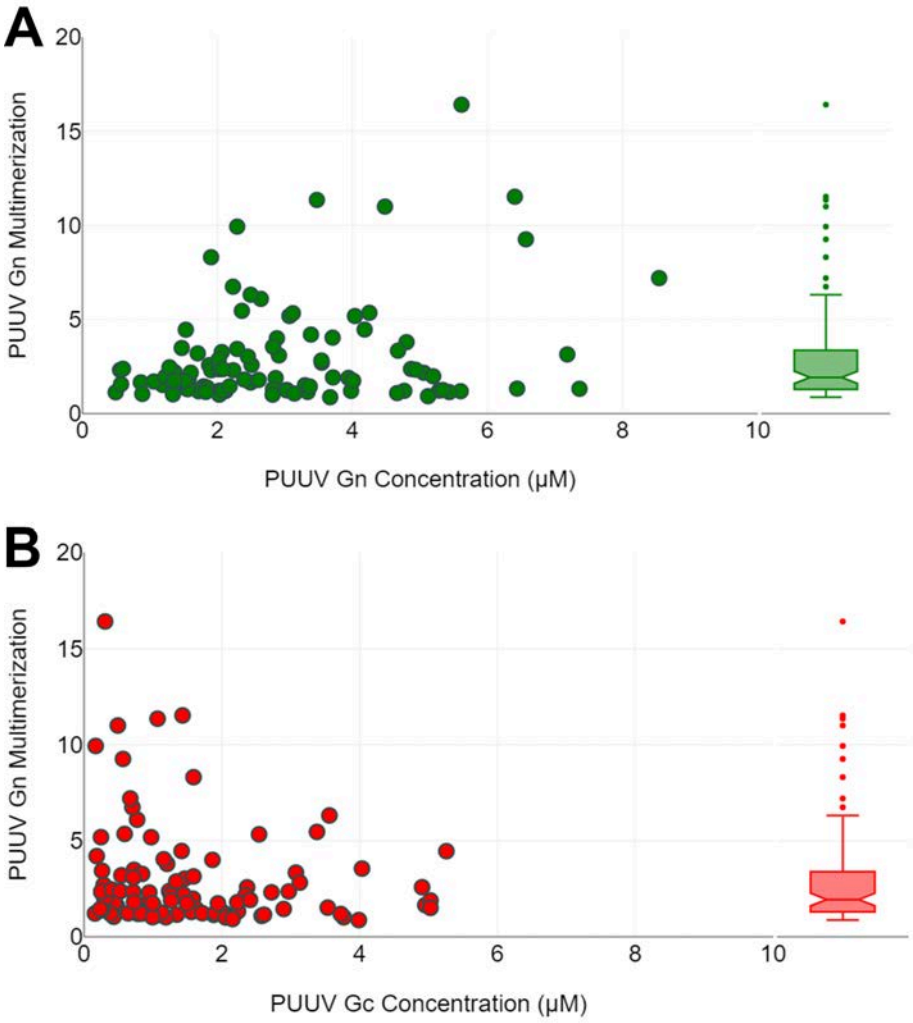

Figure A.1: **Concentration-dependent multimerization of PUUV Gn in the presence of PUUV Gc in CHO cells**: Raw data of PUUV mEGFP-Gn multimerization as a function of [A] PUUV mEGFP-Gn or [B] unlabelled PUUV Gc concentration. Raw data shown in [A] and [B] was binned suitably in Figure 3.1 E and 3.1 F respectively. Each sphere represents one cell (Total number of cells: 100 cells). Each data set was obtained from at least 4 separate experiments.

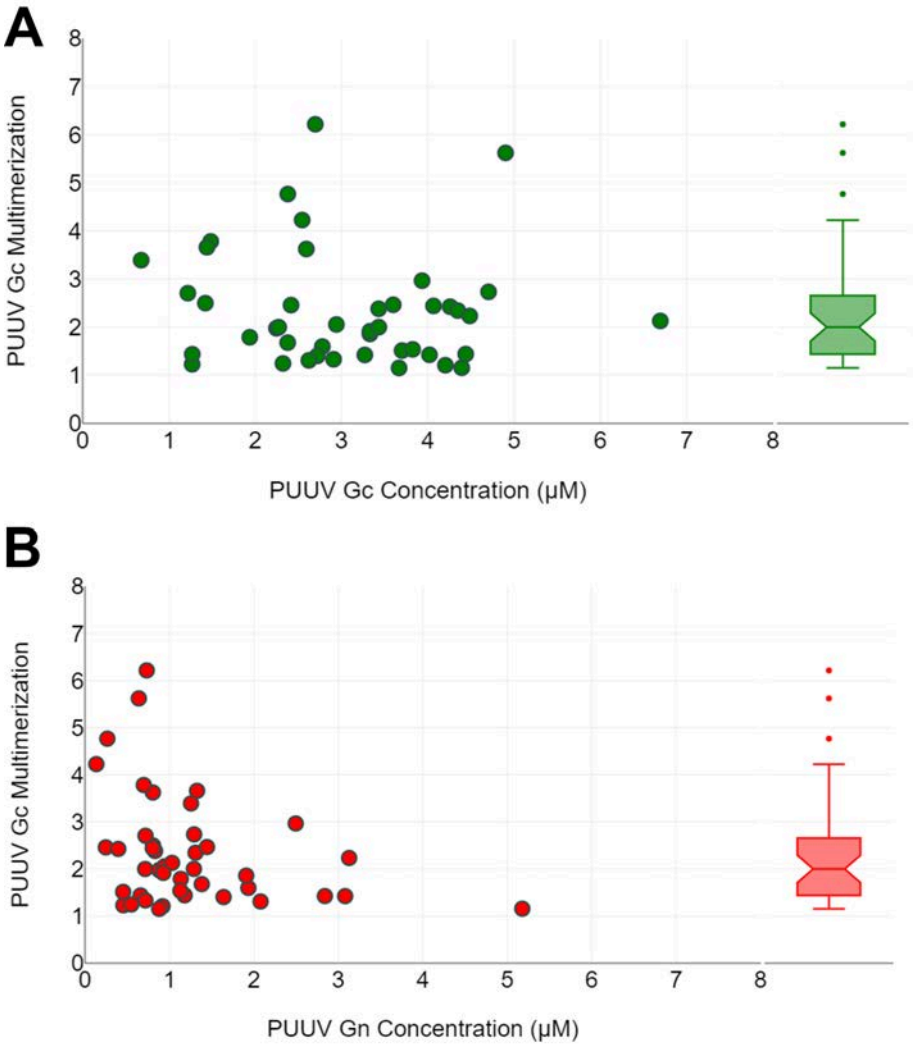

Figure A.2: **Concentration-dependent oligomerization of PUUV Gc in the presence of PUUV Gn in CHO cells**: Raw data of PUUV mEGFP-Gc multimerization as a function of [A] PUUV mEGFP-Gc (A) or [B] unlabelled PUUV Gn concentrations. Raw data shown in [A] and [B] was binned suitably in Figure 3.2 E and 3.2 F respectively. Each sphere represents one cell (Total number of cells: 43 cells). Each data set was obtained from at least 4 separate experiments.

B

Plasma Membrane Localization of Hantavirus Glycoproteins

B.1. Control experiments for the specificity of primary antibodies used in cell surface localization

Primary antibodies used for the detecting ANDV GPs in this study were not applied previously. Specificity of the Ab binding to the GPs was analysed by examining the intracellular localization of ANDV GPs upon expressing non fluorescent ANDV Strep-II GPC in CHO cells. Previous experiments with Vero E6 cells by Deyde et al. [95] have shown that GPs localizes around the perinuclear region in ANDV GPC transfected cells. This result was used in evaluating the Ab functionality (Figure B.1).

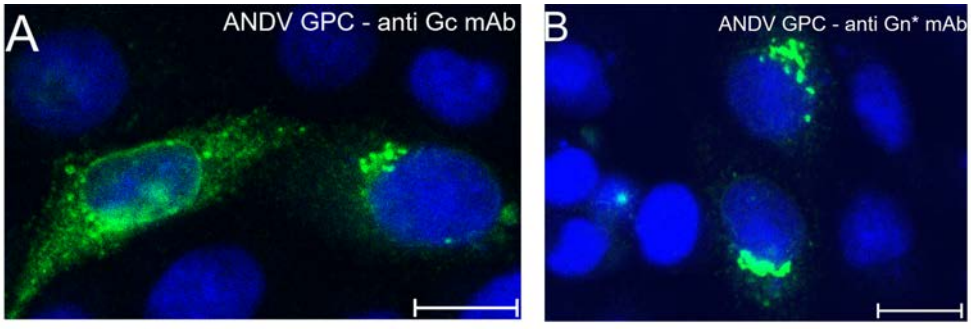

Figure B.1: **ANDV Gn and Gc localize at the perinuclear region upon expression of non-fluorescent ANDV GPC in CHO cells**: Representative images of total intracellular expression of ANDV Strep II-GPC in CHO cells. Cell nucleus is stained with the Hoescht dye (in blue). Total intracellular localization of [A] ANDV Gc and [B] ANDV Gn. Details on Abs used, see Table 2.5 (chapter 2) Scale bars are adjusted to 10 µm.

B.2. NON FLUORESCENT ANDV GPS LOCALIZES AT THE PM UPON CO-EXPRESSION FROM SEPERATE CDNAS

Figure B.2 shows that ANDV Gn and Gc localizes at the PM upon co-expression from separate cDNAs. Untagged ANDV Gc and ANDV Gn mCh2 BD were co-expressed to visualize the localization of Gc while ANDV Strep-II Gn and ANDV Gc BD mCh2 were co-transfected to observe the localization of ANDV Gn. This strategy of co-expression allows the selection of cells where both the GPs are co-localized.

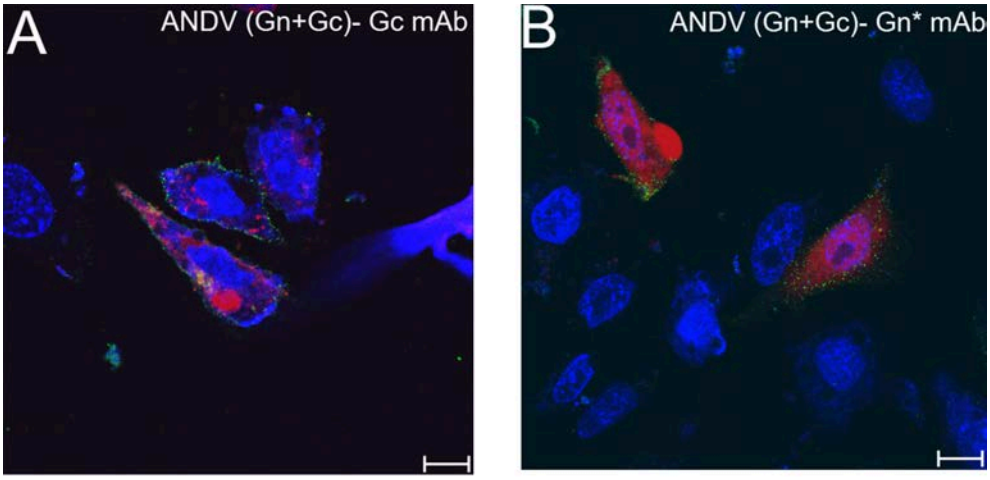

Figure B.2: **Cell surface expression of non fluorescent ANDV Gn and Gc upon co-expression from separate cDNAs in CHO cells**: [A] Representative image of expressing ANDV Gc and ANDV Gn BD mCh2 and observed 24 hpt. PM localization of ANDV Gc observed using an anti-Gc mAb (4G7/E10) and a Goat anti-Mouse 2^{nd} Ab. [B] Representative images of CHO cells expressing ANDV StrepII-Gn and ANDV Gc BD mCh2 expressed in CHO cells and observed 24 hpt visualized using an anti-Strep (Gn*) mAb and a Goat anti-Rabbit IgG secondary antibody. The nucleus was stained visualized via with Hoechst dye (purple).

B.3. CONTROL EXPERIMENTS FOR SPECIFICITY OF PM LOCALIZATION VISUALIZED WITH CELL SURFACE IF

Figure B.3 describes the control experiments that ensured the localization visualized using the cell surface IF was detected with proteins that partition at the PM. Initially, the localization of α-tubulin staining was examined with transfected (expressing ANDV Strep-II GPC) and non-transfected cells. Furthermore, the possibility of artifacts by the Abs was examined by treating it with transfected and non-transfected cells ((details, see chapter 2). All the negative controls performed in this regard, did not give any detectable expression as demonstrated in Figure B.3 (A-D).

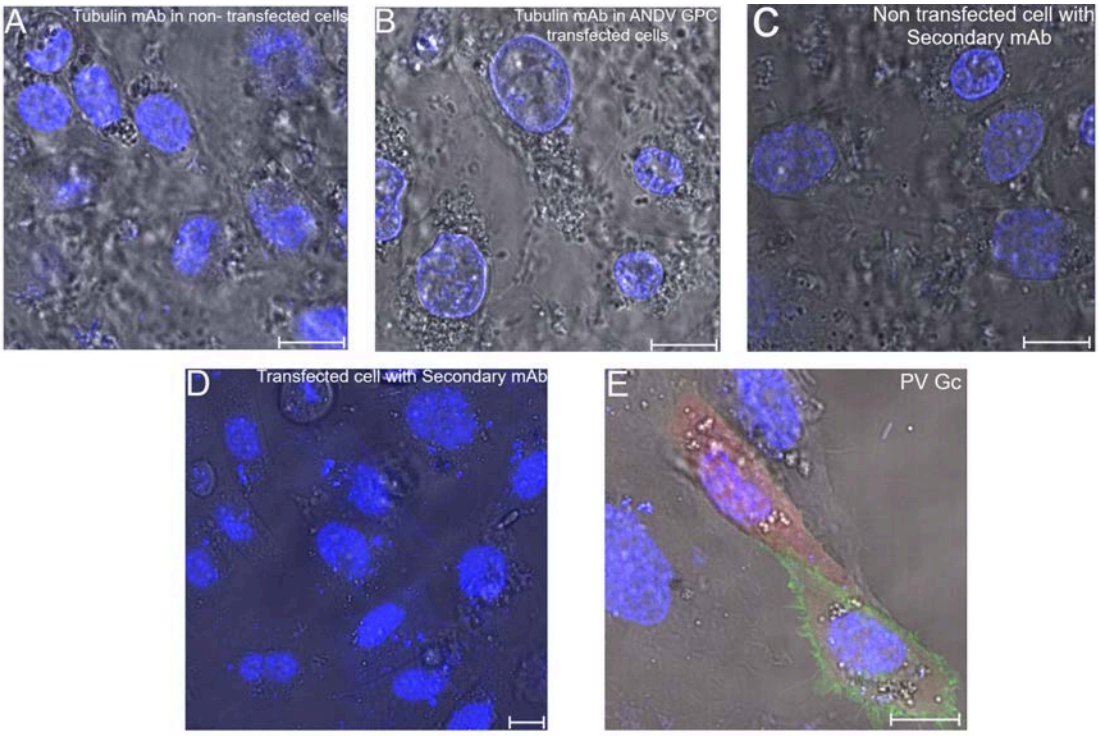

Figure B.3: **Negative controls for the cell surface IF experiments:** Transfected CHO cells in this image expresses ANDV Strep II-GPC and are observed 24 hpt. Transmission image shows the cell surface and the Hoescht dye (blue) stains the cell nucleus. Representative images of [A] non transfected and [B] transfected CHO cells treated with anti-tubulin Ab and Goat-anti mouse 2^{nd} Ab. [C] Representative image of non-transfected CHO cells treated with the primary Ab (anti-Strep mAb) and 2^{nd} Ab (Goat anti-mouse 2^{nd} Ab). [D] ANDV Strep-II GPC transfected CHO cells treated with secondary Ab (Goat anti-mouse 2^{nd} Ab).[E] Cell expressing PUUV Gc mCh2 BD. This reference cell surface localization is presented to compare the images [A] to [D], where no detectable partition at the PM is observed. Further details see chapter 2. Scale bars are adjusted to 10 µm.

B.4. ADDITIONAL RESULTS OF NON-FLUORESCENT AND FLUORESCENT HV GPS CELL SURFACE EXPRESSION

B.4 shows the additional findings on GP localization features at the cell surface in CHO cells compared to the results shown in Figure 4.1. This highlights the variations in cell surface HV GP localization observed in CHO cells.

B.5 and B.6 shows the cell surface IF results in A549 cells. Ogino et al. [102] proposed that cell surface localization of HV GPs can be influenced by the cell model used. This crucial experiment was completed to verify this hypothesis.

B.7 shows the localization of fluorescent ANDV GPs upon singular expression. The findings were similar to results reported by Deyde et al. [95] with non fluorescent ANDV GPs in Vero E6

cells.

Finally B.8 and B.9 are results pertaining to the GPMV experiments. B.8 further shows that fluorescently labelled ANDV Gn did not localize in the GPMVs. B.9 shows the PML values obtained for different HV GP construct combinations in Vero E6 and A549 cell models (details on PML, see chapter 2, PML results in CHO cells see chapter 4)

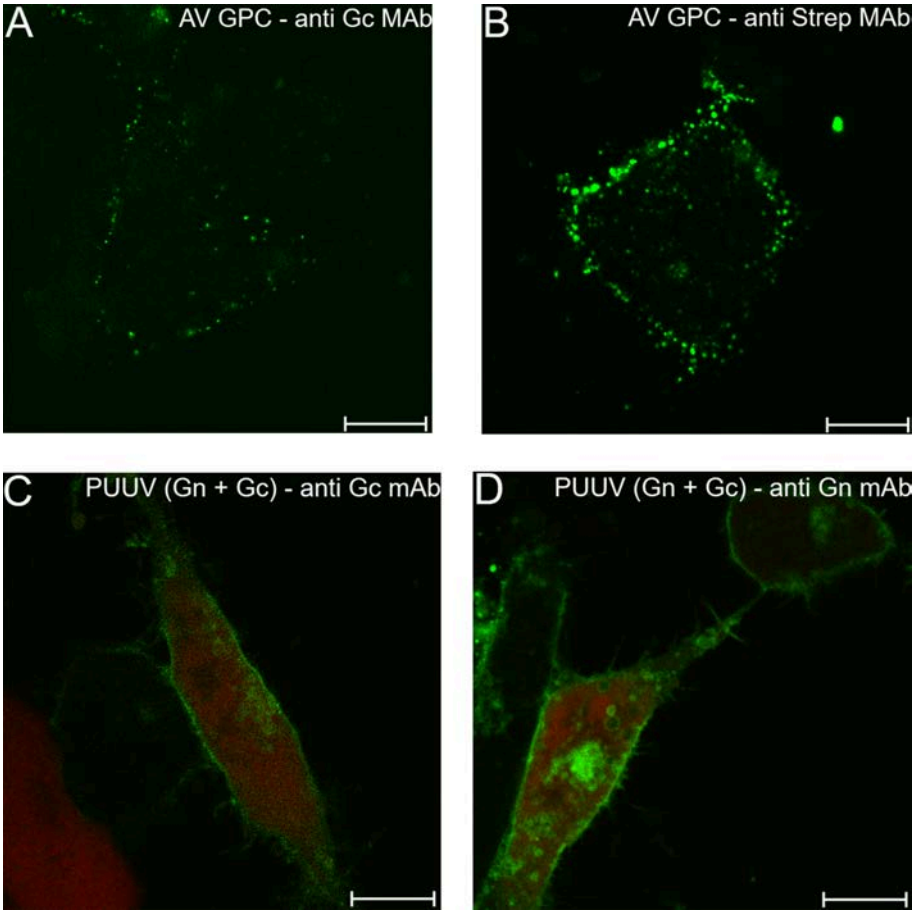

Figure B.4: **Further representative images of cell surface immunofluorescence of ANDV and PUUV GPs in CHO cells:** Representative images of the cell surface localization of [A] ANDV Gc and [B] ANDV Gn respectively after expressing ANDV Strep-II GPC. [C] Representative image of cell surface localization of PUUV Gc respectively after co-expressing PUUV Gc and PUUV Gn BD mCh2 [D] Representative image of the cell surface localization of PUUV Gn respectively after co-expressing PUUV Gn and PUUV Gc BD mCh2 in CHO cells and observed after 24 hpt. Scale bars are 10 µm

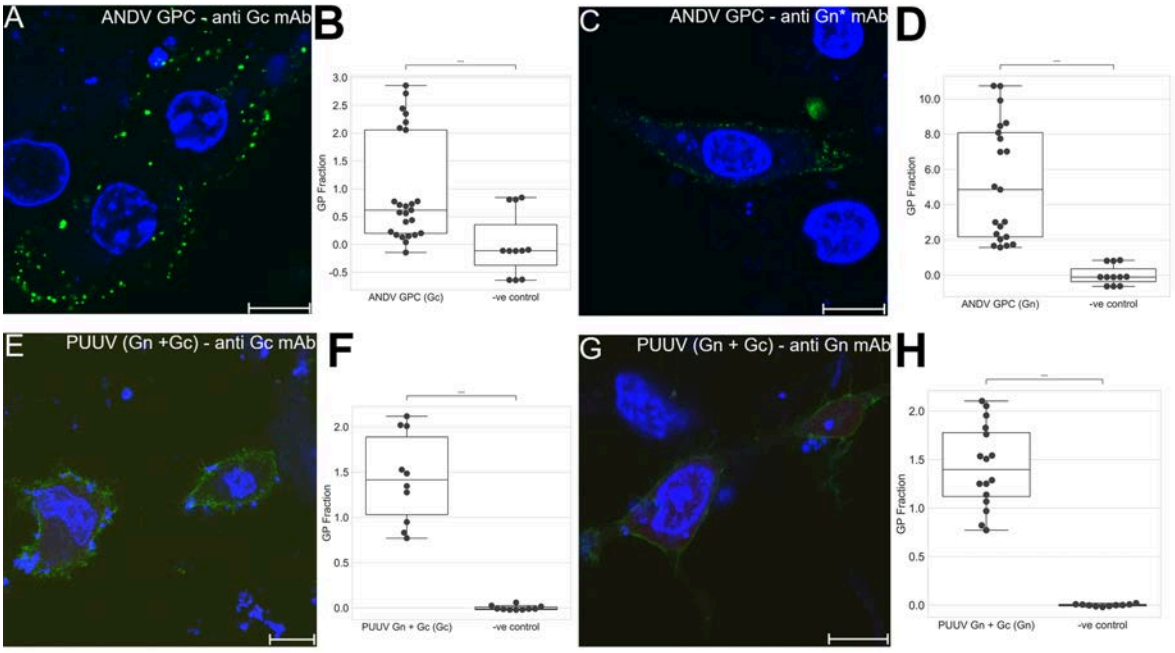

Figure B.5: **Cell surface immunofluorescence of ANDV and PUUV GPs in CHO cells in A549 cells:** ANDV and PUUV Gn & Gc localization at the PM upon co-expression of GPs in A549 cells was evaluated 24 hpt using cell surface IF staining. The nucleus was visualized using Hoechst staining (purple). Red channel in [E] and [G] denotes the mCh2 BD construct. ANDV GP localization was assessed by expressing ANDV Strep-II GPC. Representative image of the cell surface localization of [A] ANDV Gc and [B] ANDV Gn. [E] Representative image of the cell surface localization of PUUV Gc upon co-expressing PUUV Gc and PUUV Gn BD mCh2 [G] Representative image of the cell surface localization of PUUV Gn respectively after co-expressing PUUV Gn and PUUV Gc BD mCh2. PM localization of [B] ANDV Gc [D] ANDV Gn [F] PUUV Gc and [H] PUUV Gn was compared against their respective negative control using GP fraction parameter and presented as box plots. Each point in the scatter plot represents one cell. At least 8 to 10 cells were considered for each boxplot. Scale bars are 10 µm. Significance was determined by t-test, P**** ≤ 0.001.

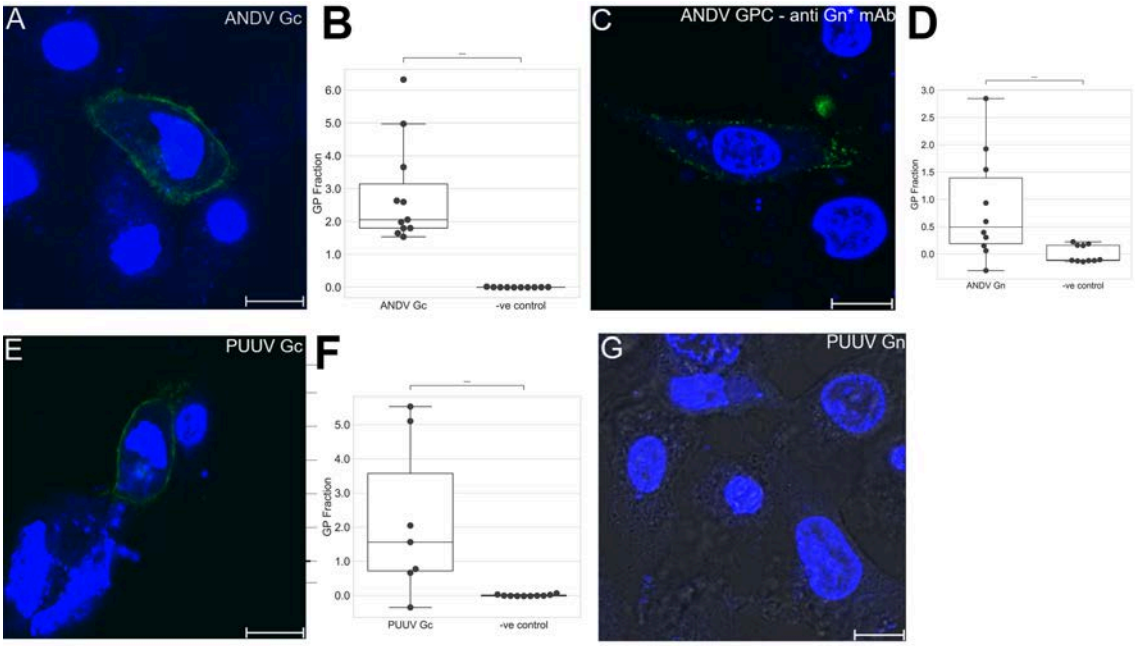

Figure B.6: **Cell surface localization of untagged ANDV and PUUV GPs upon individual expression in A549 cells**: ANDV and PUUV Gn & Gc localization at the PM upon individual expression of GPs in A549 cells was evaluated 24 hpt using cell surface IF staining. The nucleus was visualized using Hoechst staining (purple). Representative image of the cell surface localization of [A] ANDV Gc, [B] ANDV Gn, [E] PUUV Gc and [G] PUUV Gn. PM localization of [B] ANDV Gc [D] ANDV Gn [F] PUUV Gc and [H] PUUV Gn was compared against their respective negative control using using GP fraction parameter and presented as box plots. Scale bars are 10 µm. Each point in the scatter plot represents one cell. At least 8 to 10 cells were considered for each boxplot. Significance was determined by t test, P**** ≤ 0.001

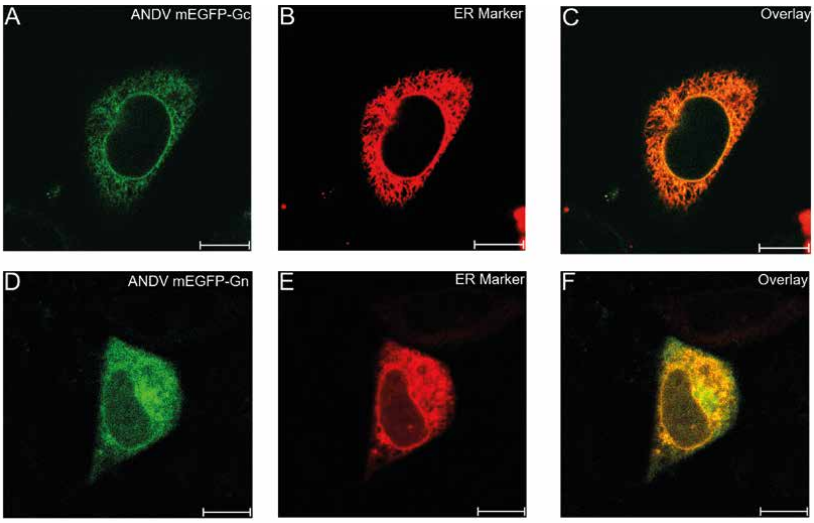

Figure B.7: **Fluorescently labelled ANDV Gn and Gc localizes partially within the endoplasmic reticulum (ER) when expressed singularly in cells:** CHO cell co-expressing [A] ANDV mEGFP-Gc and [B] ER mCherry2 , an ER marker observed 24 hpt. Cell localization of [A] ANDV mEGFP-Gc and [B] ER mCherry2 marker co-expressed in the same CHO cell is represented here. [C] Overlay image of ANDV mEGFP-Gc and ER marker. CHO cell co-expressing [D] ANDV mEGFP-Gn and [E] ER ER mCherry2 marker and observed 24 hpt. [F] Overlay image of ANDV mEGFP-Gn and ER marker. Scale bars are adjusted to 10 µm

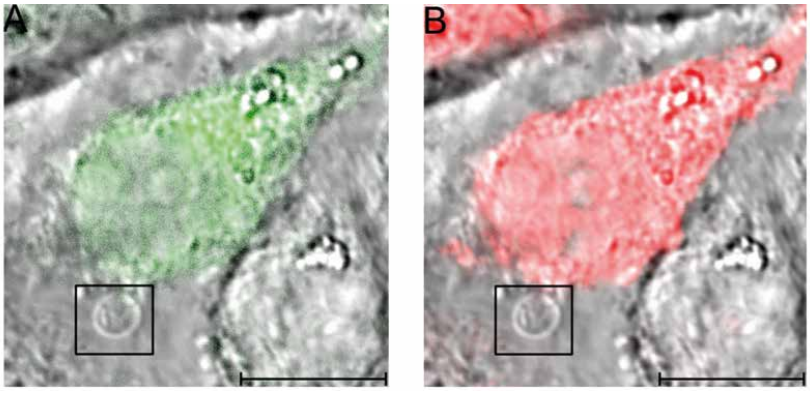

Figure B.8: **Fluorescently labelled ANDV Gn does not localize in the GPMV:** CHO Cell co-expressing ANDV mEGFP-Gn and ER-mCh2 after GPMV formation. [A] ANDV mEGFP-Gn and [B] ER-mCh2. Similar observations were seen with the mEGFP-Gn for all the HV strains and the cell lines tested. Scale bars are 10 µm.

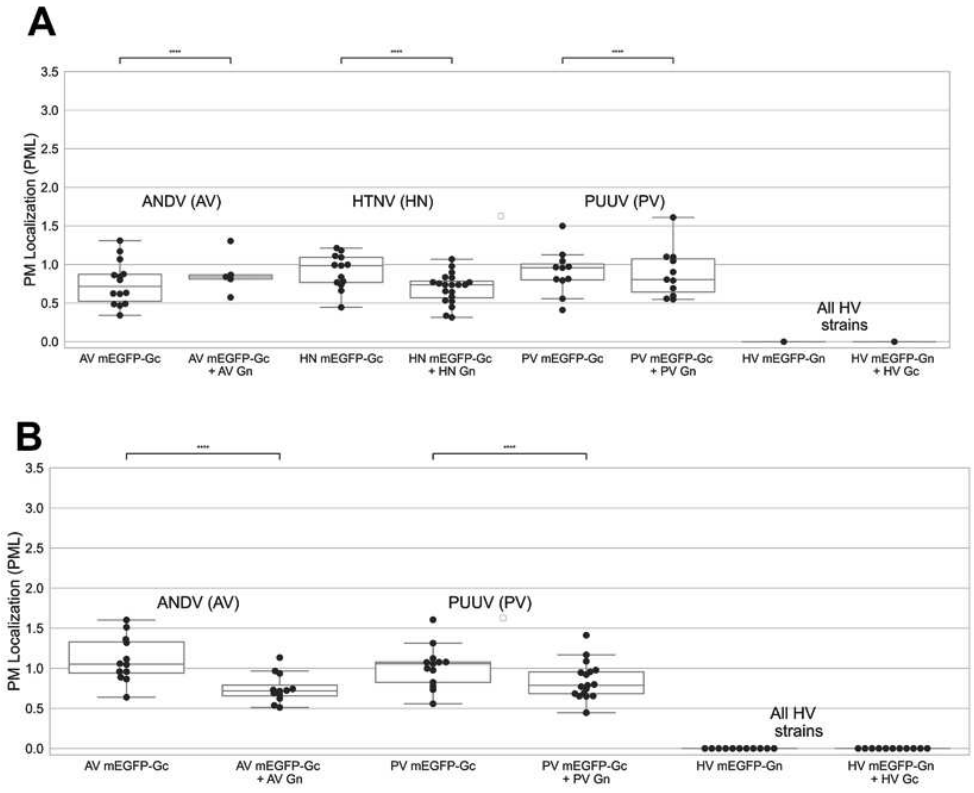

Figure B.9: **HV Gc partitions weakly into GPMVs after expression in Vero E6 and A549 cells:** PML analysis based on fluorescence intensity performed on [A] Vero E6 and [B] A549 expressing different HV constructs 24 hpt. The box plots indicate the PML values (details see chapter 2) measured in single cells expressing different construct combinations. The untagged HV construct is the BD plasmid.

C

Quantitative Sub-Cellular Interactions between Puumala HV Nucleocapsid Protein and Glycoproteins

The results in this section primarily involves fluorescently labelled PUUV GPs and NP. Any other non-fluorescent construct or HV strain will be appropriately mentioned.

C.1. Influence of Fluorescence Tagging on PUUV NP

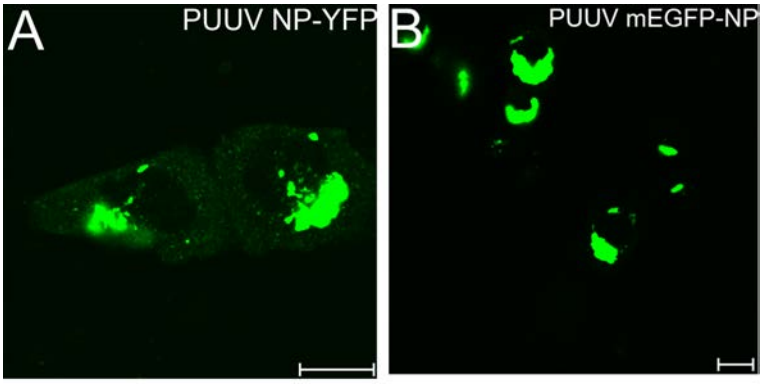

Figure C.1: **Improper fluorescent labelling of PUUV NP generates artifact blob-like structures:** Representative images of CHO cells expressing [A] NP-YFP and [B] mEGFP-NP observed 24 hpt. Scale bars are 10 µm.

The influence of fluorescence tagging on PUUV NP was initially evaluated. Davies et al.

[136] showed in TULV infected cells that NP initially forms granular punctuate and at later time points of infection forms filaments and aggregates. It was similarly verified with fluorescently labelled NP constructs. N-terminus tagging of PUUV NP with YFP resulted in similar transitions [66]. This analysis was extended to NP-YFP (YFP tagged at the C terminus) and mEGFP-NP. Both these NP constructs transitioned from granular to artifact blob-like structures without forming filaments and aggregates as observed with YFP-NP (Figure C.2).

Results with NP-YFP indicates the C-terminus fluorescent tagging of NP might lead to aberrations in NP localization. This is relevant since both N and C terminus of NP are involved in NP multimerization [39].

C.2. PUUV NP FORMS LARGE AGGREGATES IN THE PRESENCE OF PUUV GPS

Figure C.2 compares NP multimerization upon singular expression and co-expression with Gn (or Gc) 24 hpt in CHO cells. The multimerization analysis considered cells primarily expressing NP as punctuate granular oligomers in the cytosol. The average NP multimerization appeared to be higher in the presence of either GP (Gn/Gc), in comparison to its independent expression. The rationale behind this observation cannot be deduced with this experiment.

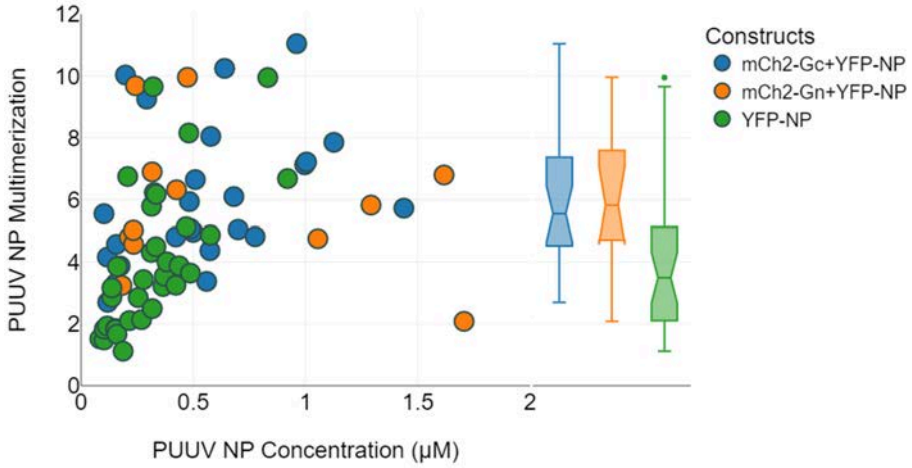

Figure C.2: **Concentration dependent N&B multimerization analysis of NP in the presence of GP (Gn/Gc):** CHO cells (i) co-expressing YFP-NP and mCh2-Gc (blue),(ii) co-expressing YFP-NP and mCh2-Gn (orange) and (iii) expressing only YFP-NP (green) observed 24 hpt. Each point in the graph represents the average multimerization in one cell. Minimum of 13 cells were considered in each construct combination. Right panel insert shows the multimerization data points grouped per category in the form of notched box plots.

C.3. PUUV NP AND PUUV GP(GN/GC) CO-EXPRESSION IN HEK AND A549 CELLS

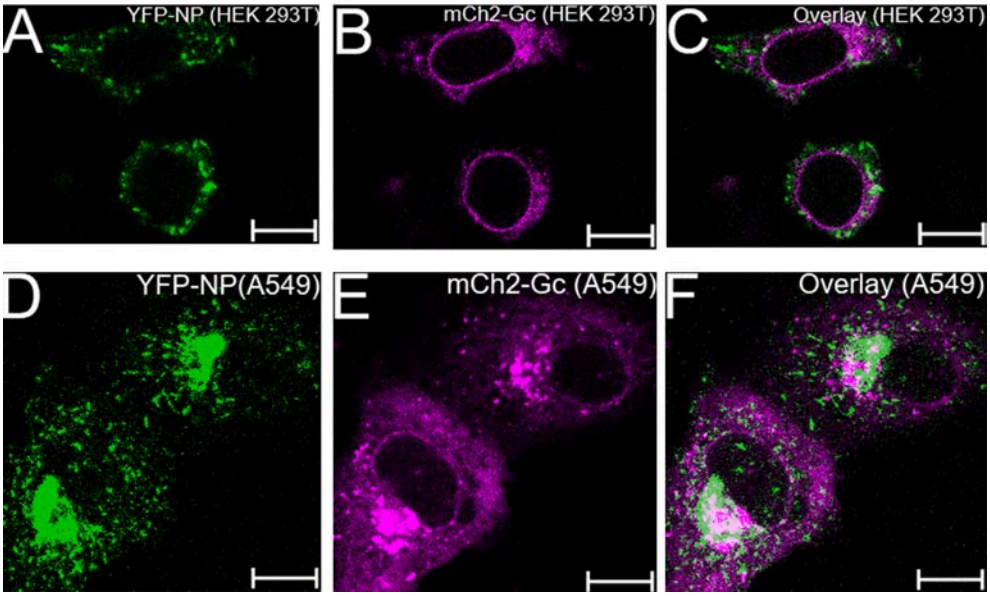

Figure C.3: **Co-expression of fluorescently labelled PUUV Gc and PUUV NP in HEK 293T and A549 cells:**[A] to [C]: Representative image of HEK 293T cells co-expressing PUUV YFP-NP and PUUV mCh2-Gc. [D] to [F] Representative image of A549 cell co-expressing PUUV YFP-NP and PUUV mCh2-Gc.

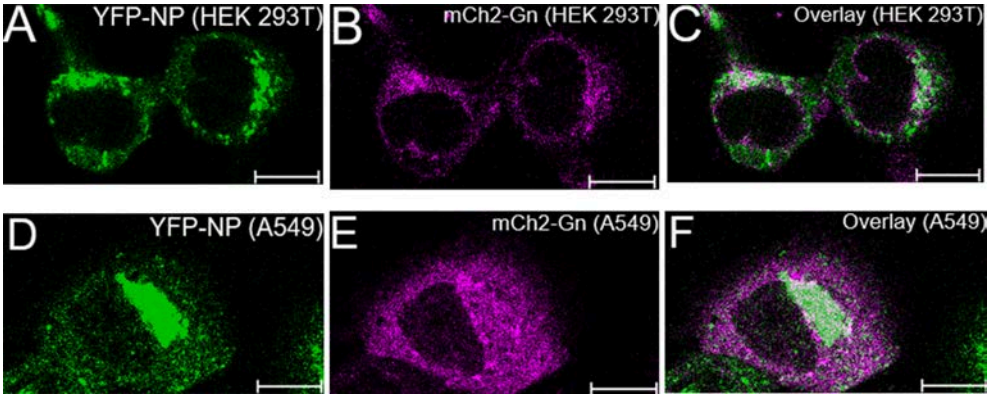

Figure C.4: **Co-expression of fluorescently labelled PUUV Gn and PUUV NP in HEK 293T and A549 cells:**[A] to [C]: Representative image of HEK 293T cells co-expressing PUUV YFP-NP and PUUV mCh2-Gn. [D] to [F] Representative image of A549 cell co-expressing PUUV YFP-NP and PUUV mCh2-Gn.

C.4. BRIGHTNESS ANALYSIS OF PUUV GP (GN/GC) UPON CO-EXPRESSION OF FLUORESCENTLY LABELLED PUUV NP, GN AND GC

Fluorescently labelled PUUV GPs co-localized with fluorescently labelled PUUV NP upon co-expression of NP, Gn and Gc from separate cDNAs [66] (see Introduction of chapter 5). The same assay was used to analyse the variations on GP multimerization (discussion of these results, see chapter 5).

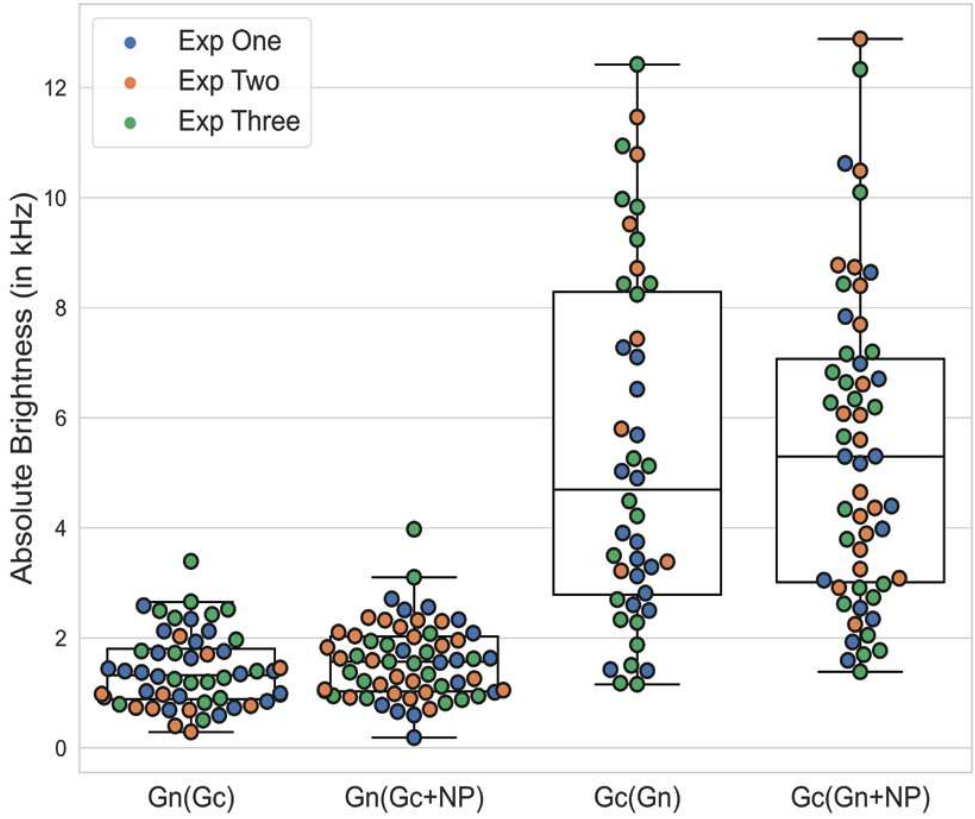

Figure C.5: **Brightness analysis of the GP on co-expression of GPs and NP:** The brightness analysis of the GP (Gn/Gc) upon co-expression of (i) YFP-Gn & mCh2-Gc and (ii) mTurq-NP, SP-YFP-Gn & SP-mCh2-Gc in HEK 293T cells observed 24 hpt. Absolute brightness of Gn in the presence of Gc is denoted by Gn (Gc) and in the presence of Gc and NP is denoted by Gn (Gc+NP). Absolute brightness of Gc in the presence of Gn is denoted by Gc (Gn) and in the presence of Gn and NP is denoted by Gn (Gn+NP). Absolute brightness $\propto$ multimerization (details see Equation 2.4 chapter 2). Every point in the boxplot represents one cell. Minimum of 20 cells were examined for each construct. Blue, orange, and green spheres represent the first, second and third set of independent experiments.

C.5. PUUV GPΔCT MULTIMERIZATION IN THE PRESENCE OF PUUV NP IN CHO AND A549 CELLS

Additional results pertaining to PUUV GPΔCT multimerization in the presence of PUUV NP in CHO and A549 cells are shown here.

Figure C.6 shows the PUUV GnΔCT multimerization in the presence of PUUV NP in CHO cells. C.6 [B] clearly shows that truncating the CT domain does have an influence on the Gn multimerization since it can no longer form up to tetramers. However, truncating the CT domain did not modulate Gn multimerization in the presence of PUUV NP. The rationale behind this observation cannot be concluded from this experiment.

Figure C.7 shows the PUUV GPΔCT multimerization in the presence of PUUV NP in A549 cells and the results are complimentary to Figure 5.4 (for PUUV GcΔCT) and Figure C.6 (for PUUV GnΔCT).

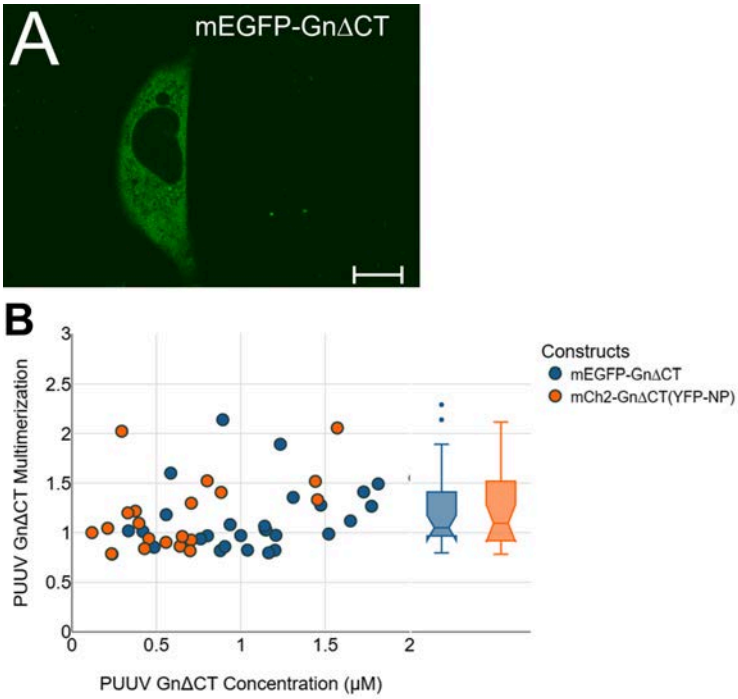

Figure C.6: **Multimerization of GnΔCT is not influenced by the presence of NP:** mEGFP-GnΔCT was expressed in the presence and absence of YFP-NP in CHO cells 24 hpt. [A] Representative images of CHO cells expressing PUUV mEGFP- GnΔCT. [B] Concentration dependent N&B multimerization analysis of GnΔCT in the absence (blue) and presence (orange) of NP. Each point in the graph represents the average multimerization in one cell. Minimum of 15 cells were examined in each case. The right panel insert shows the multimerization data points grouped per category in the form of notched box plots.Scale bars are 10 μm.

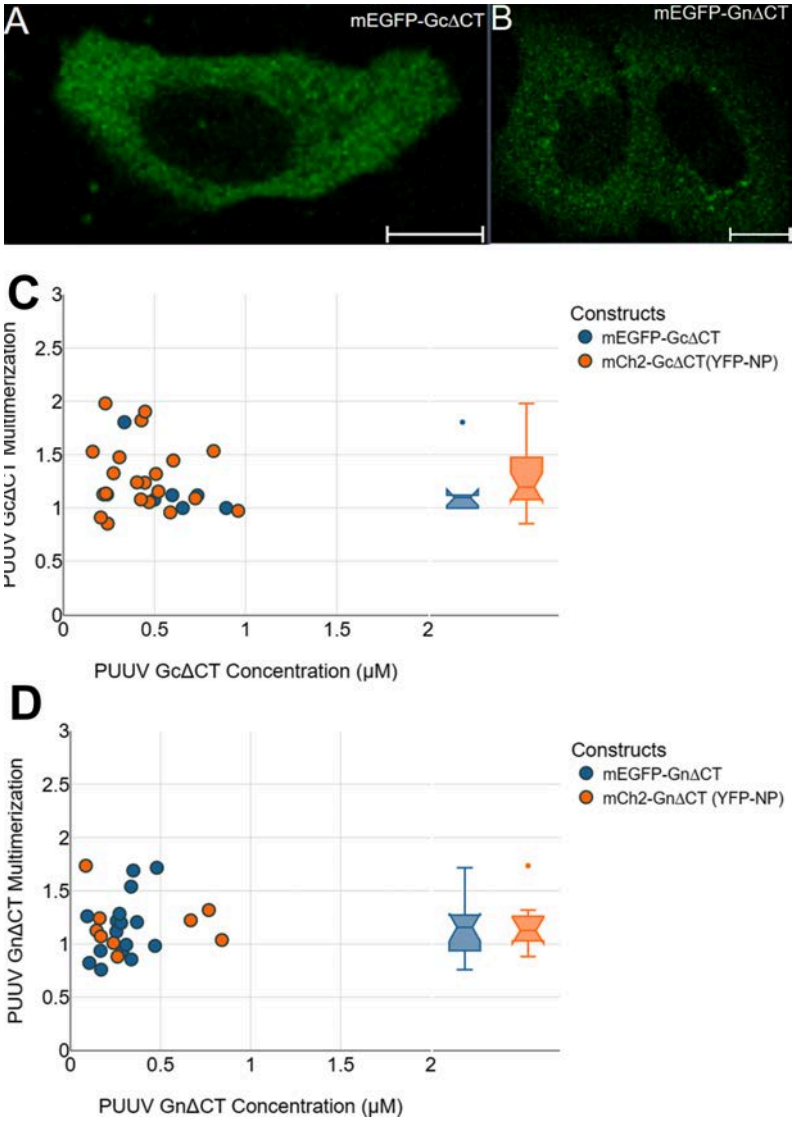

Figure C.7: **Multimerization of GPΔCT in the presence and absence of NP in living A549 cells:** Multimerization of GPΔCT in the presence and absence of NP in living A549 cells: mEGFP-GPΔCT (GP=Gn/Gc) was expressed in the presence and absence of YFP-NP in CHO cells 24 hpt. Representative images of A549 cells expressing [A] mEGFP-GcΔCT and [B] mEGFP-GnΔCT observed 24 hpt. [B] Concentration dependent multimerization analysis using N&B of [C] GcΔCT and [D] GnΔCT in the absence (blue) and presence (orange) of NP. Each point in the graph represents the average multimerization in one cell. The right panel insert shows the multimerization data points grouped per category in the form of notched box plots. Scale bars are 10 μm.

C.6. Additional results of Relative CC analysis

Figure C.8 shows the Relative CC values in HEK and A549 cells expressing the respective controls and NP-GP co-expression outlined in Figure 5.5 in CHO cells.

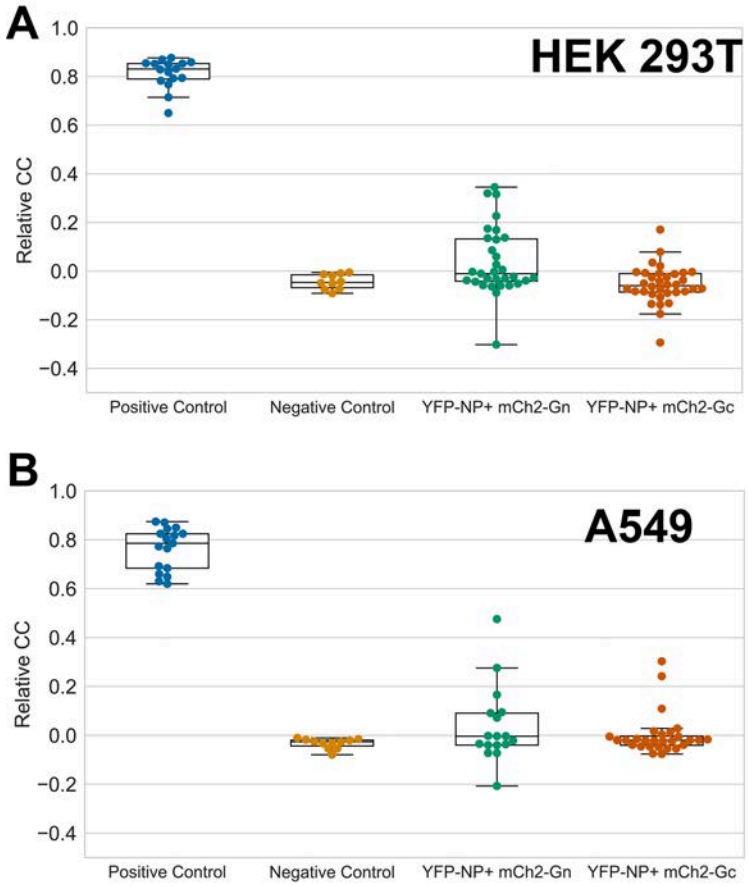

Figure C.8: **The average strength of interactions between NP and GPs co-expressed in HEK and A549 cells are weak**: Relative CC values obtained from [A] HEK cells and [B] A549 cells co-expressing NP and GP(Gn/Gc) using ccN&B. Positive control is the tandem cytosolic construct (YFP-mCh2) and the negative control, is the co-expression of YFP-NP and cytosolic mCherry2. Each point on the graph represents a single cell. The Relative CC values calculated here is the pixel average of the ROI selected in each cell (details of ROI selection, see Petrich et al.[59])

Figure C.9 shows the intensity and Relative CC maps of the controls used for the Relative CC analysis. Figure C.9 [B] and [D] particularly highlights the distribution of Relative CC upon expressing the positive and negative controls respectively.

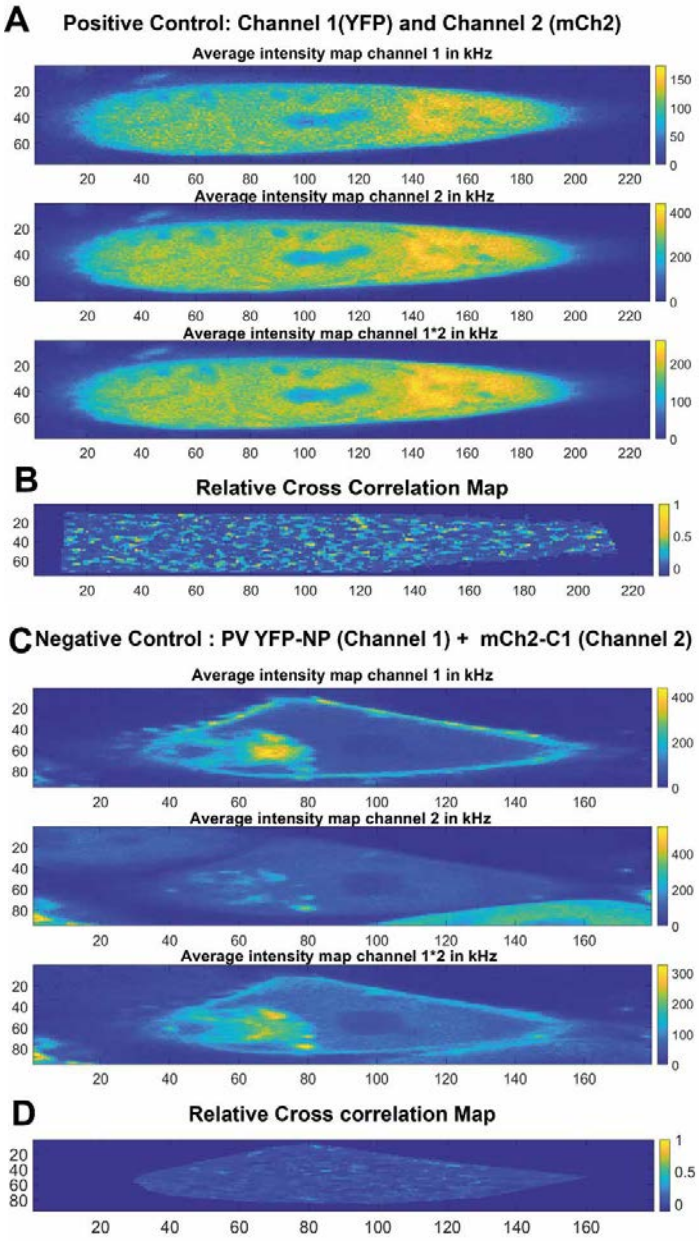

Figure C.9: **Intracellular intensity and relative cross correlation maps for controls expressed in CHO cells** [A] and [B] Tandem mEYFP-mCh2 construct (Positive Control) expressed in CHO cell 24 hpt. [A] Intensity maps for the Channel 1 (mEYFP) Channel 2 (mCh2) and Channel 1*2 (Covariance of Intensities between Channel 1 and Channel 2) are generated for the CHO cell expressing the positive control. [B] Relative Cross Correlation (details see Materials and Methods) map for the CHO cell expressing the positive control. [C] and [D] PUUV YFP-NP and mCh2-C1 (Negative Control) co-expressed in CHO cell and observed 24 hpt. [C] Intensity maps for the Channel 1 (PUUV YFP-NP) Channel 2 (mCh2-C1) and Channel 1*2 (Covariance of Intensities between Channel 1 and Channel 2) are generated for the CHO cell expressing the negative control. [D] Relative Cross Correlation map for the CHO cell expressing the negative control (details on the relevance of these maps, see Petrich et al.[59]).

BIBLIOGRAPHY

BIBLIOGRAPHY

[1] Johnson, K.M., 2001. Hantaviruses: history and overview. Hantaviruses, pp.1-14.

[2] Heyman, P., Simons, L. and Cochez, C., 2014. Were the English sweating sickness and the Picardy sweat caused by hantaviruses?. Viruses, 6(1), pp.151-171.

[3] Avšič-Županc, T., Saksida, A. and Korva, M., 2019. Hantavirus infections. Clinical Microbiology and Infection, 21, pp.e6-e16.

[4] Van Hook, C.J., 2018. Hantavirus pulmonary syndrome—the 25th anniversary of the Four Corners outbreak. Emerging Infectious Diseases, 24(11), p.2056.

[5] American Association for the Advancement of Science. 2022. The virus that rocked the Four Corners reemerges.

[6] Wells, R.M., Estani, S.S., Yadon, Z.E., Enria, D., Padula, P., Pini, N., Mills, J.N., Peters, C.J. and Segura, E.L., 1997. An unusual hantavirus outbreak in southern Argentina: person-to-person transmission? Hantavirus Pulmonary Syndrome Study Group for Patagonia. Emerging infectious diseases, 3(2), p.171.

[7] Martínez, V.P., Di Paola, N., Alonso, D.O., Pérez-Sautu, U., Bellomo, C.M., Iglesias, A.A., Coelho, R.M., López, B., Periolo, N., Larson, P.A. and Nagle, E.R., 2020. "Superspreaders" and person-to-person transmission of Andes virus in Argentina. New England Journal of Medicine, 383(23), pp.2230-2241.

[8] D'Souza, M.H. and Patel, T.R., 2020. Biodefense Implications of New-World Hantaviruses. Frontiers in bioengineering and biotechnology, p.925.

[9] Kim, W.K., Cho, S., Lee, S.H., No, J.S., Lee, G.Y., Park, K., Lee, D., Jeong, S.T. and Song, J.W., 2021. Genomic epidemiology and active surveillance to investigate outbreaks of hantaviruses. Frontiers in Cellular and Infection Microbiology, 10, p.532388.

[10] Hantavirus Infections: Friedrich-Loeffler-Institut

[11] Rki.de. 2022. RKI - RKI-Ratgeber - Hantavirus-Erkrankung.

[12] Vaheri, A., Strandin, T., Hepojoki, J., Sironen, T., Henttonen, H., Mäkelä, S. and Mustonen, J., 2013. Uncovering the mysteries of hantavirus infections. Nature Reviews Microbiology, 11(8), pp.539-550.

[13] Meyer, B.J. and Schmaljohn, C.S., 2000. Persistent hantavirus infections: characteristics and mechanisms. Trends in microbiology, 8(2), pp.61-67.

[14] Dieterle, M.E., Solà-Riera, C., Ye, C., Goodfellow, S.M., Mittler, E., Kasikci, E., Bradfute, S.B., Klingström, J., Jangra, R.K. and Chandran, K., 2021. Genetic depletion studies inform receptor usage by virulent hantaviruses in human endothelial cells. Elife, 10, p.e69708.

[15] Bauherr, S., Larsberg, F., Petrich, A., Sperber, H.S., Klose-Grzelka, V., Luckner, M., Azab, W., Schade, M., Höfer, C.T., Lehmann, M.J. and Witkowski, P.T., 2020. Macropinocytosis and clathrin-dependent endocytosis play pivotal roles for the infectious entry of Puumala virus. Journal of virology, 94(14), pp.e00184-20.

[16] Torriani, G., Mayor, J., Zimmer, G., Kunz, S., Rothenberger, S. and Engler, O., 2019. Macropinocytosis contributes to hantavirus entry into human airway epithelial cells. Virology, 531, pp.57-68.

[17] Saavedra, F., Díaz, F.E., Retamal-Díaz, A., Covián, C., González, P.A. and Kalergis, A.M., 2021. Immune response during hantavirus diseases: implications for immunotherapies and vaccine design. Immunology, 163(3), pp.262-277.

[18] Vapalahti, O., Mustonen, J., Lundkvist, Å., Henttonen, H., Plyusnin, A. and Vaheri, A., 2003. Hantavirus infections in Europe. The Lancet infectious diseases, 3(10), pp.653-661.

[19] Bi, Z., Formenty, P.B. and Roth, C.E., 2008. Hantavirus infection: a review and global update. The Journal of Infection in Developing Countries, 2(01), pp.003-023.

[20] Krueger, D.H., Ulrich, R. and Lundkvist, Å., 2001. Hantavirus infections and their prevention. Microbes and infection, 3(13), pp.1129-1144.

[21] Muranyi, W., Bahr, U., Zeier, M. and van der Woude, F.J., 2005. Hantavirus infection. Journal of the American Society of Nephrology, 16(12), pp.3669-3679.

[22] Laenen, L., Vergote, V., Calisher, C.H., Klempa, B., Klingström, J., Kuhn, J.H. and Maes, P., 2019. Hantaviridae: Current classification and future perspectives. Viruses, 11(9), p.788.

[23] Hepojoki, J., Strandin, T., Lankinen, H. and Vaheri, A., 2012. Hantavirus structure–molecular interactions behind the scene. Journal of General Virology, 93(8), pp.1631-1644.

[24] Serris, A., Stass, R., Bignon, E.A., Muena, N.A., Manuguerra, J.C., Jangra, R.K., Li, S., Chandran, K., Tischler, N.D., Huiskonen, J.T. and Rey, F.A., 2020. The hantavirus surface glycoprotein lattice and its fusion control mechanism. Cell, 183(2), pp.442-456.

[25] Guardado-Calvo, P. and Rey, F.A., 2021. The surface glycoproteins of hantaviruses. Current Opinion in Virology, 50, pp.87-94.

[26] Johansson, P., Olsson, M., Lindgren, L., Ahlm, C., Elgh, F., Holmström, A. and Bucht, G., 2004. Complete gene sequence of a human Puumala hantavirus isolate, Puumala Umeå/hu: sequence comparison and characterisation of encoded gene products. Virus research, 105(2), pp.147-155.

[27] Shi, X. and Elliott, R.M., 2004. Analysis of N-linked glycosylation of hantaan virus glycoproteins and the role of oligosaccharide side chains in protein folding and intracellular trafficking. Journal of virology, 78(10), pp.5414-5422.

[28] Zheng, F., Ma, L., Shao, L., Wang, G., Chen, F., Zhang, Y. and Yang, S., 2007. Defining the N-linked glycosylation site of Hantaan virus envelope glycoproteins essential for cell fusion. Journal of microbiology, 45(1), pp.41-47.

[29] Mittler, E., Dieterle, M.E., Kleinfelter, L.M., Slough, M.M., Chandran, K. and Jangra, R.K., 2019. Hantavirus entry: Perspectives and recent advances. Advances in virus research, 104, pp.185-224.

[30] Cifuentes-Muñoz, N., Salazar-Quiroz, N. and Tischler, N.D., 2014. Hantavirus Gn and Gc envelope glycoproteins: key structural units for virus cell entry and virus assembly. Viruses, 6(4), pp.1801-1822.

[31] Li, S., Rissanen, I., Zeltina, A., Hepojoki, J., Raghwani, J., Harlos, K., Pybus, O.G., Huiskonen, J.T. and Bowden, T.A., 2016. A molecular-level account of the antigenic hantaviral surface. Cell reports, 15(5), pp.959-967.

[32] Guardado-Calvo, P., Bignon, E.A., Stettner, E., Jeffers, S.A., Pérez-Vargas, J., Pehau-Arnaudet, G., Tortorici, M.A., Jestin, J.L., England, P., Tischler, N.D. and Rey, F.A., 2016. Mechanistic insight into bunyavirus-induced membrane fusion from structure-function analyses of the hantavirus envelope glycoprotein Gc. PLoS pathogens, 12(10), p.e1005813.

[33] Rissanen, I., Stass, R., Zeltina, A., Li, S., Hepojoki, J., Harlos, K., Gilbert, R.J., Huiskonen, J.T. and Bowden, T.A., 2017. Structural transitions of the conserved and metastable hantaviral glycoprotein envelope. Journal of virology, 91(21), pp.e00378-17.

[34] Tischler, N.D., Gonzalez, A., Perez-Acle, T., Rosemblatt, M. and Valenzuela, P.D., 2005. Hantavirus Gc glycoprotein: evidence for a class II fusion protein. Journal of General Virology, 86(11), pp.2937-2947.

[35] Willensky, S., Bar-Rogovsky, H., Bignon, E.A., Tischler, N.D., Modis, Y. and Dessau, M., 2016. Crystal structure of glycoprotein C from a hantavirus in the post-fusion conformation. PLoS Pathogens, 12(10), p.e1005948.

[36] Barriga, G.P., Villalón-Letelier, F., Márquez, C.L., Bignon, E.A., Acuña, R., Ross, B.H., Monasterio, O., Mardones, G.A., Vidal, S.E. and Tischler, N.D., 2016. Inhibition of the hantavirus fusion process by predicted domain III and stem peptides from glycoprotein Gc. PLoS neglected tropical diseases, 10(7), p.e0004799.

[37] Bignon, E.A., Albornoz, A., Guardado-Calvo, P., Rey, F.A. and Tischler, N.D., 2019. Molecular organization and dynamics of the fusion protein Gc at the hantavirus surface. Elife, 8, p.e46028.

[38] Kaukinen, P., Vaheri, A. and Plyusnin, A., 2005. Hantavirus nucleocapsid protein: a multifunctional molecule with both housekeeping and ambassadorial duties. Archives of virology, 150(9), pp.1693-1713.

[39] Reuter, M. and Krüger, D.H., 2018. The nucleocapsid protein of hantaviruses: much more than a genome-wrapping protein. Virus Genes, 54(1), pp.5-16.

[40] Mir, M.A. and Panganiban, A.T., 2004. Trimeric hantavirus nucleocapsid protein binds specifically to the viral RNA panhandle. Journal of virology, 78(15), pp.8281-8288.

[41] Arragain, B., Reguera, J., Desfosses, A., Gutsche, I., Schoehn, G. and Malet, H., 2019. High resolution cryo-EM structure of the helical RNA-bound Hantaan virus nucleocapsid reveals its assembly mechanisms. Elife, 8, p.e43075.

[42] Cheng, E., Wang, Z. and Mir, M.A., 2014. Interaction between hantavirus nucleocapsid protein (N) and RNA-dependent RNA polymerase (RdRp) mutants reveals the requirement of an N-RdRp interaction for viral RNA synthesis. Journal of virology, 88(15), pp.8706-8712.

[43] Hepojoki, J., Strandin, T., Wang, H., Vapalahti, O., Vaheri, A. and Lankinen, H., 2010. Cytoplasmic tails of hantavirus glycoproteins interact with the nucleocapsid protein. Journal of General Virology, 91(9), pp.2341-2350.

[44] Krichevsky, O. and Bonnet, G., 2002. Fluorescence correlation spectroscopy: the technique and its applications. Reports on Progress in Physics, 65(2), p.251.

[45] Klingler, J. and Friedrich, T., 1997. Site-specific interaction of thrombin and inhibitors observed by fluorescence correlation spectroscopy. Biophysical journal, 73(4), pp.2195-2200.

[46] Hess, S.T., Huang, S., Heikal, A.A. and Webb, W.W., 2002. Biological and chemical applications of fluorescence correlation spectroscopy: a review. Biochemistry, 41(3), pp.697-705.

[47] Medina, M.A. and Schwille, P., 2002. Fluorescence correlation spectroscopy for the detection and study of single molecules in biology. Bioessays, 24(8), pp.758-764.

[48] Yu, L., Lei, Y., Ma, Y., Liu, M., Zheng, J., Dan, D. and Gao, P., 2021. A comprehensive review of fluorescence correlation spectroscopy. Frontiers in physics, 9, p.644450.

[49] Bacia, K., Kim, S.A. and Schwille, P., 2006. Fluorescence cross-correlation spectroscopy in living cells. Nature methods, 3(2), pp.83-89.

[50] Macháň, R. and Wohland, T., 2014. Recent applications of fluorescence correlation spectroscopy in live systems. FEBS letters, 588(19), pp.3571-3584.

[51] Muetze, J., Ohrt, T. and Schwille, P., 2011. Fluorescence correlation spectroscopy in vivo. Laser & photonics reviews, 5(1), pp.52-67.

[52] Ries, J. and Schwille, P., 2012. Fluorescence correlation spectroscopy. BioEssays, 34(5), pp.361-368.

[53] Elson, E.L., 2011. Fluorescence correlation spectroscopy: past, present, future. Biophysical journal, 101(12), pp.2855-2870.

[54] Wohland, T., Maiti, S. and Macháň, R., 2020. An introduction to fluorescence correlation spectroscopy. IOP Publishing.

[55] Digman, M.A., Dalal, R., Horwitz, A.F. and Gratton, E., 2008. Mapping the number of molecules and brightness in the laser scanning microscope. Biophysical journal, 94(6), pp.2320-2332.

[56] Qian, H. and Elson, E.L., 1990. Distribution of molecular aggregation by analysis of fluctuation moments. Proceedings of the National Academy of Sciences, 87(14), pp.5479-5483.

[57] Dunsing, V., 2020. Fluorescence fluctuation spectroscopy techniques to quantify molecular interactions and dynamics in complex biological systems (Doctoral dissertation, Universität Potsdam).

[58] Digman, M.A., Wiseman, P.W., Choi, C., Horwitz, A.R. and Gratton, E., 2009. Stoichiometry of molecular complexes at adhesions in living cells. Proceedings of the National Academy of Sciences, 106(7), pp.2170-2175.

[59] Petrich, A., Dunsing, V., Bobone, S. and Chiantia, S., 2021. Influenza A M2 recruits M1 to the plasma membrane: A fluorescence fluctuation microscopy study. Biophysical Journal, 120(24), pp.5478-5490.

[60] Ries, J. and Schwille, P., 2006. Studying slow membrane dynamics with continuous wave scanning fluorescence correlation spectroscopy. Biophysical Journal, 91(5), pp.1915-1924.

[61] Petrášek, Z. and Schwille, P., 2008. Precise measurement of diffusion coefficients using scanning fluorescence correlation spectroscopy. Biophysical journal, 94(4), pp.1437-1448.

[62] Petrášek, Z. and Schwille, P., 2008. Scanning fluorescence correlation spectroscopy. In Single molecules and nanotechnology (pp. 83-105). Springer, Berlin, Heidelberg.

[63] Hermann, E., Ries, J. and García-Sáez, A.J., 2015. Scanning fluorescence correlation spectroscopy on biomembranes. In Methods in membrane lipids (pp. 181-197). Humana Press, New York, NY.

[64] Ries, J. and Schwille, P., 2008. New concepts for fluorescence correlation spectroscopy on membranes. Physical Chemistry Chemical Physics, 10(24), pp.3487-3497.

[65] Sperber, H.S., Welke, R.W., Petazzi, R.A., Bergmann, R., Schade, M., Shai, Y., Chiantia, S., Herrmann, A. and Schwarzer, R., 2019. Self-association and subcellular localization of Puumala hantavirus envelope proteins. Scientific reports, 9(1), pp.1-15.

[66] Welke, R., Sperber, H., Bergmann, R., Koikkarah, A., Menke, L., Sieben, C., Krüger, D., Chiantia, S., Herrmann, A. and Schwarzer, R., 2022. Characterization of Hantavirus N Protein Intracellular Dynamics and Localization. Viruses, 14(3), p.457.

[67] Noack, D., Goeijenbier, M., Reusken, C.B., Koopmans, M.P. and Rockx, B.H., 2020. Orthohantavirus pathogenesis and cell tropism. Frontiers in cellular and infection microbiology, 10, p.399.

[68] Li, C., Liu, F., Liang, M., Zhang, Q., Wang, X., Wang, T., Li, J. and Li, D., 2010. Hantavirus-like particles generated in CHO cells induce specific immune responses in C57BL/6 mice. Vaccine, 28(26), pp.4294-4300

[69] Gavrilovskaya, I. N., Brown, E. J., Ginsberg, M. H., & Mackow, E. R. (1999). Cellular entry of Hantaviruses which cause hemorrhagic fever with renal syndrome is mediated by β3 integrins. Journal of Virology, 73(5), 3951–3959.

[70] Matthys, V.S., Gorbunova, E.E., Gavrilovskaya, I.N. and Mackow, E.R., 2010. Andes virus recognition of human and Syrian hamster β3 integrins is determined by an L33P substitution in the PSI domain. Journal of virology, 84(1), pp.352-360.

[71] Ravkov, E.V. and Compans, R.W., 2001. Hantavirus nucleocapsid protein is expressed as a membrane-associated protein in the perinuclear region. Journal of Virology, 75(4), pp.1808-1815.

[72] Hägele, S., 2018. Functional Consequences of Old World Hantavirus Infection in Human Renal Cells (Doctoral dissertation).

[73] Engdahl, T.B., Kuzmina, N.A., Ronk, A.J., Mire, C.E., Hyde, M.A., Kose, N., Josleyn, M.D., Sutton, R.E., Mehta, A., Wolters, R.M. and Lloyd, N.M., 2021. Broad and potently neutralizing monoclonal antibodies isolated from human survivors of New World hantavirus infection. Cell reports, 35(5), p.109086.

[74] Cheng, E., Wang, Z. and Mir, M., 2014. Interaction between Hantavirus Nucleocapsid Protein (N) and RNA-Dependent RNA Polymerase (RdRp) Mutants Reveals the Requirement of an N-RdRp Interaction for Viral RNA Synthesis. Journal of Virology, 88(15), pp.8706-8712.

[75] Simons, M., Gorbunova, E. and Mackow, E., 2019. Unique Interferon Pathway Regulation by the Andes Virus Nucleocapsid Protein Is Conferred by Phosphorylation of Serine 386. Journal of Virology, 93(10).

[76] Vera-Otarola, J., Castillo-Vargas, E., Angulo, J., Barriga, F., Batlle, E. and Lopez-Lastra, M., 2021. The viral nucleocapsid protein and the human RNA-binding protein Mex3A promote translation of the Andes orthohantavirus small mRNA. PLOS Pathogens, 17(9), p.e1009931.

[77] Wang, Z., Ren, S., Li, Q., Royster, A., lin, L., Liu, S., Ganaie, S., Qiu, J., Mir, S. and Mir, M., 2021. Hantaviruses use the endogenous host factor P58IPK to combat the PKR antiviral response. PLOS Pathogens, 17(10), p.e1010007.

[78] Cheng, E., Wang, Z. and Mir, M., 2014. Interaction between Hantavirus Nucleocapsid Protein (N) and RNA-Dependent RNA Polymerase (RdRp) Mutants Reveals the Requirement of an N-RdRp Interaction for Viral RNA Synthesis. Journal of Virology, 88(15), pp.8706-8712.

[79] Wang, K., Ma, H., Liu, H., Ye, W., Li, Z., Cheng, L., Zhang, L., Lei, Y., Shen, L. and Zhang, F., 2019. The Glycoprotein and Nucleocapsid Protein of Hantaviruses Manipulate Autophagy Flux to Restrain Host Innate Immune Responses. Cell Reports, 27(7), pp.2075-2091.e5.

[80] Gallo, G., Caignard, G., Badonnel, K., Chevreux, G., Terrier, S., Szemiel, A., Roman-Sosa, G., Binder, F., Gu, Q., Da Silva Filipe, A., Ulrich, R., Kohl, A., Vitour, D., Tordo, N. and Ermonval, M., 2021. Interactions of Viral Proteins from Pathogenic and Low or Non-Pathogenic Orthohantaviruses with Human Type I Interferon Signaling. Viruses, 13(1), p.140.

[81] Li, N., Luo, F., Chen, Q., Zhu, N., Wang, H., Xie, L., Xiong, H., Yue, M., Zhang, Y., Feng, Y. and Hou, W., 2018. IFN-Γs inhibit Hantaan virus infection through the JAK-STAT pathway and expression of Mx2 protein. Genes & Immunity, 20(3), pp.234-244.

[82] Solà-Riera, C., García, M., Ljunggren, H. and Klingström, J., 2020. Hantavirus inhibits apoptosis by preventing mitochondrial membrane potential loss through up-regulation of the pro-survival factor BCL-2. PLOS Pathogens, 16(2), p.e1008297.

[83] Muyangwa, M., Garanina, E., Martynova, E. and Rizvanov, A., 2016. Lentivirus Expression of Hantavirus Nucleocapsid Proteins. BioNanoScience, 6(4), pp.403-406.

[84] Shin, O., Kumar, M., Yanagihara, R. and Song, J., 2013. Hantaviruses induce cell type- and viral species-specific host microRNA expression signatures. Virology, 446(1-2), pp.217-224.

[85] Prescott, J., Hall, P., Acuna-Retamar, M., Ye, C., Wathelet, M.G., Ebihara, H., Feldmann, H. and Hjelle, B., 2010. New World hantaviruses activate IFNλ production in type I IFN-deficient Vero E6 cells. PloS one, 5(6), p.e11159.

[86] Strandin, T., Hepojoki, J., Wang, H., Vaheri, A. and Lankinen, H., 2008. Hantaviruses and TNF-alpha act synergistically to induce ERK1/2 inactivation in Vero E6 cells. Virology Journal, 5(1), pp.1-9.

[87] Kang, J.I., Park, S.H., Lee, P.W. and Ahn, B.Y., 1999. Apoptosis is induced by hantaviruses in cultured cells. Virology, 264(1), pp.99-105.

[88] Li, X.D., Kukkonen, S., Vapalahti, O., Plyusnin, A., Lankinen, H. and Vaheri, A., 2004. Tula hantavirus infection of Vero E6 cells induces apoptosis involving caspase 8 activation. Journal of general virology, 85(11), pp.3261-3268.

[89] Solà-Riera, C., Gupta, S., Maleki, K.T., González-Rodriguez, P., Saidi, D., Zimmer, C.L., Vangeti, S., Rivino, L., Leo, Y.S., Lye, D.C. and MacAry, P.A., 2019. Hantavirus inhibits TRAIL-mediated killing of infected cells by downregulating death receptor 5. Cell reports, 28(8), pp.2124-2139.

[90] Petazzi, R.A., Koikkarah, A.A., Tischler, N.D. and Chiantia, S., 2021. Detection of Envelope Glycoprotein Assembly from Old World Hantaviruses in the Golgi Apparatus of Living Cells. Journal of Virology, 95(4), pp.e01238-20.

[91] Huiskonen, J.T., Hepojoki, J., Laurinmaki, P., Vaheri, A., Lankinen, H., Butcher, S.J. and Gruenewald, K., 2010. Electron cryotomography of Tula hantavirus suggests a unique assembly paradigm for enveloped viruses. Journal of virology, 84(10), pp.4889-4897.

[92] Ruusala, A., Persson, R., Schmauohn, C.S. and Pettersson, R.F., 1992. Coexpression of the membrane glycoproteins G1 and G2 of Hantaan virus is required for targeting to the Golgi complex. Virology, 186(1), pp.53-64.

[93] Shi, X. and Elliott, R.M., 2002. Golgi localization of Hantaan virus glycoproteins requires coexpression of G1 and G2. Virology, 300(1), pp.31-38.

[94] Spiropoulou, C.F., Goldsmith, C.S., Shoemaker, T.R., Peters, C.J. and Compans, R.W., 2003. Sin Nombre virus glycoprotein trafficking. Virology, 308(1), pp.48-63.

[95] Deyde, V.M., Rizvanov, A.A., Chase, J., Otteson, E.W. and Jeor, S.C.S., 2005. Interactions and trafficking of Andes and Sin Nombre Hantavirus glycoproteins G1 and G2. Virology, 331(2), pp.307-315.

[96] Hulswit, R.J., Paesen, G.C., Bowden, T.A. and Shi, X., 2021. Recent advances in bunyavirus glycoprotein research: precursor processing, receptor binding and structure. Viruses, 13(2), p.353.

[97] Goldsmith, C.S., Elliott, L.H., Peters, C.J. and Zaki, S.R., 1995. Ultrastructural characteristics of Sin Nombre virus, causative agent of hantavirus pulmonary syndrome. Archives of virology, 140(12), pp.2107-2122.

[98] Ravkov, E.V., Nichol, S.T. and Compans, R.W., 1997. Polarized entry and release in epithelial cells of Black Creek Canal virus, a New World hantavirus. Journal of virology, 71(2), pp.1147-1154.

[99] Cifuentes-Muñoz, N., Darlix, J.L. and Tischler, N.D., 2010. Development of a lentiviral vector system to study the role of the Andes virus glycoproteins. Virus research, 153(1), pp.29-35.

[100] Cifuentes-Munoz, N., Barriga, G.P., Valenzuela, P.D. and Tischler, N.D., 2011. Aromatic and polar residues spanning the candidate fusion peptide of the Andes virus Gc protein are essential for membrane fusion and infection. Journal of general virology, 92(3), pp.552-563.

[101] Acuña, R., Bignon, E.A., Mancini, R., Lozach, P.Y. and Tischler, N.D., 2015. Acidification triggers Andes hantavirus membrane fusion and rearrangement of Gc into a stable postfusion homotrimer. Journal of General Virology, 96(11), pp.3192-3197.

[102] Ogino, M., Yoshimatsu, K., Ebihara, H., Araki, K., Lee, B.H., Okumura, M. and Arikawa, J., 2004. Cell fusion activities of Hantaan virus envelope glycoproteins. Journal of virology, 78(19), pp.10776-10782.

[103] Zheng, F., Ma, L., Shao, L., Wang, G., Chen, F., Zhang, Y. and Yang, S., 2007. Defining the N-linked glycosylation site of Hantaan virus envelope glycoproteins essential for cell fusion. Journal of microbiology, 45(1), pp.41-47.

[104] Slough, M.M., Chandran, K. and Jangra, R.K., 2019. Two point mutations in old world hantavirus glycoproteins afford the generation of highly infectious recombinant vesicular stomatitis virus vectors. MBio, 10(1), pp.e02372-18.

[105] Parvate, A., Sengupta, R., Williams, E.P., Xue, Y., Chu, Y.K., Stahelin, R.V. and Jonsson, C.B., 2020. Cryofixation of Inactivated Hantavirus-Infected Cells as a Method for Obtaining High-Quality Ultrastructural Preservation for Electron Microscopic Studies. Frontiers in cellular and infection microbiology, 10, p.580339.

[106] Gallo, G., Kotlik, P., Roingeard, P., Monot, M., Chevreux, G., Ulrich, R.G., Tordo, N. and Ermonval, M., 2022. Diverse susceptibilities and responses of human and rodent cells to orthohantavirus infection reveal different levels of cellular restriction. PLOS Neglected Tropical Diseases, 16(10), p.e0010844.

[107] Hussein, I., Cheng, E., Ganaie, S., Werle, M., Sheema, S., Haque, A. and Mir, M., 2012. Autophagic Clearance of Sin Nombre Hantavirus Glycoprotein Gn Promotes Virus Replication in Cells. Journal of Virology, 86(14), pp.7520-7529

[108] Steinkühler, J., Sezgin, E., Urbančič, I., Eggeling, C. and Dimova, R., 2019. Mechanical properties of plasma membrane vesicles correlate with lipid order, viscosity and cell density. Communications Biology, 2(1).

[109] CHARRAS, G., 2008. A short history of blebbing. Journal of Microscopy, 231(3), pp.466-478.

[110] Charras, G., Coughlin, M., Mitchison, T. and Mahadevan, L., 2008. Life and Times of a Cellular Bleb. Biophysical Journal, 94(5), pp.1836-1853.

[111] Charras, G., Hu, C., Coughlin, M. and Mitchison, T., 2006. Reassembly of contractile actin cortex in cell blebs. Journal of Cell Biology, 175(3), pp.477-490.

[112] Bauer, B., Davidson, M. and Orwar, O., 2009. Proteomic analysis of plasma membrane vesicles. Angewandte Chemie International Edition, 48(9), pp.1656-1659.

[113] Sedgwick, A., Olivia Balmert, M. and D'Souza-Schorey, C., 2018. The formation of giant plasma membrane vesicles enable new insights into the regulation of cholesterol efflux. Experimental Cell Research, 365(2), pp.194-207.

[114] Kwon, H., Lee, J., Jeong, K., Jang, D. and Pak, Y., 2013. A novel actin cytoskeleton-dependent noncaveolar microdomain composed of homo-oligomeric caveolin-2 for activation of insulin signaling. Biochimica et Biophysica Acta (BBA) - Molecular Cell Research, 1833(10), pp.2176-2189.

[115] Steinkühler, J., Różycki, B., Alvey, C., Lipowsky, R., Weikl, T., Dimova, R. and Discher, D., 2018. Membrane fluctuations and acidosis regulate cooperative binding of "marker of self" CD47 with macrophage checkpoint receptor SIRPα. Journal of Cell Science,.

[116] Dunsing, V., Mayer, M., Liebsch, F., Multhaup, G. and Chiantia, S., 2017. Direct evidence of amyloid precursor–like protein 1 trans interactions in cell–cell adhesion platforms investigated via fluorescence fluctuation spectroscopy. Molecular Biology of the Cell, 28(25), pp.3609-3620.

[117] McCaughey, C., Shi, X., Elliott, R.M., Wyatt, D.E., O'Neill, H.J. and Coyle, P.V., 1999. Low pH-induced cytopathic effect—a survey of seven hantavirus strains. Journal of virological methods, 81(1-2), pp.193-197.

[118] Chen S.Y., Matsuoka Y., Compans R.W. Golgi complex localization of the Punta Toro virus G2 protein requires its association with the G1 protein. Virology. 1991;183:351–365. doi: 10.1016/0042-6822(91)90148-5.

[119] Gerrard, S.R. and Nichol, S.T., 2002. Characterization of the Golgi retention motif of Rift Valley fever virus GN glycoprotein. Journal of virology, 76(23), pp.12200-12210.

[120] Spiegel, M., Plegge, T. and Pöhlmann, S., 2016. The role of phlebovirus glycoproteins in viral entry, assembly and release. Viruses, 8(7), p.202.

[121] Shi, X., Kohl, A., Li, P. and Elliott, R.M., 2007. Role of the cytoplasmic tail domains of Bunyamwera orthobunyavirus glycoproteins Gn and Gc in virus assembly and morphogenesis. Journal of virology, 81(18), pp.10151-10160.

[122] Carnec, X., Ermonval, M., Kreher, F., Flamand, M. and Bouloy, M., 2014. Role of the cytosolic tails of Rift Valley fever virus envelope glycoproteins in viral morphogenesis. Virology, 448, pp.1-14.

[123] Ramanathan, H. and Jonsson, C., 2008. New and Old World hantaviruses differentially utilize host cytoskeletal components during their life cycles. Virology, 374(1), pp.138-150.

[124] Zhou, H., Sun, Y., Guo, Y. and Lou, Z., 2013. Structural perspective on the formation of ribonucleoprotein complex in negative-sense single-stranded RNA viruses. Trends in Microbiology, 21(9), pp.475-484.

[125] Liljeroos, L., 2013. Matrix proteins as centralized organizers of negative-sense RNA virions. Frontiers in Bioscience, 18(2), p.696.

[126] Wang, H., Alminaite, A., Vaheri, A. and Plyusnin, A., 2010. Interaction between hantaviral nucleocapsid protein and the cytoplasmic tail of surface glycoprotein Gn. Virus Research, 151(2), pp.205-212.

[127] Shimizu, K., Yoshimatsu, K., Koma, T., Yasuda, S. and Arikawa, J., 2013. Role of nucleocapsid protein of hantaviruses in intracellular traffic of viral glycoproteins. Virus Research, 178(2), pp.349-356.

[128] Acuña, R., Cifuentes-Muñoz, N., Márquez, C., Bulling, M., Klingström, J., Mancini, R., Lozach, P. and Tischler, N., 2014. Hantavirus Gn and Gc Glycoproteins Self-Assemble into Virus-Like Particles. Journal of Virology, 88(4), pp.2344-2348.

[129] Willensky, S., Bar-Rogovsky, H., Bignon, E.A., Tischler, N.D., Modis, Y. and Dessau, M., 2016. Crystal structure of glycoprotein C from a hantavirus in the post-fusion conformation. PLoS Pathogens, 12(10), p.e1005948.

[130] Biener, G., Stoneman, M.R. and Raicu, V., 2021. Fluorescence intensity fluctuation analysis of receptor oligomerization in membrane domains. Biophysical Journal, 120(15), pp.3028-3039.

[131] Hägele, S., Müller, A., Nusshag, C., Reiser, J., Zeier, M. and Krautkrämer, E., 2019. Virus- and cell type-specific effects in orthohantavirus infection. Virus research, 260, pp.102-113.

[132] Snippe, M., Borst, J.W., Goldbach, R. and Kormelink, R., 2007. Tomato spotted wilt virus Gc and N proteins interact in vivo. Virology, 357(2), pp.115-123.

[133] Ribeiro, D., Borst, J.W., Goldbach, R. and Kormelink, R., 2009. Tomato spotted wilt virus nucleocapsid protein interacts with both viral glycoproteins Gn and Gc in planta. Virology, 383(1), pp.121-130.

[134] Meier, K., Thorkelsson, S.R., Quemin, E.R. and Rosenthal, M., 2021. Hantavirus Replication Cycle—An Updated Structural Virology Perspective. Viruses, 13(8), p.1561.

[135] Rowe, R.K., Suszko, J.W. and Pekosz, A., 2008. Roles for the recycling endosome, Rab8, and Rab11 in hantavirus release from epithelial cells. Virology, 382(2), pp.239-249.

[136] Davies, K.A., Chadwick, B., Hewson, R., Fontana, J., Mankouri, J. and Barr, J.N., 2020. The RNA replication site of Tula orthohantavirus resides within a remodelled Golgi network. Cells, 9(7), p.1569.

[137] Sezgin, E., Kaiser, H.J., Baumgart, T., Schwille, P., Simons, K. and Levental, I., 2012. Elucidating membrane structure and protein behavior using giant plasma membrane vesicles. Nature protocols, 7(6), pp.1042-1051.

[138] Strandin, T., Hepojoki, J., Wang, H., Vaheri, A. and Lankinen, H., 2011. The cytoplasmic tail of hantavirus Gn glycoprotein interacts with RNA. Virology, 418(1), pp.12-20.

[139] Strandin, T., Hepojoki, J. and Vaheri, A., 2013. Cytoplasmic tails of bunyavirus Gn glycoproteins—Could they act as matrix protein surrogates?. Virology, 437(2), pp.73-80.

PUBLICATION LIST

The following is the list of the publications (published and in preparation) which has the results presented in this thesis:

1. Petazzi, R.A., **Koikkarah, A.A.**, Tischler, N.D. and Chiantia, S., 2021. Detection of Envelope Glycoprotein Assembly from Old World Hantaviruses in the Golgi Apparatus of Living Cells. Journal of Virology, 95(4), pp.e01238-20.

2. Welke, R., Sperber, H., Bergmann, R., **Koikkarah, A.**, Menke, L., Sieben, C., Krüger, D., Chiantia, S., Herrmann, A. and Schwarzer, R., 2022. Characterization of Hantavirus N Protein Intracellular Dynamics and Localization. Viruses, 14(3), p.457

3. **Koikkarah, A.**, Albornoz A., Castillo, N.M, Tischler N.D, Chiantia, S. *Plasma Membrane Assembly of Hantavirus Glycoproteins* (Manuscript in preparation)

4. **Koikkarah, A.**, Schwarzer, R., Sieben, C., Chiantia, S. *Quantitative sub cellular interactions between nucleocapsid protein and glycoproteins of Puumala Orthohantaviruses* (Manuscript in preparation)

Publications that have not be included in this work are:

1. Petazzi, R. A., **Aji, A. K.**, & Chiantia, S. (2020). Fluorescence microscopy methods for the study of protein oligomerization. Progress in Molecular Biology and Translational Science Oligomerization in Health and Disease: From Enzymes to G Protein-Coupled Receptors, 1-41

2. Menke, L.; Sperber H.S., **Koikkarah, A.**, Chiantia, S., Schwarzer, R., Sieben, C.; Advances in fluorescence microscopy for orthohantavirus research (Submitted to Microscopy, Oxford University Press (OUP))

List of Figures

List of Tables

ACKNOWLEDGEMENTS

"We have not wings, we cannot soar
But we have feet to scale and climb
By slow degrees, by more and more
The cloudy summits of our time."

Henry Wadsworth Longfellow

The curtains are about to fall for the time cometh to bid adieu to my PhD voyage. This journey would have remained impossible without the support, motivation and mindful advice offered by several people, attesting the philosophy purported by St.Teresa *" We can all do small things, with great love, and together we can do something wonderful".*

To Salvo, first and foremost, thank you for the opportunity to complete the PhD under your supervision. My gratitude extends for the support, advice and trust during this entire PhD period. You created a great working environment with freedom for development and the resources to explore multiple fundamental questions. Your advice on different facets of my PhD work has instilled the confidence to be an independent researcher with dexterity and finesse. *Grazie per essere un grande mentore e per avermi insegnato la ricetta per essere un ricercatore credibile.*

To Roberto, thank you for ensuring that I was well trained with dealing with my independent research questions on Hantaviruses and also equipping me with the molecular biology skills for the project. **To Valentin, the First**, my gratitude for teaching me the intricacies of fluorescence microscopy and for your critique with my work in that regard. Several outcomes in this work have stemmed out from that.

To Anne, basically the trusted buddy cop of the my PhD series. Whenever chaos commenced on the project, starting from cloning to microscopy analysis, you were there always to render help and assistance. Without it, I would have not laid adrift during the challenging phases of my PhD research. A big gratitude for everything.

To Jana and Mandy, Danke, dass Sie mein Unterstützungssystem im Labor sind. Ohne Ihre Hilfe wäre ich als Seele gestrandet. To **Sweta**, dafür, die deutsche Bürokratie vereinfachter erscheinen zu lassen als sonst. **To Amaury and Titas**, my gratitude for all your help during the latter phases of my PhD. To Martin, for your advice and critique, that has shaped this dissertation in a better manner. And to **Valentin, the Second**, for your assistance with all the documentation and scheduling with the thesis submission.

To my collaborators **Dr.Nicole Tischler, Dr.Roland Schwarzer and Dr.Christian Sieben**, thank

you for sharing your expertise in the Hantavirus biology and also ensuring that the research outcomes are of the highest quality. Particularly to Nicole, who even patiently sat with me in the wee hours at Robinson College in Cambridge to discuss the implications of my work (hopefully not earning the wrath of her daughters).

To Oren My journey into biology was made possible with the Internship at your group. You were a great mentor and friend during this phase and I want to thank you being a strong pillar of support. Also a big gratitude to the members of your lab particularly **Sana**, **Sofia** and **Kristin** for being my first teachers in experimental biology and being extremely patient with a theoretical chap fiddling with the inclination of how a pipette must be held.

Desolation would have struck the proceedings if not for the unwavering support of my friends around the world - whether it be my homies in Berlin **Dilip**, **Varki** and **Siraj**, my buddies from Netherlands especially God level **Aswin**, Anirudh, Jishnu, Nitin and others and folks from my university days back in Anna including Natty **Nathaniel**, **Thomas** whom I visited during all the major milestones of my European life and **Members of the Football Whatsapp Group**. To **Priti** Didi and *Amarens* for always lending an ear whenever I was down and making sure that I remained on track despite all the challenges I faced during this phase.

To my family, **Appa** and **Amma** this one is for you. Your unwavering pillar of support and your continued persistence of faith and trust in me has finally made this possible. And to **Roshan**, for being understanding of the rollercoaster PhD ride and dealing with my eccentricities during this period.

And finally my journey in Science would have remained a dream if not for the patience and guidance by my high school maths teacher **Gangadharan Sir**. This would not have been possible without you.

EIDESSTATTLICHE ERKLÄRUNG

und Einverständniserklärung
nach § 6 Abs. 2 Nr. 5, 6 und 7 der Promotionsordnung der
Mathematisch-Naturwissenschaftlichen
Fakultät der Universität Potsdam vom 10.07.2013

Von:

Name: Koikkarah Aji

Vorname(n): Amit

Hiermit versichere ich an Eides statt, dass

- meine hinsichtlich der früheren Teilnahme an Promotionsverfahren gemachten Angaben richtig sind;
- die eingereichte Arbeit oder wesentliche Teile derselben in keinem anderen Verfahren zur Erlangung eines akademischen Grades vorgelegt worden sind;
- bei der Anfertigung der Dissertation die Grundsätze zur Sicherung guter wissenschaftlicher Praxis der DFG eingehalten wurden, die Dissertation selbständig und ohne fremde Hilfe verfasst wurde, andere als die von mir angegebenen Quellen und Hilfsmittel nicht benutzt worden sind und die den benutzten Werken wörtlich oder sinngemäß entnommenen Stellen als solche kenntlich gemacht wurden

Einer Überprüfung der eingereichten Dissertationsschrift bzw. der an deren Stelle eingereichten Schriften mittels einer Plagiatssoftware stimme ich zu.

Ort und Datum:

Unterschrift: